Structural and Physical Characterization of Insect Flow Systems

Melissa C. Kenny

Dissertation submitted to the faculty of the
Virginia Polytechnic Institute and State University
in partial fulfillment of the requirements for the degree of

Doctor of Philosophy
in
Biomedical Engineering

John J. Socha, Chair

Mark A. Stremler

Rafael V. Davalos

Douglas G. Pfeiffer

Laura A. Miller

May 2, 2019

Blacksburg, Virginia

Keywords: Insect, Respiration, Murray's Law, Circulation, Hemolymph, Viscosity, Dorsal Vessel

Structural and Physical Characterization of Insect Flow Systems

Melissa C. Kenny

Academic Abstract:

This dissertation characterizes the geometry, kinematics, and physical properties of insect internal structures that make up the respiratory and circulatory systems. This characterization is necessary to better understand how these systems function to transport fluids at the microscale, and ultimately, how we might computationally model this flow. Chapter 2 describes the geometry of the insect tracheal system, specifically testing if Murray's law applies to this system using three-dimensional imaging of tracheal tubes. Chapter 3 begins to characterize the physical properties of insect hemolymph, specifically the viscosity and density of hemolymph, using experimental measurements. Because insects are strongly affected by environmental temperature, this chapter also explores how hemolymph viscosity may be affected by temperature. Chapter 4 builds on the results of Chapter 3, exploring the effects of developmental responses to temperature on hemolymph viscosity and properties, as well as performance of the insect using experimental measurements. Finally, Chapter 5 presents a kinematic and structural characterization of the insect heart using a variety of imaging techniques and analyses.

This work was partially supported by the National Science Foundation under grants 1558052, 0938047, 1301037, and 0966125.

Structural and Physical Characterization of Insect Flow Systems

Melissa C. Kenny

General Audience Abstract:

Insect physiology and morphology has long been studied by biologists and entomologists, with many of the basic features understood and characterized. The insect circulatory and respiratory systems differ greatly from those of many other organisms. Physically, these systems transport fluids through microscale environments which include a variety of pumps, networks, and other structures that facilitate flow. Functionally, the circulatory and respiratory systems are largely decoupled, unlike in vertebrates. The respiratory system transports air directly to deliver oxygen to tissues, whereas the circulatory system transports various nutrients and other chemicals via hemolymph. With these unique differences, investigation of these major biological transport systems in insects is essential to fully understand their structure and function. This dissertation addresses many of the basic structural and physical properties of the insect respiratory and circulatory systems that are still unknown, despite growing engineering analysis. First, I measured specific geometric features of the insect tracheal network and determined if Murray's law applies to this system. Second, I quantified the viscosity of insect hemolymph, including in response to temperature. To expand upon this relationship further, I measured hemolymph viscosity, hemolymph composition, and insect performance after temperature acclimation during development. Last, I investigated the morphology and kinematics of the insect heart, using many methods of imaging and analysis to measure structural features of the heart wall, including during function. Hemolymph properties and heart morphology provide the physical basis of flow production within the circulatory system. Understanding flow production within the circulatory system, as well as design features of the respiratory system, are crucial in the construction of mathematical models of both hemolymph and air flow within the insect.

This work was partially supported by the National Science Foundation under grants 1558052, 0938047, 1301037, and 0966125.

Dedication

For my dad, John Kenny, who instilled in me a love of all things math and science, and whose support, motivation, and inspiration are the very reason I am an engineer.

For my mom, Tammy Kenny, whose love and support has been unflagging, and who has always listened whenever I have needed her.

Acknowledgments

I would like to express my deepest gratitude to Dr. Jake Socha, my advisor, for all of his insight, encouragement, wisdom, and, most importantly, patience over the years. He has been my guidepost throughout this process, helping me navigate through the sometimes stressful, but ultimately rewarding, graduate school path. He has taught me to have a discerning eye, to avoid assumptions, and to always ask questions. In particular, he has instilled in me an appreciation for science communication and teaching. I will never forget to always tell science as a story! I also thank my committee members, Dr. Mark Stremler, Dr. Rafael Davalos, Dr. Douglas Pfeiffer, and Dr. Laura Miller for their valuable advice and encouragement.

I owe a special thanks to my lab-mates for the many discussions, assistance, and feedback they have provided. I wish to express my sincere thanks to Khaled Adjerid for helping me with numerous experiments and for always being a listening ear; Talia Weiss for her expert coding and electronics help; Dr. Matthew Giarra for his help with the hungry caterpillars and their hemolymph; Joel Garrett for help with several experiments and for always finding the humor in the moment; Christie Crandall for significant contributions to Chapter 4 with both experiments and analyses; and Dr. Sharri Zamore for always grounding me and being the best office-mate I could ask for. I would also like to acknowledge Jack Whitehead, Dr. Hodjat Pendar, Marta Drabek, Michelle Graham, Joshua Pulliam, Pat Rogers, Brittany Horton, and Katie Johnston. Also, I thank the bugs for their many sacrifices to make this dissertation possible.

Beyond the lab work, I owe my sincerest thanks to all of my family and friends who have helped me throughout this journey. I want to specifically thank Dr. Megan Cox, Sara Easterwood, Corrine Woods, Andrew Hoskins, and Alyson Dietze for their support and encouragement. I also acknowledge Dr. Ken Reid, who, in hiring me to teach freshman engineering, ignited my passion and ambition for teaching. His support, and the many opportunities he has provided, have been extremely beneficial and I am eternally grateful.

Last, and certainly not least, I must give my deepest thanks to the two beings who have helped me more than most: Brindal and Dag. To Brindal, my horse, whose love and antics have either firmly maintained or seriously detracted from my sanity. To Dag the dog, who never fails to make me feel better and who is my partner in crime.

Thank you.

Melissa C. Kenny

Blacksburg, VA

May, 2019

Contents

List of Figures

List of Tables

Chapter 1

Introduction

Insect physiology and morphology has long been studied by biologists and entomologists, with many of the basic features understood and characterized. In particular, the basic structure and function of the respiratory and circulatory systems of insects has been identified. These systems comprise complex networks that interact with fluids at the microscale. The respiratory system does not transport oxygen within the blood, which differs from vertebrates. Instead, oxygen is transported to the tissues via a system of branching tracheal tubes which terminate in valves, called "spiracles", which open to the air. These tubes function to move air via both diffusion through the network and active ventilation, which relies on tracheal collapse patterns in some species. In contrast, the insect circulatory system is open, so that all tissues are simply bathed in hemolymph. The primary pumping organ of this system, the dorsal vessel, facilitates circulation of nutrients, hormones, and waste throughout the insect coelem. In spite of growing engineering analysis of insects, there are many basic physical properties of the insect respiratory and circulatory systems that are still unknown**.** Using various experimental methods, I investigated the specific geometry of tracheal system branching, the morphology and kinematics of the dorsal vessel, and the physical properties of insect hemolymph and its response to temperature.

This dissertation provides data that characterizes the geometry, kinematics, and physical properties of insect internal structures that make up the respiratory and circulatory systems. This characterization is necessary to better understand and model these insect systems. Mathematical analysis of the geometry of the tracheal system may help us to understand methods of flow within the respiratory system and could provide inspiration for tissue engineers to better oxygenate artificial tissues and organs. Discovery of the physical properties of insect hemolymph and an in-depth study of the morphology and kinematics of the insect dorsal vessel provide further understanding of the physical basis of flow production within the insect circulatory system. Understanding flow production within the circulatory system is crucial in the construction of mathematical models of hemolymph flow within the insect. The methods used here also produce visualizations of internal insect structures, including 3D reconstructions of the tracheal network and real-time videos of dorsal vessel function. Besides providing novel data for several specific species of insect, including *Platynus decentis*, *Manduca sexta*, and *Zophobas morio*, the experimental and analysis methods of this project can be applied to many species of insects as well as other organisms.

1.1 Overview of insect physiology

The insect circulatory and respiratory systems differ greatly from those of many other organisms. Physically, these systems operate at a very small scale. These systems transport fluids through microscale environments which include a variety of pumps, networks, and other structures which facilitate flow. Functionally, the circulatory and respiratory system are largely decoupled, unlike in vertebrates. The respiratory system transports air directly to deliver oxygen to tissues, whereas the circulatory system transports various nutrients and other chemicals via hemolymph [6]. With these unique differences, investigation of these major biological transport systems in insects is essential to fully understand their structure and function. In spite of growing analysis, there are many basic structural and physical properties of the insect respiratory and circulatory systems that are still unknown.

1.1.1 Our current understanding of the insect respiratory system

The insect respiratory system functions by delivering oxygen directly to tissues within the animal through a network of internal tracheal tubes connected directly to the air. This system begins with spiracular valves along the lateral sides of the abdomen and thorax which connect to large tracheae for bulk flow and branch to small, micron-sized tracheoles as exchange sites [6]. This system was originally thought to be driven predominantly via diffusion of oxygen through the network, but insects have been found to also employ convective flows to improve transport [7]. Some active measures can also be used such as abdominal pumping and tracheal collapse which may aid in respiration via active ventilation [8, 9]. Tracheal compression within several species of insect has been viewed in real-time due to advances in x-ray imaging during breathing events [7, 9, 10].

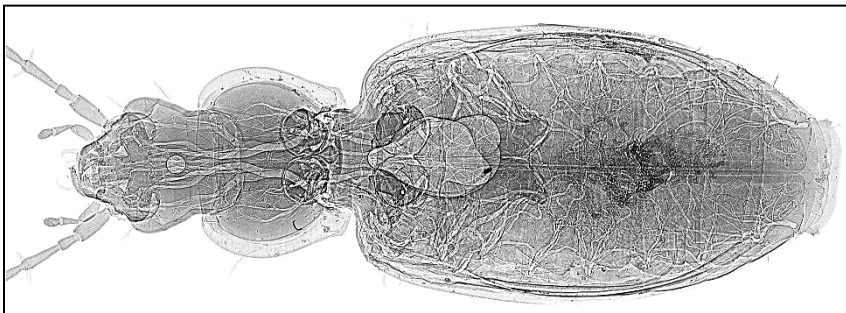

Figure 1.1: Synchrotron x-ray scan of a carabid beetle *Platynus decentis* showing the tracheal system throughout the body (adapted from [1] with permission).

In terms of the structure of the tracheal network, the larger tracheae are multicellular with sclerotized taenidia and function to transport oxygen to the single-celled tracheoles where gas exchange occurs [6]. The basic arrangement of tracheal tubes follows a similar pattern among most insects, including lateral trunks to connect the spiracles, with transverse and longitudinal trunks across the coelem (Fig. 1.1). From these main trunks, tubes branch to local tissues depending on the metabolic demands and response to areas of hypoxia [6, 11].

1.1.2 Our current understanding of the insect circulatory system

The insect circulatory system is open, meaning that the hemolymph flows freely throughout the coelem and is not confined to vasculature and vessels as blood is in vertebrates. Circulation functions to transport nutrients, hormones, and metabolic waste, while also aiding in immune function and in response to injury

[6, 12-14]. The insect body is divided by the dorsal diaphragm, separating the small pericardial sinus from the perivisceral sinus which makes up most of the body [6, 15]. Within the pericardial sinus is the dorsal vessel (DV), which is considered the primary pulsatile organ of the circulatory system and is a long tube running just below the dorsal cuticle through the abdomen and thorax of the insect. In addition, many insects utilize small accessory pulsatile organs to pump hemolymph through the thin, micro-scale legs, antennae, and wings [15].

The DV is the largest organ in the insect circulatory system, but it is very small relative to the size of the body and is only half-muscularized. Hemolymph enters the DV through pairs of valves called ostia and through the anterior end of the vessel [6] (Fig. 1.2). Propulsion of hemolymph through the DV is accomplished via peristaltic-like contractions down the length of the abdominal portion of the tube. The DV produces flow mostly anteriorly, although flow direction can be reversed in some species [16]. Despite extensive study on the morphology of the insect DV [6, 17-20] and flow of hemolymph within the DV [21, 22], very little is known about the precise kinematics of the heart wall.

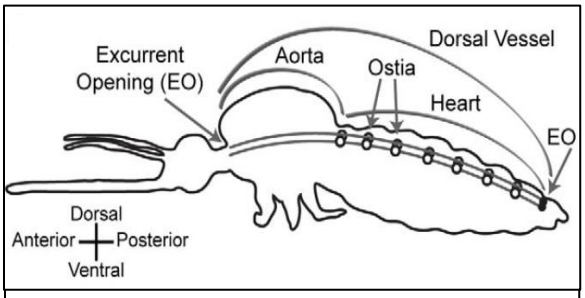

Figure 1.2: Insect body plan showing the position and basic structures of the DV. Figure used with permission from [2].

1.1.3 The importance of hemolymph

Both the insect circulatory and respiratory system involve the transport of fluids through microscale, deformable networks. These systems are surrounded by hemolymph, arguably one of the most important connective tissues within the insect body due to its ability to transmit force between different systems. Hemolymph consists mostly of fluid plasma containing sugars, ions, amino acids, and other inorganic compounds in which cells, termed hemocytes, are suspended [6]. While hemolymph is generally utilized to deliver nutrients, some insects use the transport of hemolymph throughout the coelem to induce collapse of sections of the tracheal network [23, 24] or to thermoregulate active flight muscles [6]. Hemolymph makes up 10-40% of the volume of the insect [6, 12, 25, 26] and surrounds all tissues within the insect, making its flow crucial to an insect's physiology.

Flow of hemolymph within the insect is governed by the physical properties of the hemolymph and the geometry of the circulatory system. These physical properties, such as density, viscoelasticity, and viscosity, can be significantly affected by composition, specifically the ratio of the plasma and cellular components of the hemolymph. In particular, viscosity of a fluid is proportional to the resistance of the fluid to flow and thus, blood viscosity has an inverse effect on blood flow where an increase in viscosity would result in slower flow and vice versa. Blood viscosity has been measured in many vertebrate species [27-36]; however, prior to the work in this dissertation, it was unknown in insects.

1.2 Dissertation overview

The major goal of this dissertation is to study the structure and kinematics of portions of the insect respiratory and circulatory systems to better understand how they function to transport fluids at the microscale. This dissertation uses various experimental and data analysis techniques, including synchrotron x-ray microtomography, b-mode ultrasound videography, detailed image analysis and processing, as well as viscosity, behavioral, and composition measurements.

In Chapter 2, I begin by studying the geometry of the insect tracheal system. This work began several years previously when my advisor, Jake Socha, considered how tracheal system structure may affect tracheal collapse patterns in insects. Murray's law describes the relationship between the size of parent and daughter tubes during branching in biological networks. In this chapter, we address the question, does Murray's law apply to the tracheal system of insects? This chapter uses synchrotron x-ray microtomography and in-depth image analysis to visualize and measure tracheal tube geometry within intact *Platynus decentis* beetles. This study is the first attempt to test if Murray's law applies to the tracheal system of insects. The results found here will provide a deeper understanding of the physiology of the tracheal system and might indicate flow considerations and production within this biological network. I would like to thank a previous graduate student, Vikas Krishnamurthy, who made initial attempts to study Murray's law in insects and provided the starting point for this study.

In Chapter 3, I start to measure and characterize the physical properties of insect hemolymph. Before the circulatory system of insects can be computationally modelled, it is important to obtain the basic properties of both the system and the fluid involved. In this chapter I attempt to answer the question, what is the viscosity of insect hemolymph? And further, since insects can be strongly affected by environmental temperatures, how does temperature affect the viscosity of insect hemolymph? Using a cone and plate viscometer, I measured whole hemolymph viscosity in *Manduca sexta* larvae from 0 to 45°C. This study quantifies the viscosity of insect hemolymph for the first time. In addition, this chapter shows the effect of both shear rate and temperature on the viscosity of hemolymph, both of which can vary within the insect. Hemolymph viscosity and the effects of temperature and shear rate are crucial in understanding the fluid mechanics of hemolymph flow within the coelem of the insect. I would like to thank former graduate student Matthew Giarra and high school student Ellen Granata, who attempted to measure insect hemolymph viscosity a few years ago and provided some of my initial methodology.

In Chapter 4, I provide a further understanding of the effects of environmental temperature on the viscosity of insect hemolymph. Here, I address the question, are hemolymph properties affected by developmental responses to temperature? Insects have many known physiological responses to temperature, including changes in behavior and release of proteins or other chemicals internally. Some of these responses may alter the composition of hemolymph, and thus affect the hemolymph viscosity. I reared *Manduca sexta* larvae at three different temperature regimes before measuring their hemolymph viscosity across a range of temperatures using a cone and plate viscometer. I also measured hemolymph cell volume and other properties. This study will be the first to measure physical properties of hemolymph after the insect has been exposed to temperature extremes, including measuring both viscosity and cell volume. The effect of environmental temperature on hemolymph viscosity could be an underappreciated factor in how insects use physiological mechanisms to cope with changes in temperature, including activity levels, defensive responses, and heart rate.

In Chapter 5, I present a kinematic and structural characterization of the dorsal vessel of the beetle, *Zophobas morio*. This chapter is motivated by the question, what are the wall kinematics of the insect heart? I have used a variety of techniques here including dissection and microtome slicing in order to make physical measurements of the dorsal vessel of this beetle. To visualize and measure the heart in motion, I have analyzed b-mode ultrasound videography of both transverse and longitudinal views of the dorsal vessel. This is the first study to characterize the heart wall kinematics within an insect. Understanding how the heart wall moves will help us understand how it produces flow and ultimately, the full structure and function of the dorsal vessel and the circulatory system.

This dissertation makes significant advancements in our understanding of the structural and physical properties of the insect respiratory and circulatory systems. The insect circulatory and respiratory systems provide potential bioinspiration for microfluidic methods and devices, specifically in biomedical applications. By better understanding how insects achieve flow through their micro-sized features, we can apply new concepts and methods to current biomedical microfluidic applications. For example, the insect dorsal vessel, with its unique ability to move fluid using a peristaltic-like movement of its walls possibly without occlusion, could be used to inspire peristaltic pumps that limit contamination, additional fluid forces, and other issues involved with occlusion of the tube. Outreach activities utilizing the models, visualizations, and 3D reconstructions will foster interest in insect structure and function, an area not regularly thought of as an engineering landscape, as well as promote participation of students in STEM activities. Additionally, this project has furthered interdisciplinary collaboration and study, as it functions directly at the interface of engineering and biology.

Chapter 2

Does Murray's law apply to the tracheal system in insects? A 3D study of the beetle *Platynus decentis*

Manuscript authors: Melissa C. Kenny, Mark A. Stremler, and John J. Socha

Citation: Kenny, M.C., Stremler, M.A., & Socha, J.J. (2019). Does Murray's law apply to the tracheal system in insects? A 3D study of the beetle *Platynus decentis*. *Manuscript in preparation.*

Abstract

The architecture of fluid transport systems has been well studied in many organisms. Diverse taxa have evolved network geometries that tend toward the minimization of energy loss in fluid transport. Optimal network branching design is sometimes reflected in Murray's law, which states that for laminar flow at any branch point, the radius of the parent vessel cubed equals the sum of the cubes of the radii of the daughter vessels. This relationship balances the cost of overcoming viscous resistance to flow with the costs of building and maintaining the system. Murray's law has been found to hold in networks such as mammalian circulatory vessels and the canal system in some species of sponges; however, the applicability of Murray's law has not yet been studied in the tracheal network of insects. We obtained synchrotron microtomography of the beetle *Platynus decentis* at the Advanced Photon Source at Argonne National Laboratory. 3D segmentation of tracheal branching points was performed using Avizo software and the hydraulic radii of both the parent and daughter vessels were measured. We found that Murray's law does not apply to the tracheal system of this beetle species. Considering that insects may utilize mixed respiratory mechanisms that employ both advection and diffusion, measurements of tracheal branching geometry may indicate respiratory function and dynamics within insects.

Keywords: Murray's law, insects, tracheal network, bifurcation

2.1 Introduction

Biological networks are vital for the transport of chemicals, metabolites, waste, and other materials throughout an organism [37, 38]. Networks such as respiratory and circulatory systems can be both morphologically extensive and metabolically expensive, making an optimal structure and design selectively favored [38]. Fluid flow within a network serves to transport materials, but it requires energy for pumping and metabolic investment into building and maintaining the network structure itself. For optimal design, biological networks are expected to balance effective transport via fluid flow with energetic considerations by following three main principles [37]: (1) diffusion through the network walls at exchange sites is limited by the surface area to volume ratio, as described by Fick's Law; (2) large vessels are better suited for bulk flow, owing to the high cost associated with moving large quantities of fluid at high flow rates through small vessels; (3) and flow velocities are reduced at transfer sites, as exchange of materials through the network walls via diffusion occurs over relatively long timescales.

When aligning with these principles, the flow velocity and inner surface area of the network will vary depending on whether each section is needed for bulk flow or as a transfer site. Flow velocity and surface area can each be altered by having the transport network branch frequently, which changes the size and number of tubes [39]. To optimize the design, network architecture may also minimize the cost of vessel branching. Cecil Murray describes the geometry of each branching point in an optimal biological network as [40]:

$$\frac{\sum r^{x}_{\text{parent}}}{\sum r^{x}_{\text{daughter}}} = k \qquad (2.1)$$

with x=3 and k=1. In developing equation (2.1), Murray made several assumptions. First, there is an energetic cost to moving the fluid against the viscous resistance at the vessel wall. Second, there is a cost to build and maintain the system, which is directly related to the volume of the system. Last, there exists some function that maximizes return on the system for these costs. Essentially, Murray proposed that there is an inherent tradeoff between the cost of producing flow and the metabolic cost of maintaining the fluid and system [39]. Making these assumptions in a biological network gives x=3 and k=1 in equation (2.1), resulting in what is known as Murray's law. When these assumptions do not apply, branching geometry is still optimized in some networks assuming k=1, but with different values of x [41]. For example, in an optimal system with turbulent flow, x is 2.33 [42]; for large transport vessels or diffusion-dominated flow, x is 2.0 [39, 43]; and with convective heat transfer, x is 1.0 [44]. Additionally, with increased network permeability, x will increase [45, 46], and with rarefied flow, x will decrease [47, 48]. Many biological networks have been found to satisfy Murray's law, such as sunflower leaf venation [49], chick embryo vasculature [50], plant water transport systems [38], the mammalian circulatory system [39], stromatoporoid water exchange systems [51], and the conducting zone of the mammalian respiratory system [45, 46]. However, many other networks, such as the insect tracheal system, remain unstudied.

The insect respiratory system functions by delivering oxygen directly to tissues within the animal using a network of internal tracheal tubes [52]. The tracheal system begins with spiracular valves on the abdomen and thorax that connect to large tracheae, which eventually branch to small, micrometer-diameter tracheoles that serve as primary diffusive exchange sites [6]. Historically, the transport of O_2 and CO_2 was thought to

be diffusion dominated, but many insects are capable of creating advective flows, facilitated by mechanisms of active ventilation, including rhythmic tracheal compression [7-10].

The morphology of the insect tracheal system has been poorly studied, perhaps due to the limitations of dissection, which alters the internal environment of the insect and shape of the tracheal tubes. However, with improved x-ray technology that allows for fine imaging resolution [7, 9, 10], in recent years the tracheal system has been visualized in greater detail and tracheal branching patterns can be studied without disruption. Here, we report the first test of Murray's law on the geometry of an insect tracheal system. We used synchrotron microtomography to obtain three-dimensional images of intact *Platynus decentis* adults that were used to identify branching points within their tracheal network and measure the radius of the tracheal tubes. With these images, we were also able to measure the cross-sectional shape of each tracheal tube. Traditionally, elliptical tubes were considered 'compressible' [53], suggesting tube shape may be indicative of respiratory dynamics. Exploration of the geometry of the insect tracheal tube network may further our understanding of optimal biological networks.

2.2 Methods

2.2.1 Animals

Platynus decentis adults were used for this study, as they are known to use active ventilation in addition to diffusion [9]. Beetles were wild-caught in pitfall traps from the woods surrounding the Advanced Photon Source at Argonne National Laboratory (Lemont, IL, USA). They were kept in tanks with soil and offered generic dry dog food and water *ad libitum* for up to a month until experiments were conducted.

2.2.2 Imaging and data collection

Animals were imaged using synchrotron x-ray phase-contrast micro-computed tomography (SR-μCT) at beamline 2-BM at the Advanced Photon Source. Animals were sacrificed with fumes of ethyl acetate and immediately mounted in polyimide tubing (Kapton, Dupont, Wilmington, DE, USA), with sticky tack used to seal both ends of the tube. Each sample was chilled at 4°C for 1-2 hours to halt any residual internal movements, and then rewarmed to room temperature for 30 min before imaging. Images were recorded with a 200 ms exposure time using a 2048 x 2048 px cooled-CCD sensor (CoolSNAP, Photometrics) with 1 μm resolution. 1400 raw projections were taken as the sample was rotated over 180° at increments of 0.125°. The x-ray beam supplied monochromatic light with 12-18 kEv energy, using a sample-to-detector distance of 30-100 mm. Imaging took approximately 30 min per sample, and reconstructions were made with attenuation only. The tracheae were relatively easy to visualize and identify in these scans due to the distinct change in density from internal organs to the air within the tubes (Figure 2.1A) [7, 54].

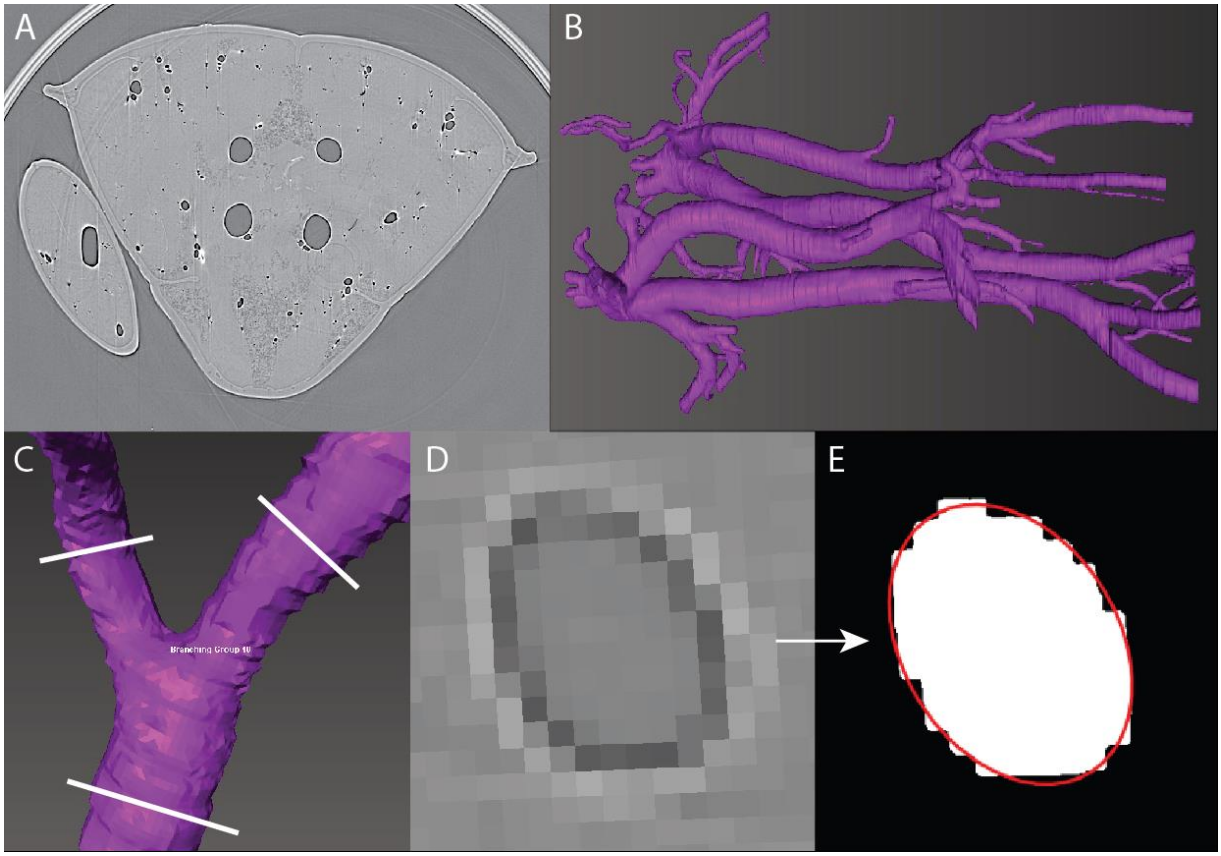

Figure 2.1: Analysis of the synchrotron microtomography scans of *P. decentis* adults. Cross-sectional tomographic images (A) show tracheal tubes, which were reconstructed in 3D (B). For each branching group, an orthogonal slice of each tube, as indicated by white lines in (C), was obtained. These cross-sectional images of the tubes (D) were processed to create binary images, and an ellipse was fit to the tube cross section (E).

2.2.3 3D segmentation and measurement

Volume rendering using Avizo software (Thermo Scientific, U.S.) was used to segment and measure the tracheal tubes. Locations where tracheae transitioned from one trunk to two or three trunks (hereafter, 'tracheal branching points') were identified by searching through the reconstructed images (such as the example shown in Figure 2.1A) and manually following a tube until it branched. Each branching group, consisting of the parent trunk and daughter trunks at each tracheal branching point, was segmented in 3D to a length of approximately two to three times the diameter of the tube. The Slice tool was used to rotate the plane of view to obtain an orthogonal cross-section of each tube approximately one to two diameter lengths away from the branching point (Figure 2.1C). Differences in pixel intensity between the tube wall and air within correspond to discontinuities in the refractive index during phase contrast imaging, leading to phase jumps that cause Fresnel diffraction [55-57]. These phase jumps appear as white-black fringes in the x-ray image at the edge of the tube (Figure 2.1D). We assumed that the location of the tube wall was located between dark and light pixels in the cross-sectional image [55-57].

Using MATLAB, a circular averaging filter (pillbox) with a square matrix of size three pixels was first applied to each cross-sectional image for easier analysis of the pixelated images. A gray threshold was used on each cross-sectional image to generate a binary image of the cross-section of the tube, where the inside of the tube was represented by white pixels. An ellipse was then fit to the cross-section (Figure 2.1E). The major and minor axis radii of the ellipse were recorded. In order to obtain a single, representative measure for each tube, the hydraulic radius was calculated as $R_H=A/P$, where A is the ellipse area and P is the ellipse perimeter. Following Westneat et al. [9], the ellipse perimeter was calculated using Ramanujan's approximation [58];

$$P = \pi(a+b)\left(1+\left(\frac{3\left(\frac{(a-b)^2}{(a+b)^2}\right)}{10+\sqrt{4-3\left(\frac{(a-b)^2}{(a+b)^2}\right)}}\right)\right) \qquad (2.2)$$

where a is the major axis radius and b is the minor axis radius. In addition, the ratio of the major and minor axis radii, termed the 'shape ratio' in this study, was used to quantify the cross-sectional tube shape.

Of the five animals examined, 131 branching groups were identified and analyzed with 14-46 groups in each animal. The majority of branching groups consisted of a single parent tube and two daughter tubes, although each animal contained up to 3 branching groups with three daughter tubes. Forty-one branching groups were segmented in the head and 86 in the thorax across all five animals. Only 3 branching groups were segmented in the abdomen, as abdominal tracheal tubes were much smaller and more difficult to locate than in other areas of the insect body. In total, 400 tubes were segmented across the five animals. Tubes ranged in size from a maximum major axis radius of 94.1 μm to a minimum minor axis radius of 6.6 μm, with the hydraulic radius ranging from 3.9 to 45.0 μm.

2.2.4 Statistical analysis

R (Foundation for Open Access Statistics) was used for all statistical analyses. One-way t-tests (TT) were used for comparisons of values. A linear model (LM) was used to test for the effect of one variable upon another. Analysis of variance (ANOVA) was used to compare values to determine any differences in mean. A Box-Cox transformation was used as needed to transform variables to normal. Nonlinear least-squares estimation (NLS) was used to determine the exponent of best fit. To determine which means differed in a multiple comparison ANOVA, post-hoc analysis was done using Tukey's HSD.

2.3 Results

The value of k in equation (2.1) with x=3 was found to be 1.29 on average, with a 95% confidence interval of 1.23 to 1.34, which is significantly different than 1 (TT: df = 127, $p < 0.0001$)(Figure 2.2). There were no differences in k with x=3 due to location of the branching group, number of daughter tubes, or animal (Table 2.1). Size of the parent tube also did not affect k with x=3 (LM: F = 0.2611, df = 126, p = 0.61). A

best fit x for equation (2.1), with k=1, was calculated to be 2.14, with a 95% confidence interval of 2.05 to 2.26 (NLS: df = 127, $p < 0.0001$; Figure 2.3).

Table 2.1: Summary of ANOVA comparing k with x=3 for animal, number of daughter tubes, and location.

Source	df	MS	*F*	*P*
Animal	4	0.008032	0.282	0.889
Number of daughter tubes	1	0.003291	0.115	0.735
Location	2	0.002481	0.087	0.917
Residuals	120	0.028505		

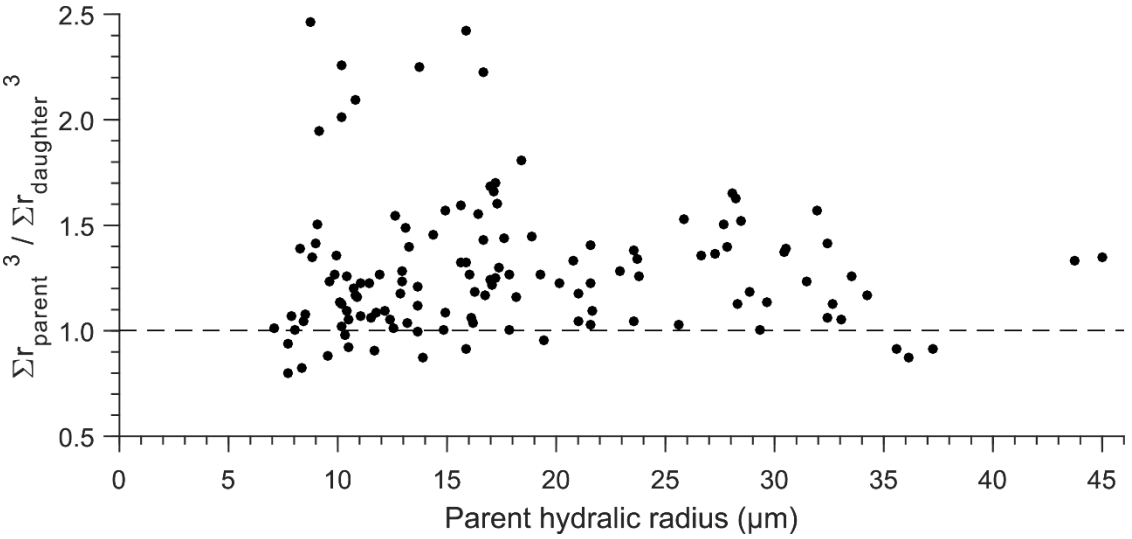

Figure 2.2: Murray's ratio (equation 1 with x=3) as a function of parent hydraulic radius for each branching group. A value of k=1 (dashed line) indicates congruence with Murray's law.

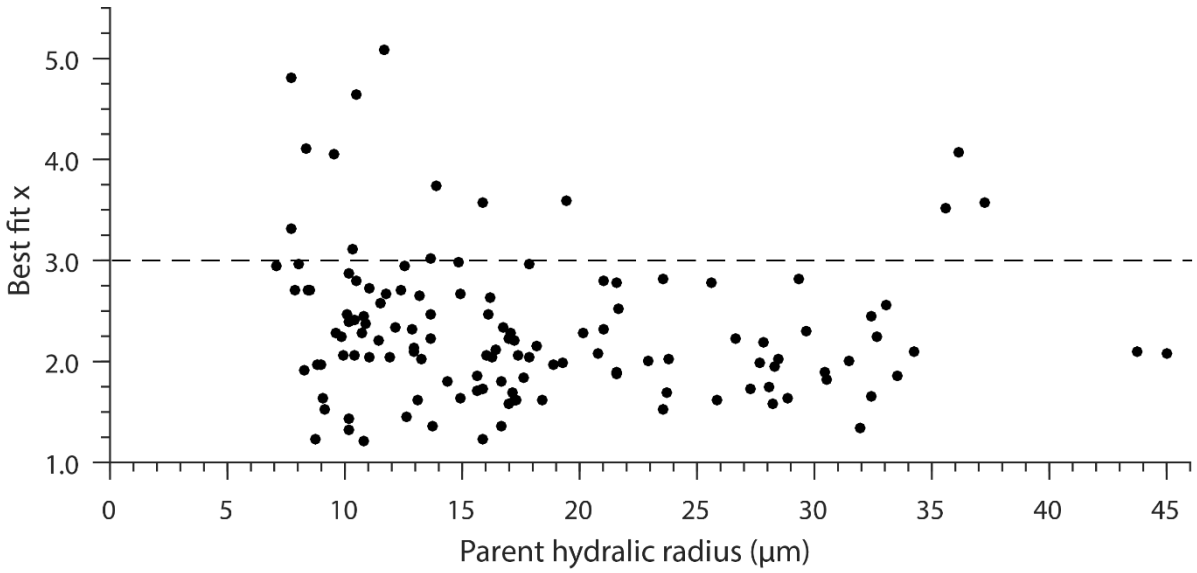

Figure 2.3: Best fit x (equation 1 with k=1) as a function of parent hydraulic radius for each branching group. A value of x=3 indicates congruence with Murray's law (dashed line).

Tracheal tubes were found to be slightly elliptical (Figure 2.4), with an average shape ratio of 1.21, with a 95% confidence interval of 1.19 to 1.23, which is significantly different than 1 (TT: df = 390, $p < 0.0001$). Although parent and daughter tubes did not differ significantly in shape (Table 2.2), larger tubes tended to be more circular (Figure 2.4; LM: F = 6.257, df = 389, $p < 0.02$). Tubes in the head were only 4% more elliptical than those in the thorax, but this difference was statistically significant. In addition, tracheal tubes in one animal were significantly more circular than the other animals tested (Table 2.2).

Table 2.2: Summary of ANOVA comparing shape ratio for animal, tube type, and location. Post-hoc analysis was done using Tukey's HSD.

Source	df	MS	*F*	*P*
Animal	4	0.05074	17.781	<0.0001
Tube type (parent or daughter)	1	0.00014	0.049	0.82558
Location	2	0.01512	5.300	0.00537
Residuals	383	0.00285		

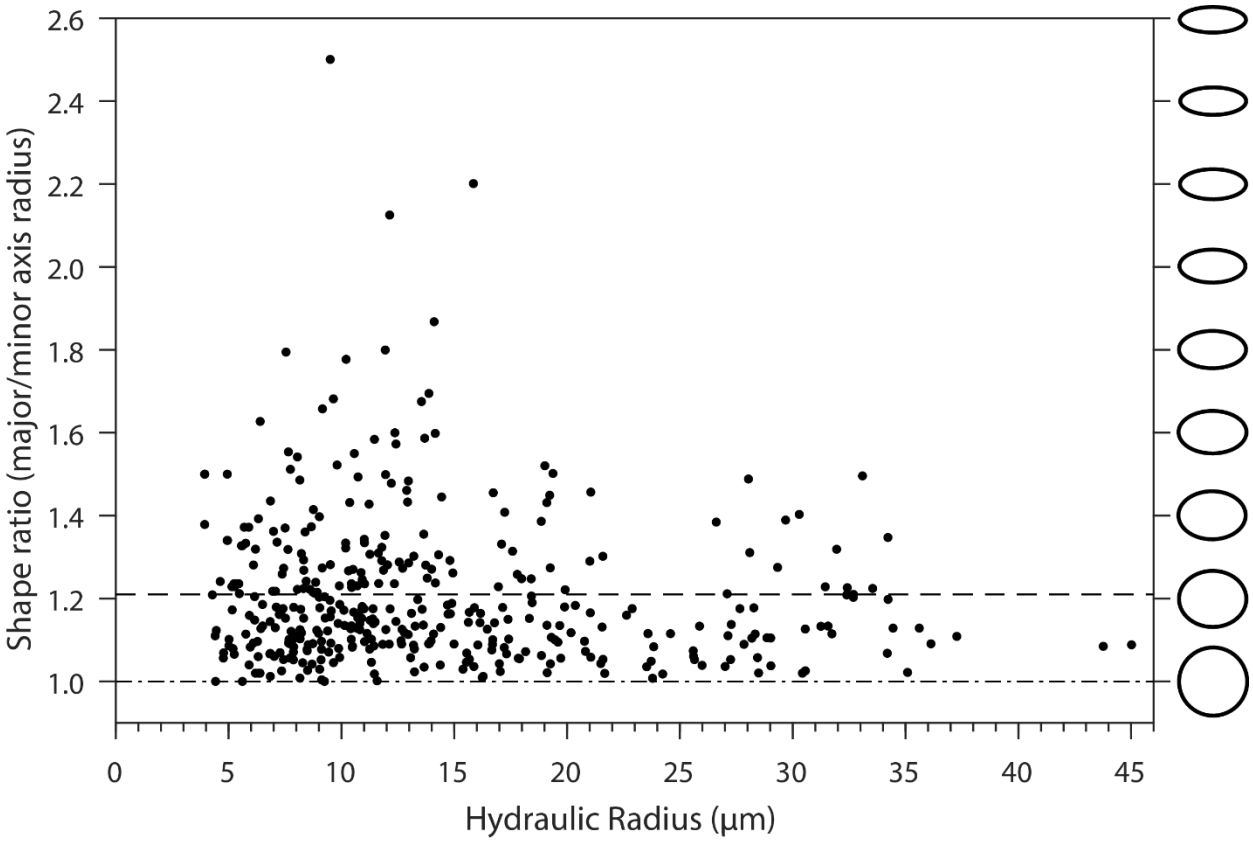

Figure 2.4: Shape ratio (major to minor axis radius) as a function of hydraulic radius for each tube. A shape ratio of 1 (dash-dotted line) indicates a trachea with circular cross-sectional shape. These data had an average shape ratio of 1.21 (dashed line). Representative ellipses for each shape ratio are shown to the right.

2.4 Discussion

Optimization of the design of biological transport networks is advantageous for organisms, as it balances the cost of producing flow and the metabolic cost of maintaining the fluid and system. This includes optimizing the network architecture to minimize the cost of vessel branching. While the applicability of Murray's law (x=3, k=1) across many biological transport networks is well known, in this study, we have shown that Murray's law does not apply to the tracheal system of *Platynus decentis* adults. It appears that the assumptions of Murray's law do not apply to the insect tracheal system, warranting a different geometry. For example, methods of flow generation or metabolic maintenance costs within the tracheal system may differ from other biological networks.

The biological networks whose structure follows Murray's law employ continuous, active methods of flow generation, which is not necessarily the same in the insect tracheal system. Insects can use a combination of active ventilation and diffusion in their tracheal system to produce flow. *Platynus decentis* adults, in particular, are known to experience rhythmic tracheal compression [9], which has been associated with gas exchange in the tracheal network [59]. Moreover, respiration in insects is not always continuous [60, 61]. Some insects utilize active methods to generate bulk flow, followed by a pause which may facilitate diffusion of oxygen to tissues through the tracheal walls. Thus, the insect respiratory system is a mixed system, where diffusion occurs continuously but bulk flow may occur only during some times [60, 61]. Murray's law assumes there is an energetic cost to the organism to move fluid against the viscous resistance of the vessel wall, which would hold true for active flow mechanisms employed by the insect; however, diffusion of gas through the insect tracheal system would not follow this assumption. Although gaseous diffusion would not require work from the organism, network design would tend towards minimization of resistance, with an optimum design at x=2 (with k=1) in equation (2.1) [39].

In addition, for optimal network design, Murray's law assumes there is a cost for the organism to maintain the biological network throughout its functional life. However, it has long been assumed that tracheal size is fixed after development in insects, based on the fact that tracheae are lined with a layer of cuticular cells [6]. This assumption implies that the energy required for the metabolic maintenance of the tracheal system may be minimal after its initial development. However, although it is unknown in *Platynus decentis*, in *Manduca sexta* larvae, the structural investment and volume of the tracheal system increase during growth [62]. Oxygen deprivation can trigger growth responses in tracheal epithelium throughout post-embryonic development, creating a constant expansion of the tracheal system [62, 63]. Throughout larval growth in many insects, the length of the tracheae increases steadily [62, 64]. After damage to the tracheal system, insect tracheoles migrate toward the oxygen-deficient area, drawing tracheae after them [65]. Thus, the insect tracheal system will respond and grow to locations of hypoxia [6, 11], incurring a metabolic cost to the insect for adequate oxygen delivery to tissues, and Murray's assumption about the cost of metabolic maintenance of the network holds true. However, whereas tracheae and tracheoles will grow in length throughout development, increases in tracheal diameter and formation of new tracheoles occur only at each molt [62, 64, 65]. The geometry of the tracheal system changes drastically during molts, increasing the cost of metabolic maintenance of the network at such times, despite the cost of flow production potentially remaining the same. The balance between the cost to move fluid and to maintain the network assumed for Murray's law systems may be affected, resulting in a different network geometry.

Further, there is no metabolic cost in insects to maintain the air that fills the tracheal network, only a potential cost in maintaining the tubes themselves. Murray's derivation has been shown to hold for biological systems in which the flowing fluid is inert, as in the lungs and as it is here, but only if the thickness of the tube walls are a function of the radius [39]. Previous morphological studies in the stick insect *Carasius morosus* have shown that tracheal tube thickness is generally related to the size of the tube [66]; however, it can vary with location, with thicker tubes found where tracheae are free in the hemolymph or along the surface of an organ [66, 67]. The energy for metabolic maintenance in insects that use active ventilation may be proportional to the surface area of the tubes rather than their volume, which would change the x to 2.5 in equation (2.1) with k=1 for an optimal network structure [44].

Tracheal cross-sectional shape may also provide insights into the ventilatory mechanisms used by these insects. The tracheal tubes were found to be significantly elliptical overall, with an average shape ratio of 1.21 (Figure 2.4). This finding is in contrast to traditional thought, where the tube cross-section has been assumed as circular, especially in studies calculating tracheal volume within insect body segments [68]. An elliptical tube cross-section with a shape ratio of 1.21 is 17% smaller in area than a circular tube with the same major axis radius and 21% larger in area than a circular tube with the same minor axis radius. This creates a significant change in calculations of tracheal volume from cross-sectional views of tracheal tubes; however, our three-dimensional data show that tube shape ratio varies with tube size, with larger tubes more circular than smaller tubes, and thus the total volume calculation may be greatly affected. In addition, this difference in tracheal tube shape may correlate with flow methods through each tracheal tube. Classically, circular tracheae have been identified as supplying oxygen via diffusion only and it was assumed they experienced little deformation [7, 69]. In contrast, tracheae with an oval cross-sectional shape were described as serving ventilatory purposes (termed 'respiration tracheae' or 'ventilation tracheae') and may collapse [1, 53, 69]. These 'ventilation tracheae' were identified as being involved in convective airflow via tracheal collapse or deformation [70]. However, synchrotron x-ray videos have shown larger tubes collapsing in some insects [54], indicating that circular tracheal tubes may also provide ventilatory mechanisms via collapse in insects. Further study of tracheal tube shape, size, and collapse patterns are needed to determine any correlations.

While this study only examines a single insect species and single developmental stage, the methods used here can be used to study a larger variety of insect tracheal networks. Tremendous variation exists in both tracheal morphology and respiratory dynamics among insects, ranging from advective- to diffusion-dominated species [6, 7, 23]. Currently, in order to understand gas exchange dynamics, studies have focused on external measurements of the animal, such as CO_2 and H_2O emission [71], airflow at the spiracles [72], patterns of spiracle opening and closing [73, 74], and exoskeleton movements [75]. Despite these studies, the roles of convection and diffusion as a function of body size, phylogeny, development, and life history, remain poorly understood [7]. Measurement of tracheal tube shape and branching geometry using microtomography and volume rendering is simple and fast, and more importantly, does not deform internal structures. Synchrotron x-ray tomography is only limited by its resolution, resolving tracheae as small as 3.5 μm in diameter [1]. Measurements of tracheal network geometry in additional insect species that use varying methods of respiration may illuminate a relationship between tracheal geometry and respiratory dynamics. If flow in the tracheal system is driven by diffusion, then x=2 in equation (2.1)[39, 44] for optimal network design. However, if flow is due to active flow generation, then the geometry of an optimal network follows Murray's law with x=3. With x=3, the volume of the system is conserved at each branching point, whereas with x=2, cross-sectional area is conserved. As x decreases in equation (2.1) with k=1, the surface-

to-volume ratio through subsequent network branches will increase. Within the tracheal network, a larger surface area to volume ratio will increase delivery of CO_2 and O_2 to internal tissues [76]. The best fit x in equation (2.1) of the insect tracheal system tested here was 2.18, which suggests that transport is still predominantly diffusive within the system, despite evidence of advective flow [9], and that conservation of tracheal surface area is advantageous for gas exchange [76]. If tracheal network geometry through branching groups is indicative of flow type within the insect, this may be a new method of determining respiratory dynamics across insect phylogeny.

Acknowledgements

We acknowledge the assistance of Vikas Krishnamurthy, Brittany Horton, and Padraic Flynn as well as Kathy Tinoco with Avizo support. Also, the Statistical Applications & Innovations Group (SAIG) at VT was integral to the completion of statistical analyses. In particular, we thank Talia Weiss for help with analysis of images and Khaled Adjerid and Joel Garrett for discussion. This work was supported by the National Science Foundation under grants 1558052, 0938047, and 0966125.

Chapter 3

How temperature influences the viscosity of hornworm hemolymph

Manuscript authors: Melissa C. Kenny, Matthew N. Giarra, Ellen Granata, and John J. Socha

Citation: Kenny, M. C., Giarra, M. N., Granata, E., & Socha, J. J. (2018) How temperature influences the viscosity of hornworm hemolymph. *Journal of Experimental Biology*, **221**(21). doi: 10.1242/jeb.186338.

Abstract

Hemolymph is responsible for the transport of nutrients and metabolic waste within the insect circulatory system. Circulation of hemolymph is governed by viscosity, a physical property, which is well known to be influenced by temperature. However, the effect of temperature on hemolymph viscosity is unknown. We used *Manduca sexta* larvae to measure hemolymph viscosity across a range of physiologically relevant temperatures. Measurements were taken from 0 to 45°C using a cone and plate viscometer in a sealed environmental chamber. Hemolymph viscosity decreased with increasing temperature, showing a 6.4x change (11.08 to 1.74 cP) across the temperature range. Viscosity values exhibited two behaviors, changing rapidly from 0 to 15°C and slowly from 17.5 to 45°C. To test the effects of large particulates (e.g. cells) on viscosity, we also tested hemolymph plasma alone. Plasma viscosity also decreased as temperature increased, but did not exhibit two slope regimes, suggesting that particulates strongly influence low-temperature shifts in viscosity values. These results suggest that as environmental temperatures decrease, insects experience dramatic changes in hemolymph viscosity, leading to altered circulatory flows or increased energetic input to maintain similar flows. Such physical effects represent a previously unrecognized factor in the thermal biology of insects.

Keywords: viscosity, hemolymph, temperature, insects

3.1 Introduction

Blood is a critically important connective tissue in the animal body, delivering necessary nutrients to organs and cells, protecting from foreign bodies, removing metabolic waste, and repairing injury [12, 14]. In insects, the blood and lymphatic fluid comingle as hemolymph within an open circulatory system [6, 13], with flow governed by the geometry of the circulatory network and the physical properties of the hemolymph itself. These physical properties include viscosity and density, which are biologically important because they directly influence the energetic requirements of flow production and patterns of flow throughout the body within an open circulatory system [77, 78]. Blood viscosity has been measured in many vertebrates, including mammals [27, 35], fish [28, 31, 34], reptiles [30, 33, 79], amphibians [32], and birds [29, 36]. However, perhaps owing to the presence of an open system, blood viscosity is generally unstudied in invertebrates [80] and is unknown in insects.

Changes in blood viscosity can lead to physiological problems related to circulation. For example, hyperviscosity syndrome in humans results in decreased cardiac output, which increases the chance of mucosal hemorrhage, visual abnormalities, neurological anomalies, and cardiac failure [81]. Such problems arise from changes in blood composition (specifically, cell count), but the viscosity of any fluid also depends on external physical factors including pressure, shear rate (for non-Newtonian fluids), and temperature. The temperature dependence of viscosity is well known, with a general trend of increasing viscosity as temperature decreases. For example, human blood viscosity increases by a factor of nearly five when measured from 37 to 0°C [82], a change which could in theory retard flow by a factor of fifteen [83]. However, as endotherms, most mammals actively thermoregulate, maintaining precise internal body temperatures (with fluctuations of ~1°C [84]), meaning that large changes in blood viscosity should never be experienced by mammals under most non-pathological conditions.

Insects, however, are poikilotherms, whose body temperature varies with the external environment. Temperature affects many aspects of insect physiology, such as activity [85, 86], foraging [87], flight [88], courtship calling [89], mating [90], and territorial behavior [91]. Changes in activity due to temperature can also lead to secondary effects, including changes in critical thermal minimum and chill injury [92], as well as life span [93]. Despite its importance in insect physiology, the role of temperature-driven changes in hemolymph viscosity has never been considered. Hemolymph comprises up to 45.4% of the volume of the insect [6, 12, 25, 26, 94], and it must be pumped by the heart and accessory pulsatile organs, and move throughout the coelem and into micro-sized spaces such as the long and thin antennae, legs, and delicate wing veins [6, 16]. Correspondingly, flow speeds can range by orders of magnitude [21], resulting in fluid behavior that spans from inertia-dominated to viscosity-dominated. This characteristic suggests that changes in hemolymph viscosity mediated by temperature could significantly affect the circulation of hemolymph throughout the open circulatory system of insects.

Here, we report the first measurements of viscosity of insect hemolymph, and specifically address its temperature dependence. We measured hemolymph viscosity of *Manduca sexta* larvae across a physiologically relevant range of temperatures spanning from 0 to 45°C [85]. To further characterize its properties, we also measured density and varied shear rate at a single temperature. Considering the importance of the circulation of hemolymph, viscosity of the hemolymph and possible temperature-mediated changes in viscosity may represent an important factor in the physiology of insects.

3.2 Methods

3.2.1 Animals

Manduca sexta larvae were obtained from an established colony at the University of Washington, shipped to Virginia Tech overnight in individual containers within an insulated box. The larvae of this species were chosen for their short, well-studied life cycles, and because their large size enabled us to obtain sufficient hemolymph for testing (about 700 µL per animal). They were reared individually at room temperature (21-23°C) and given access to food *ad libitum* (Hornworm Diet, Carolina Biological Supply Company, North Carolina) until they were at least 8 g in mass and had reached the fifth instar of their developmental cycles.

3.2.2 Experimental set-up

Viscosity measurements were conducted with a cone and plate viscometer (DV-II+ Pro, Brookfield Engineering, Massachusetts, USA) (Fig. 3.1). Trials were performed with either a CP-40 or CP-51 spindle (Brookfield Engineering, Massachusetts, USA), which are designed for different ranges of viscosity. Because viscosity values may depend on shear rate (e.g., mammalian blood is shear-thinning [82]), we chose spindle rotation speeds to produce reliable measurements and keep shear rates as consistent as possible (Table B.2.1). The CP-40, referred to hereafter as the low viscosity spindle, was used to measure viscosity values from 0.51-5.12 cP; it was operated at 60 rpm, producing shear of 450 s^{-1}. The CP-51, referred to hereafter as the high viscosity spindle, was used to measure viscosity values from 4.05-40.45 cP; it was operated at 120 rpm, producing shear of 460 s^{-1}.

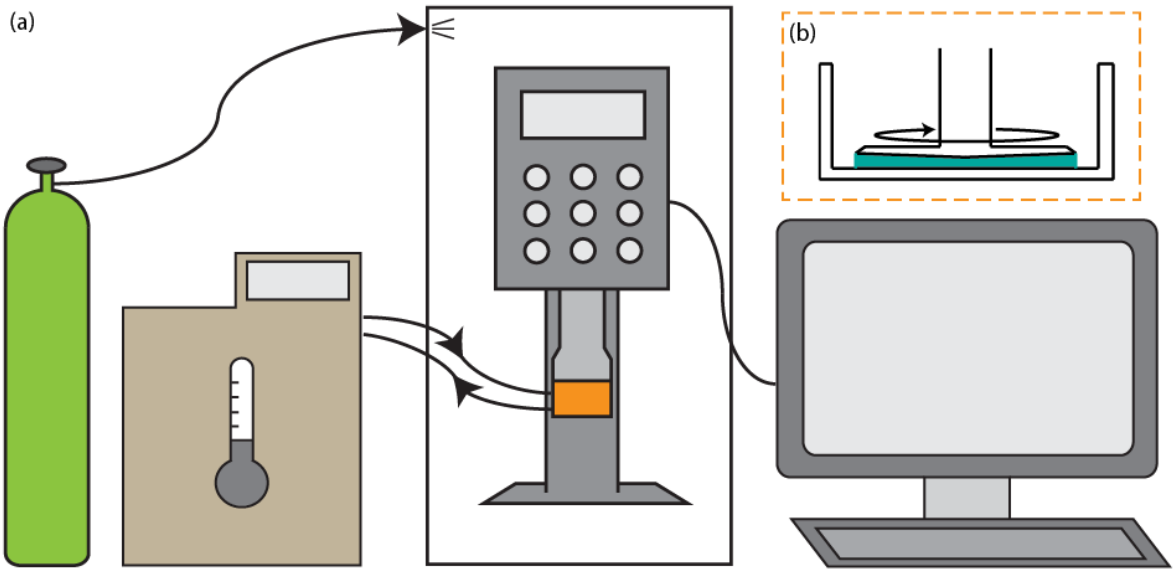

Figure 3.1: Diagram of experimental set up (a), showing (left to right) the nitrogen gas tank, the temperature control circulatory bath, the environmental chamber with viscometer, and the computer. Inset in top right corner (b) shows the cross-section of the viscometer cup and spindle with blue-green hemolymph shown in the gap between (gap size is not to scale).

Temperature was controlled to the nearest 0.1°C using a chiller/heater circulator (RE 206, Lauda, Germany), which provided a constant flow of aqueous glycol through an internal chamber of the viscometer cup. We chose 0-45°C as the temperature range for measurements based on the lower (0°C) and upper (45°C) critical lethal limit for *M. sexta* [85], with trials performed at 5°C intervals. Additional trials were conducted at 17.5°C to provide further resolution on an apparent change in behavior in viscosity from 15 to 20°C. At each temperature, we recorded data from five samples, with one sample per individual.

To minimize oxygen-induced clotting, the viscometer was placed within a sealed environmental chamber (CleaTech Critical Laboratory Supplies, California, USA), which was flooded with dry nitrogen gas (Airgas, Virginia, USA). Oxygen concentrations within the chamber were kept below 2%, verified with an oxygen sensor (Expedition X O2 Analyzer, OxyCheq, Florida, USA). Humidity within the chamber was maintained at 60-80% using a small humidifier (Ultrasonic Cool Mist, Pure Enrichment) and measured with a hygrometer (Traceable, Fisher Scientific, New Hampshire, USA).

3.2.3 Experimental protocol

To extract a sample, larvae were first anesthetized by being placed in the environmental chamber and exposing them to nitrogen gas for 5 to 10 minutes. While still within the chamber, a small incision was made through the ventral exoskeleton of the animal between the second and third sets of prolegs. Hemolymph was dripped onto parafilm (Pechiney Plastic Packaging, Wisconsin, USA), and 0.7 mL was transferred to the cup of the viscometer via pipette. Because the incision site was close to the gut and fat bodies, some samples were contaminated by brown gut contents or white fat and were not tested. The viscometer required a minimum of 0.5 mL of fluid for measurements; we chose to use a slightly greater amount (0.7 mL) to account for the removal of potential contaminants, such as small bubbles that formed when placing the hemolymph within the cup. The time from incision to the start of the viscosity measurement was less than two minutes. Following each trial, any visible changes in the sample that may have occurred during testing were observed and recorded, such as the formation of thrombi (clots) (Fig. B.2.1).

Between each trial, the spindle and cup were cleaned using Kimwipes (KimTech Science Brand, Kimberly-Clark Professional, Georgia, USA) and distilled water. We also performed a control experiment between each trial, wherein we measured the viscosity of 0.7 mL of distilled water and compared the measurements with published values. If our control measurements deviated from published values by more than 5%, the cleaning procedure and control trial were repeated.

In addition to testing whole hemolymph, we measured the viscosity of the plasma portion of the hemolymph using separate trials and specimens. To obtain the plasma, we first extracted a hemolymph sample using the same method as previously described. Each hemolymph sample was centrifuged (Mini Centrifuge Mini-10k+, Miulab, China) for 5 minutes at 10,000 rpm two times, separating the supernatant after each round. The final supernatant, which we consider to be the plasma, was isolated via pipette and tested in the viscometer. Removal of cells was verified via cell counting (Vi-Cell Cell Counter, Beckman Coulter, USA) from five 1 mL samples of 9:1 dilutions of whole hemolymph and plasma with an anticoagulant (98 mM NaOH, 186 mM NaCl, 1.7 mM EDTA, 41 mM citric acid, pH 6.8 [5]). Average cell volume was 7.05×10^6

$\pm$ 1.64 x 10^6 cells/mL for whole hemolymph and 3.90 x 10^5 $\pm$ 2.2 x 10^5 cells/mL for plasma, indicating that centrifugation removed 94.5% of cells.

3.2.4 Data collection and processing

During each trial, viscosity data were recorded at 2 Hz. The raw instantaneous viscosity values over time were processed using a custom MATLAB code to identify durations when the viscosity was steady. We quantified such periods by calculating a sliding window standard deviation of the raw viscosity values over a 75 second period centered on each data point, and then considered those points whose standard deviation was less than 0.05 cP as steady. The representative viscosity value for each sample was calculated as the average of all steady values for its trial. If the viscosity was not found to be steady, the trial was not included for analysis. In total, 96 trials were performed with whole hemolymph, and 55 trials yielded steady values. For plasma, 67 trials were performed, and 50 trials yielded steady values. See Fig. B.2.1 for representative traces and Fig. B.2.3 for all trials.

Generally, viscosity values equilibrated within two to fifteen minutes and were run for at least three minutes once they appeared steady. Trials were not run for longer than 25 minutes total, yielding a total range of 9-25 minutes across trials. Plasma trials took less time to equilibrate on average and had a range of 3-23 minutes in total trial length. In some trials, the measured viscosity increased rapidly for anywhere from a few seconds to a few minutes. The exact cause of these fluctuations is unknowns, but they may have been due to the formation of one of more clots, which were found free-floating in some samples post-test. Many of the whole hemolymph trials and only a few of the plasma trials showed the formation of such clots, which ranged in size from 0.4 to 8.6 mm (Fig. B.2.1).

3.2.5 Varying shear rate

In a second set of trials, we tested whole hemolymph and plasma at multiple shear rates, controlled by varying the rotation speed of the spindle. Trials were begun at 15 or 30 rpm with 15 or 30 rpm increases until reaching 120 or 135 rpm, representing a 112.5 to 1012.5 s^{-1} range of shear rates. For some trials, the lowest or highest shear rate measured viscosity values outside of the instrument's range and were unable to be measured (Table B.2.1). A representative viscosity was determined for each shear rate using the same technique described previously. All trials were performed at 25°C using the low viscosity spindle.

3.2.6 Density measurements

The density of whole hemolymph at room temperature was calculated by measuring the weights and volumes of additional samples. Hemolymph was extracted as before, allowing the fluid to collect onto parafilm. A 0.3 mL syringe with needle was first weighed, then loaded with 0.05-0.29 mL of hemolymph depending on the amount that was obtained from the animal. In total, 99 larvae were tested ranging in age from 17-37 days at room temperature (22°C). As a control, the density of distilled water at 22°C was also measured (n=10) using the same method.

3.2.7 Statistical analysis

RStudio (Foundation for Open Access Statistics) was used for all statistical analyses. One-way t-tests (TT) and paired t-tests (PT) were used for comparisons of values. A linear model (LM) was used to test for the effect of one variable upon another. A linear model with logarithmic transform was used to fit an exponential model to the viscosity versus temperature data, as is regularly used to parameterize the temperature dependence of liquid viscosity [95]. For the trials with varying shear rate, each trial did not yield a value at every measurable shear rate, so a linear mixed model (LMM) was used both with and without shear rate considered; an ANOVA compared these two models to test for an effect of shear rate on viscosity values.

3.3 Results

3.3.1 Effect of temperature on viscosity of whole hemolymph

As temperature increased from 0 to 45°C, the average viscosity of whole hemolymph decreased from 11.1 to 1.7 cP (Fig. 3.2, LM: $p < 0.0001$), representing a 6.4x change across temperature. There appeared to be a steeper decline in viscosity at lower temperatures (0-15°C; 11.1 to 5.1 cP) than at higher temperatures (17.5-45°C; 3.5 to 1.7 cP). To quantify this difference, a continuous piecewise exponential model with a single break point was fit to the data (Fig. B.2.2, LM with a logarithmic transform of viscosity following [96], $R^2 = 0.92$) yielding the following relationship:

$$\mu_w = \begin{cases} 11.8e^{-0.0663T} & \text{for } T \leq 22.7℃ \\ 4.10e^{-0.0196T} & \text{for } T > 22.7℃ \end{cases}, \quad [3.1]$$

where μ_w is the viscosity of whole hemolymph in centipoise (cP) and T is the temperature in °C. The viscosity of whole hemolymph was greater than that of water at all temperatures (Fig. 3.2, PT: $p < 0.005$).

The relative viscosity of whole hemolymph compared to water shows a distinct change between high and low temperatures, but follows a different trend than seen in whole hemolymph (Fig. 3.3). At low temperatures (0 to 17.5°C), relative viscosity decreased with increasing temperature with a slope of $-0.17°C^{-1}$ (LM: $p < 0.0001$), but at high temperatures (17.5 to 45°C), temperature was not correlated with relative hemolymph viscosity (LM: $p = 0.344$). On average, the viscosity of whole hemolymph at high temperatures (17.5 to 45°C) was 2.90 ± 0.46 (mean ± SD) times the viscosity of water.

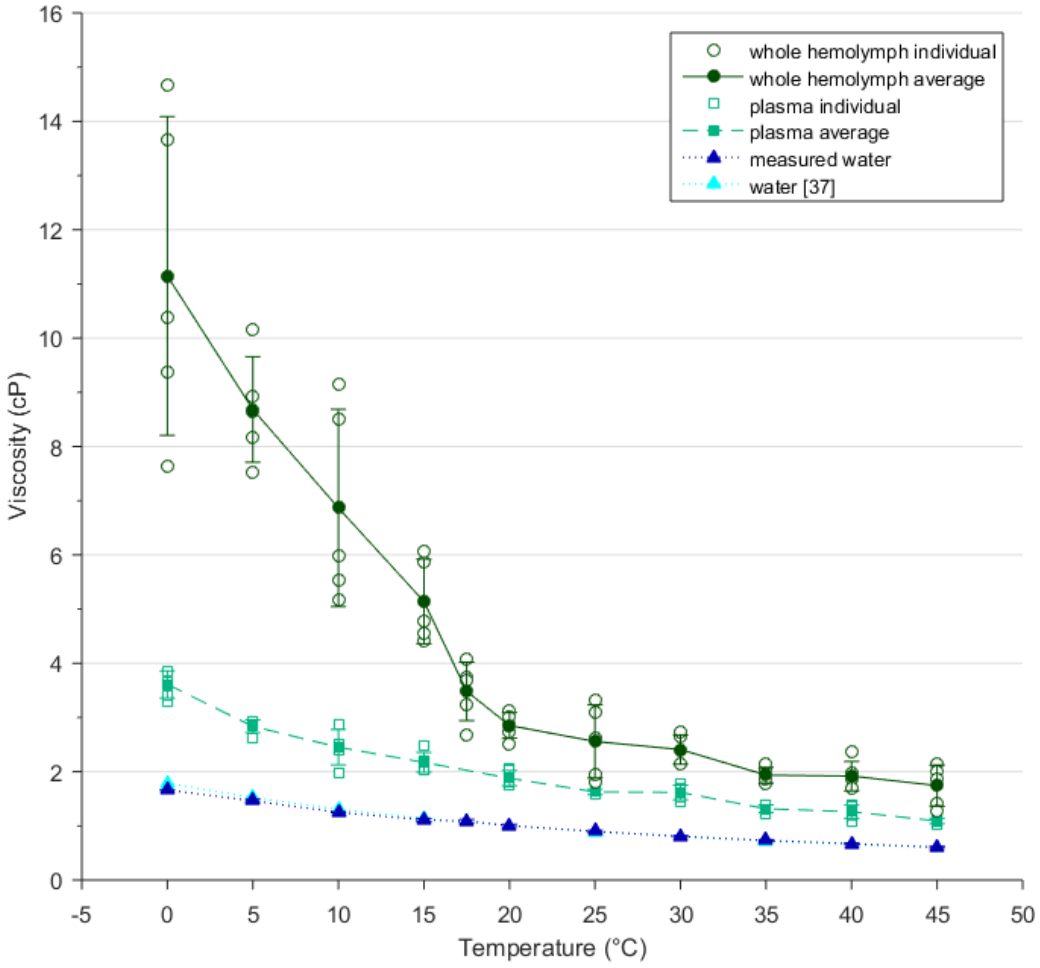

Figure 3.2: Temperature dependence of viscosity for whole hemolymph and plasma of *Manduca sexta* larvae. Known values of water are shown for comparison, from [3]. Filled points represent the average value for each temperature, with the individual trials shown as non-filled points. Error bars represent standard deviation of the average. The quantitative fits for each trend are provided in Eqns 3.1 and 3.2.

3.3.2 Effect of temperature on viscosity of plasma

Similar to whole hemolymph, as temperature decreased from 0 to 45°C, the viscosity of plasma decreased from 3.6 to 1.1 cP (Fig. 3.2, LM: $p < 0.0001$), representing a 3.3x change. The viscosity of plasma was less than the viscosity of whole hemolymph at all temperatures (PT: $p = 0.006$). An exponential model fit to the data (Fig. B.2.2, LM with a logarithmic transform of viscosity, $R^2 = 0.94$) yielded:

$$\mu_p = 3.25e^{-0.0249T}, \quad [3.2].$$

where μ_p is the viscosity of plasma in cP and T is temperature in °C. The viscosity of plasma was also greater than that of water at all temperatures measured (Fig. 3.2, PT: $p < 0.0001$). Temperature did not have

a significant effect on the viscosity relative to water (Fig. 3.3, LM: $p < 0.001$). On average, plasma was 1.92 ± 0.18 (mean ± SD) times the viscosity of water at all temperatures.

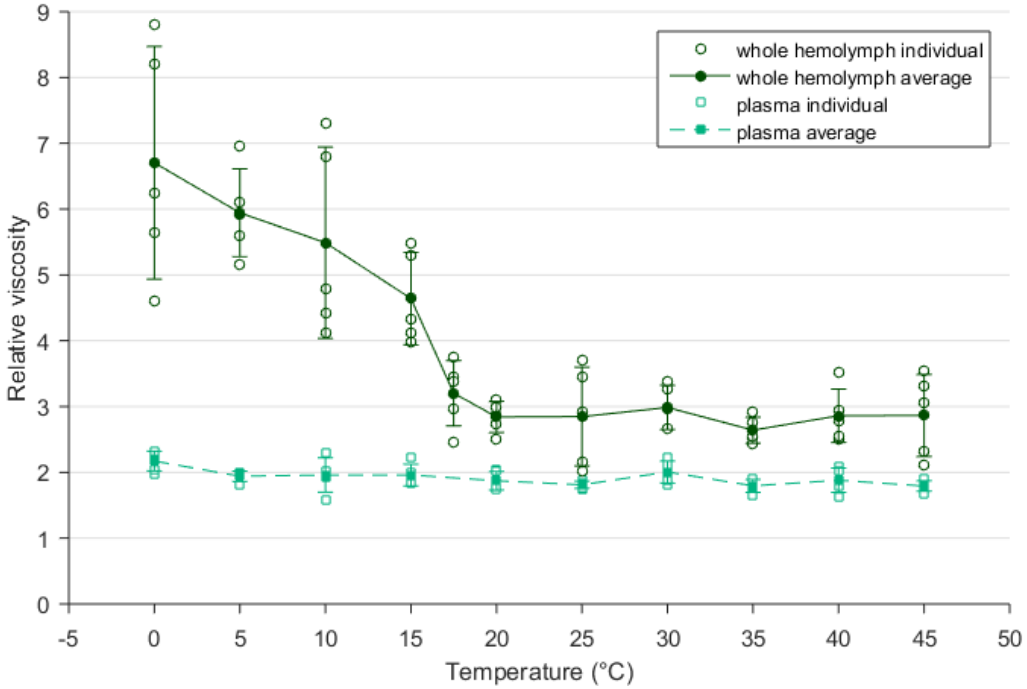

Figure 3.3: Viscosity relative to water versus temperature for both whole hemolymph and plasma in *Manduca sexta* larvae. Filled points represent the average value for each temperature, with the individual trials shown as non-filled points. Error bars represent standard deviation of the average. Relative viscosity of plasma appears to remain consistent with temperature, as does relative viscosity of whole hemolymph temperatures higher than 17.5°C. At low temperatures (<17.5°C), relative viscosity of whole hemolymph increases with decreasing temperature.

3.3.3 Effect of shear rate on viscosity

For both whole hemolymph and plasma, as shear rate increased, viscosity decreased (Fig. 3.4: LMM with ANOVA: $p < 0.0001$ for both). The average change in viscosity over shear rate was -1.9×10^{-3} cP s for whole hemolymph and -7.6×10^{-4} cP s for plasma.

3.3.4 Density of whole hemolymph

The density of whole hemolymph at 22°C was 1.02 ± 0.03 g/mL, which was significantly greater than the density of water at that temperature (0.9977705 g/mL [97]; TT: $p < 0.0001$). Density increased with age (LM: $p = 0.022$) and mass (LM: $p = 0.003$) of the animal (Fig. B.2.4).

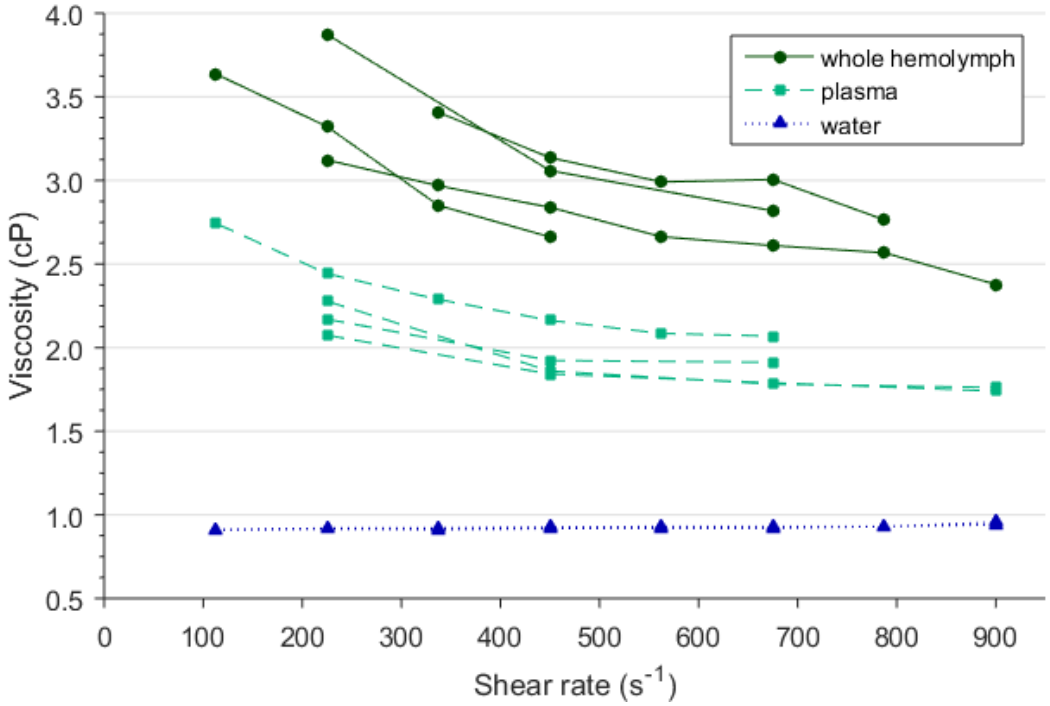

Figure 3.4: Viscosity versus shear rate for whole hemolymph and plasma of *Manduca sexta larvae*. Water, shown for comparison, does not vary with shear rate. Each connected set of points represents a single trial of a single sample, in which shear rate was changed incrementally over time. For some trials, the lowest or highest shear rate measured viscosity values outside of the instrument's range and were unable to be measured (Table B.2.1).

3.3.5 Validation of methods

Viscosity values for water trials for each temperature were within 2.46 ± 1.74% of literature values [3], which was not a significant difference (PT: $p = 0.2$). As expected, viscosity of water did not vary with shear rate. Density values of distilled water yielded an average density of 0.995 ± 0.016 g/mL, which was not significantly different from the literature value at 22°C (0.9977705 g/mL [97]; TT: $p = 0.59$).

3.4 Discussion

In this study, we show that the viscosity of whole hemolymph and plasma of *Manduca sexta* larvae decreases as temperature increases. This general trend has also been observed in the blood of many other species across taxonomic groups, including mammals (humans [82, 98], penguins [29, 98], seals [98], ducks [98], dogs [99], horses [99], and rats [99]), and amphibians (toads [99]), and fish [31]). Hemolymph viscosity changes more rapidly in response to temperatures lower than 15°C, a behavior that is similarly found in human blood [33, 82], which contains far more cells. This low-temperature effect did not occur in plasma, suggesting that the presence of cells or other large particulates are responsible for this behavior. In human blood, decreasing temperature increases the aggregation of red blood cells [100], which increases

blood viscosity [101]. Similarly, the deformability of red blood cells decreases with lower temperature [82, 100], which also increases blood viscosity [14, 82, 100]. Changes in cell deformability with temperature occurs in other animal cell types as well [102, 103], suggesting that this mechanical behavior is a characteristic of the cell's lipid bilayer membrane. Insect hemocytes may respond similarly to decreases in temperature, potentially explaining the steep incline in viscosity at low temperatures observed in the hemolymph of *Manduca sexta* larvae.

The whole hemolymph viscosity values found here, irrespective of temperature, are similar in magnitude to values reported in other animals [29-31, 79, 98, 99]. In most cases, direct comparisons cannot be made, because measurements have been conducted at different shear rates and temperature. When compared to the few viscosity measurements that have been made at the same shear rate (450 s^{-1}) and temperature (30°C), insect hemolymph viscosity (range, 2.1-2.7 cP) is found to be close to both crocodiles (avg, 2.89 cP; [79]) and the western fence lizard (range, 2.7-5.9 cP, with higher values at greater hematocrit; [30]). The differences are likely due to the percentage of cell mass within the blood, which is directly correlated with blood viscosity across species [14, 33]. Hematocrit percent of insect hemolymph is <5% [104], which is considerably less than the 18.7-50.8% measured in crocodiles and the western fence lizard [30, 79]. The removal of cell mass from blood to obtain plasma yields a lower viscosity in many organisms [35], as is also seen here with insect whole hemolymph compared to plasma.

Viscosity of both whole hemolymph and plasma of *Manduca sexta* larvae was also found to be significantly affected by shear rate, showing a decrease in viscosity with increasing shear rate. This behavior indicates that hemolymph acts as a shear-thinning, non-Newtonian fluid, similar to the whole blood of all species in which shear rate has been tested (penguins, chickens, horses, pigs, dogs, cats, rats, cattle, sheep, rabbits, mice, and humans [29, 35, 82]). Human plasma has historically been considered Newtonian [81], but recent evidence suggests it is non-Newtonian [105], a result that we also found with hemolymph plasma. In many animals, blood viscosity is shear-rate dependent only at low shear rates (< 45 s^{-1}) [82]; at high shear rates (> 45 s^{-1}), viscosity is nearly independent of shear rate. Unfortunately, due to experimental limits, we were unable to measure viscosity at a shear rate lower than 112.5 s^{-1} (Table B.2.1), but we can roughly estimate the shear rates that might be experienced within the insect. The insect circulatory system operates at the microscale with very low Reynolds number (ratio of inertial to viscous forces; [78]), with the fastest flows likely occurring in the heart; thus, highest shear rates should be found here. Few exact values are known, but taking the grasshopper heart as an example, maximum shear rate can be estimated. Assuming a maximum velocity of 9.5 mm/s with a 0.5 mm diameter of the heart [21], shear rate can be calculated to be approximately 152 s^{-1} at the inner surface of the dorsal vessel. This estimation assumes Poiseuille flow, in which the shear rate of a fluid flowing in a pipe is equivalent to 8 times the ratio of the linear fluid velocity to the diameter of the pipe [78]. Although no detailed velocity profiles of flow in the heart are available to test for Poiseuille flow, this assumption likely represents a lower bound on shear rate (compared to other possibilities such as plug flow). In addition, the pumping in both the dorsal vessel and accessory pulsatile organs involves time-varying velocities [21], which must result in varying and potentially higher shear rates. This analysis suggests that viscosity of hemolymph, as a non-Newtonian fluid, should change throughout the stroke cycle as well.

Changes in viscosity of hemolymph, due to either temperature or shear rate, may influence any aspect of physiology that depends on circulation. The viscosity of a fluid is a measure of its resistance to deforming motion, essentially, how fast a fluid changes shape. In order to produce a faster shape change or fluid

movement, more force must be applied to the fluid, which requires more mechanical work and thus, the investment of metabolic energy. Similarly, the more viscous the fluid, the more energy is needed to simply maintain the same speed of deformation. If energy investment remains constant, then flow rates must change with temperature. Volume flow rate is inversely proportional to the viscosity of the fluid, assuming laminar flow through a rigid pipe with no entrance or branch point nearby [77]. Our results show a 6.4x increase in hemolymph viscosity as temperature decreases from 45 to 0°C, which would indicate, all else being equal, a 6.4x decrease in volume flow rate of hemolymph within the insect. This decreased flow of hemolymph throughout the insect could retard the circulation of nutrients, removal of metabolic waste, and other necessary functions of the circulatory system. Changes in viscosity might also induce changes in flow patterns as Reynolds number changes, meaning that flow of hemolymph through the smallest structures such as antennae, legs, and various internal organs, including the dorsal vessel and auxiliary pumps, could become particularly limited. In humans, for example, many of the dangerous symptoms of hyperviscosity (increased viscosity) of the blood are due to decreased flow in the smallest capillaries, which experience the smallest Reynolds numbers. This can lead to pre-mortem lividity due to the inability of deoxygenated hemoglobin to flow away from the skin [81], decreased cognitive function due to lowered cerebral blood flow [106], as well as eyesight impairment due to decreased retinal blood flow [81]. However, in contrast to vertebrate species, insects largely decouple gas exchange from circulation—most transport of oxygen occus within the tracheal system, not the hemolymph. Thus, hyperviscosity of hemolymph in insects should produce a smaller or negligible negative effect on the animal's metabolic rate and ability to function than it would in animals with coupled respiratory and circulatory systems. Regardless of these potential effects, the physics of flow dictate that at low temperatures, insects must compensate physiologically to maintain the same circulatory flow; if not, they must experience altered flows of hemolymph throughout the coelem.

In our experiments, hemolymph was extracted at room temperature before its temperature was altered for viscosity measurements, so we did not subject the animals themselves to changing temperatures. Many insects have evolved a variety of mechanisms to respond to and survive temperature extremes and variability that directly affect the hemolymph composition. Upregulation of heat shock proteins facilitates correct protein folding and degradation of non-functional proteins, which could be inhibited due to heat exposure [107]. Expression of heat shock proteins has been observed in several insect species including *Cataglyphis* ants [108] and in adult *Drosophila* flies [109]. In response to cold, insects have generally adopted three main strategies: (1) keep bodily fluids below their normal melting point (freeze avoidance), (2) survive ice formation (freeze tolerance), or (2) depress the melting point of their bodily fluids (cryoprotective dehydration) [110]. Freeze avoidance can involve increased glycerol production, purging of water, and synthesis of antifreeze proteins to lower crystallization temperatures [111, 112]. Freeze tolerance involves specific methods to avoid ice formation within cells. It is possible that such physiological responses may affect hemolymph composition and subsequently, viscosity. In fact, when allowed to acclimate to different temperatures, American bullfrogs do not exhibit changes in blood viscosity with changing temperature [32]. The possibility of such effects in insects suggests a direction for future exploration.

As a first study of viscosity in insect hemolymph, we chose to focus on one species and developmental stage. Insects vary not only in size and morphology across species, but they can vary considerably within species due to life cycle stage, environmental factors, and availability of resources. Variation in hemolymph viscosity across species and developmental stages may arise due to differences in water content, cell properties, and plasma protein concentrations, suggesting a large number of new research questions related

to viscosity. For instance, how does hemolymph viscosity vary in pupae or adults? Has the response of hemolymph viscosity to temperature been influenced by evolutionary pressures? Do insects that experience near-constant temperatures have a different hemolymph viscosity response to temperature than those that experience more varying temperatures? Hemocyte numbers in *M. sexta* change daily throughout the larval stage [113] as the larvae prepare for pupation, which suggests that hemolymph viscosity may change through development as well. Fifth instar *M. sexta* larvae were used in this study for consistency and because of their large volume of hemolymph, which was required for our methods. Measuring the hemolymph viscosity in many other insect species and developmental stages, particularly those with smaller body size and/or hemolymph content, will require different methods. One promising candidate is magnetic rotational spectroscopy, which can measure viscosity in a much smaller volume of liquid [114]; however, this method has not yet been applied successfully to hemolymph.

These findings provide the first quantification of insect hemolymph viscosity and density, as well as measuring the response of viscosity to changes in temperature and shear rate. Understanding these values and relationships helps to reveal potentially important factors for the role of hemolymph in insect physiology.

Acknowledgements

We acknowledge the assistance of Christie Crandall, Katie Johnson, Brittany Horton, Patrick Rogers, and Amanda Barnes. In particular, we would like to thank Binh Nguyen at the University of Washington for supplying hornworm larvae for testing. Also, the Laboratory for Interdisciplinary Statistical Analysis (LISA) at VT was crucial to completion of the statistical analyses. We thank Dr. Mark Stremler for comments on the manuscript and Dr. Rafaella De Vita, Dr. Konstantin Kornev, and Pavel Aprelev for discussion.

Chapter 4

Effects of environmental temperature on viscosity of *Manduca sexta* hemolymph

Manuscript authors: Melissa C. Kenny, Christie L. Crandall, Brent J. Sinclair, and John J. Socha

Citation: Kenny, M.C., Crandall, C.L., Sinclair, B.J., & Socha, J.J. (2019) Effects of environmental temperature on viscosity of *Manduca sexta* hemolymph. *Manuscript in preparation.*

Abstract

Temperature influences many aspects of insect physiology, impacting behavior and survival. Insect hemolymph viscosity is also temperature dependent, showing a 6.4-fold change from 0 to 45°C in *Manduca sexta* larvae. As poikilotherms, insects experience a wide range of internal temperatures, suggesting that their circulatory system must accommodate a broad range of viscosities. Changes in hemolymph viscosity could significantly affect the dynamics of circulatory flows. Insects respond physiologically to acclimation at different temperatures with mechanisms such as release of proteins or fatty acids, thereby affecting hemolymph composition, but it is unclear if they also affect viscosity. Here we ask, does rearing temperature affect the viscosity of insect hemolymph? We measured viscosity of hemolymph from *Manduca sexta* larvae reared in three different temperature regimes: 15:10 (cold), 25:20 (room), and 35:30 (warm) °C, with 14:10 hour day:night cycles. A cone-and-plate viscometer attached to a circulating bath measured viscosity at 5, 15, 25, and 35°C. Cell diameter, volume, viability, and circularity of hemolymph was measured via a Vi-Cell cell counter. Hemolymph viscosity of cold-reared larvae were significantly less than room- and/or warm-reared larvae at 5, 15, and 35°C. In addition, while there are no differences in cell volume between rearing conditions, average cell diameter was significantly higher in cold-reared insects. These data suggest that compositional changes of hemolymph in response to temperature may also affect viscosity in insects.

Keywords: hemolymph, viscosity, temperature, insects, acclimation, hemocyte

4.1 Introduction

As poikilotherms, the body temperature of insects varies with and is a function of the external environment. Thus, most processes which underlie insect physiology and behavior are influenced by temperature [115, 116]. The effect of environmental temperature on many insect behaviors has been characterized. Notably, a decrease in temperature results in a decrease in insect activity [85], which has a similar effect on feeding [85], mating [89, 90], flight [88], and territorial behavior [91]. Temperature also affects insect physiology, with a decrease in temperature resulting in a disruption of ion and water homeostasis [92], decreased muscular activation [117, 118], and increased hemolymph viscosity [4]. However, insects still survive at a large range of temperatures, using a range of potential responses to acclimate to extreme temperatures. These responses affect both behavior and physiology, ultimately affecting performance of the insect. The mechanisms underlying thermal acclimation responses are not completely understood but can include modifications to cytoskeletal structure, cell membrane composition, gene expression, biochemistry, and neuromuscular activity [119, 120]. The effect of temperature acclimation on internal physical properties, such as hemolymph viscosity, remains unstudied.

Circulation of insect hemolymph functions to deliver nutrients, remove metabolic waste, transport signaling proteins, thermoregulate, and provide an immune response for the insect [12, 14, 20]. Hemolymph flow within this system is governed by its geometry and morphology as well as the physical properties of the hemolymph. The morphology of the insect circulatory system is generally understood, with the open system involving a contractile dorsal vessel to generate flow and accessory pulsatile organs to aid in flow through the appendages [6, 15, 16, 20]. The physical properties of hemolymph are not as well studied, but hemolymph density and viscosity have been measured in *Manduca sexta* larvae, showing significant changes in hemolymph viscosity with temperature [4]. Changes in insect hemolymph viscosity could directly influence the energetics required to produce flow throughout the circulatory system. Assuming laminar flow in a rigid pipe, similar to many aspects of the insect circulatory system like the legs, antennae, and heart, we can assume Poseuille's law applies to flow within the insect circulatory system. Thus, an increase in viscosity would result in an increase in resistance to flow which would decrease flow rate [78]. If hemolymph viscosity increased, the insect would either suffer lower flow rates or would require more energetic input from the circulatory muscles to maintain the same flow rate [78]. Changes in hemolymph viscosity could also directly influence patterns of flow within the circulatory system. Reynolds number (ratio of inertial to viscous forces) [78] would vary from 0.4 (viscosity dominated) to 2.9 (inertia dominated) if we assume velocity of hemolymph within and length of the grasshopper heart [21] with hemolymph density and viscosity ranging across temperatures in hornworms [4]. Decreases in flow rate and changes in flow patterns due to changes in viscosity could slow the circulation of necessary nutrients and waste as well as limit flow through the smallest bodily structures such as the antennae and legs. This means that at low temperatures, where insects may experience increased viscosity [4], insects must compensate physiologically to maintain the same circulatory flow.

In response to temperature extremes, insects have developed a range of coordinated and integrated mechanisms that allow them to survive and flourish [6, 115, 116]. These mechanisms allow insects to modify many different aspects of their physiology and biochemistry. In fact, cold acclimation in *Drosophila melanogaster* resulted in extensive genetic changes, including differential regulation of almost one third of the transcriptome and half of the metabolome [121]. Heat acclimation can involve increased metabolic

activity, upregulation of heat shock proteins, and hormonal changes [107, 122]. Cold acclimation can include increased glycerol production, synthesizing antifreeze proteins [112], or purging water [111]. Thermal acclimation mechanisms allow insects to maintain high levels of performance at temperatures that would otherwise elicit a decline in performance. At cold temperatures, insect hemolymph becomes more viscous [4], and assuming the morphology of the circulatory system remains the same, this would result in reduced performance or increased energy input. Cold acclimation may provide relief from hemolymph viscosity changes to maintain performance. In fact, when allowed to acclimate to different temperatures, American bullfrogs do not exhibit changes in blood viscosity with changing temperature [32]. However, cold acclimation in insects often includes the accumulation of cryoprotectants, which tend to increase viscosity and would exacerbate increased hemolymph viscosity at lower temperatures. Other changes in hemolymph composition could potentially decrease viscosity, including changes in hemocyte concentration and properties [14, 82], as well as varying lipid and protein concentrations [31, 123] and plasma osmolality [124]. In fact, insect hemolymph viscosity, particularly at low temperatures, is significantly increased by the presence of hemocytes [4] and hemocyte concentration can vary due to availability of blood, nutritional status, seasonal variation, and immune response [125-127]. Since increased hemolymph viscosity at low temperatures could adversely affect hemolymph flow, temperature-mediated changes in viscosity could be advantageous.

We predict that hemolymph from insects reared at colder temperatures will have lower viscosity at low temperatures than insects reared at room or warm temperatures to maintain hemolymph flow. Here, we measured the viscosity of insect hemolymph from *Manduca sexta* larvae reared at three different temperatures regimes across a range of temperatures spanning from 5 to 35°C. We also measured concentration and properties of hemocytes to identify any changes due to insect rearing temperature. In addition, we measured physiological response to changes in environmental temperature by measuring heart rate and response to a stimulus, both of which are directly linked to hemolymph flow. Considering the importance of circulatory flow, modulation of hemolymph viscosity via temperature-mediated mechanisms may allow insects to maintain similar hemolymph flow across temperatures.

4.2 Methods

4.2.1 Animals

Manduca sexta larvae were obtained from Great Lakes Hornworms (Romeo, Michigan), shipped to Virginia Tech via 2-day shipping. The physiology of the larvae of this species has been extensively studied [6], including a previous study of hemolymph viscosity [4]. In particular, this species yields sufficient hemolymph for testing (about 700 µL per animal). Additionally, *Manduca sexta* have well known thermal acclimation mechanisms [128, 129].

Larvae were reared individually within three separate incubators (Model 10, Percival Mfg. Co., Boone, Iowa) with temperature controllers (Watlow Series 1500 Controllers, Watlow Controls, Inc., Winona, MN) set at different temperature regimes: 15:10 (cold), 25:20 (room), and 35:30 (warm) °C, with 14:10 hour day:night cycles (Figure 4.1a). They were given access to food *ad libitum* (Hornworm Food, Great Lakes

Hornworms, Romeo, Michigan) until they were at least 6 g in mass and had reached the fifth instar of their developmental cycles. We chose to use fluctuating temperatures for our acclimation regimes because they yield stronger phenotypic responses than constant temperatures in most insects [130].

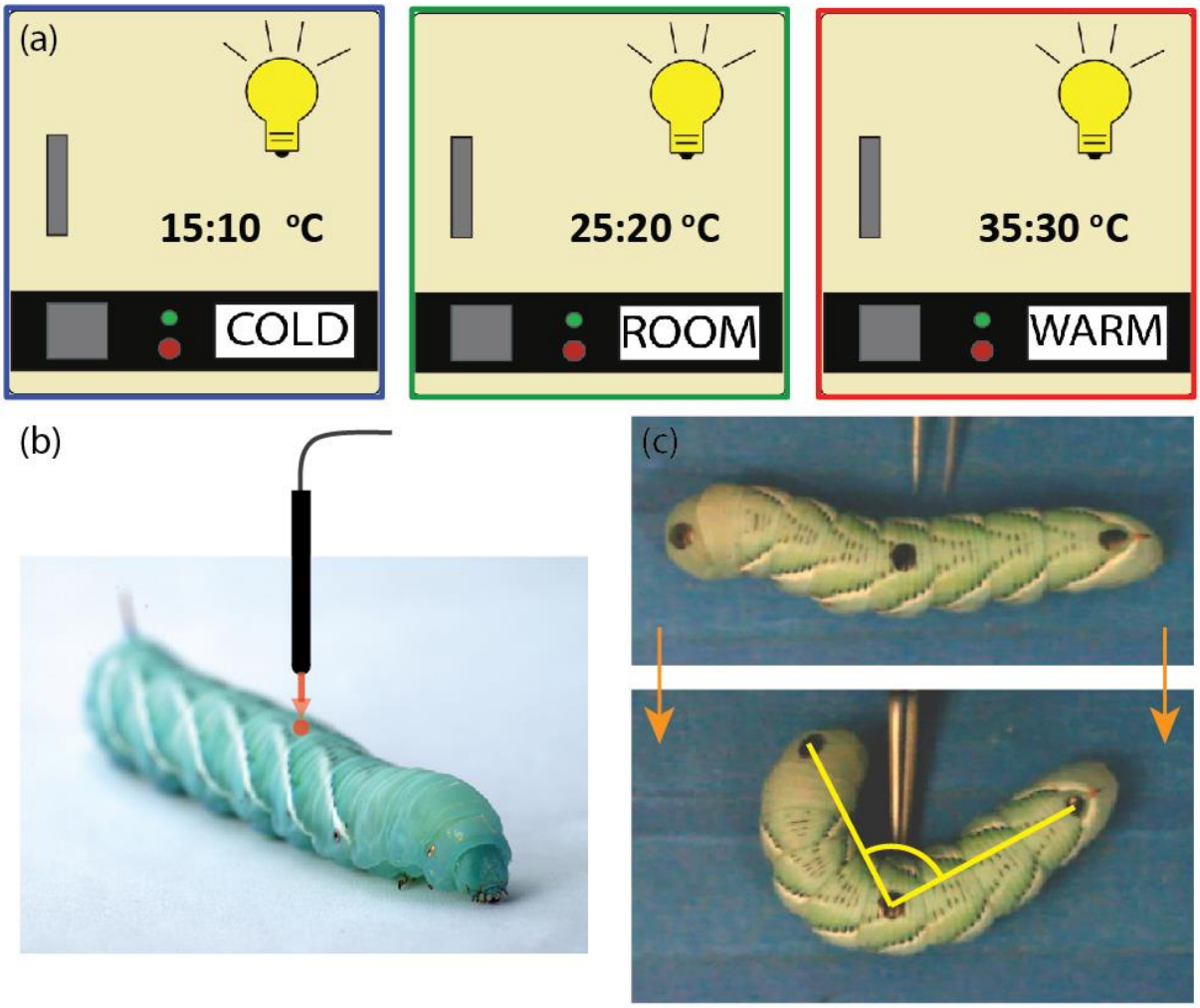

Figure 4.1: Diagram of incubator set up (a), showing cold (15:10°C), room (25:20°C), and warm (35:30°C) rearing conditions. Diagram of infrared sensor set up (b), showing an IR sensor aimed at the mid-dorsal surface of a *Manduca sexta* larva. Striking response of a larva (c), from relaxed pose (top) to full strike (bottom) with three marks shown on the dorsal surface of the larva and the angle of strike (yellow) indicated.

4.2.2 Viscosity and cell measurements

Viscosity measurements were conducted with a cone-and-plate viscometer (DV-II+ Pro, Brookfield Engineering, Massachusetts, USA) with an attached chiller/heater circulator (RE 206, Lauda, Germany) as described previously [4]. Because hemolymph clots quickly, measurements were made within a sealed environmental chamber (CleaTech Critical Laboratory Supplies, California, USA) flooded with dry nitrogen gas. Viscosity measurements were obtained at 5, 15, 25, and 35 °C at shear rates between 450-460 s^{-1}. Hemolymph was extracted via an incision between the 2nd and 3rd set of prolegs of the larvae, following protocol developed by Kenny et al. [4]. A single representative viscosity value was identified for each trial

using a moving window standard deviation to determine when the raw instantaneous viscosity value was steady over time, following protocol described by Kenny at al. [4]. For each temperature, we recorded data from ten hemolymph samples per rearing temperature, with one sample per individual. Trials that did not reach a steady viscosity value after 20 minutes were not included. In total, 156 viscosity trials were performed, with 120 trials yielding useable values.

For each hemolymph sample measured, we created a 1 mL sample of 9:1 dilution of hemolymph with an anticoagulant (98 mM NaOH, 186 mM NaCl, 1.7 mM EDTA, 41 mM citric acid, pH 6.8 [5]). Concentration, viability, average diameter, and average circularity of hemocytes were measured via a cell counting machine which uses the trypan-blue exclusion method, wherein dead cells uptake trypan-blue, to count number of viable and dead cells in each sample (Vi-Cell Cell Counter, Beckman Coulter, USA)[131]. For each cell, the area and perimeter were measured directly, and the diameter could be approximated from each of these assuming a circular shape. Cell circularity was calculated as the ratio of the diameter calculated from the area measurement to the diameter calculated from the perimeter measurement, which would be 1 for a circular cell.

4.2.3 Heart rate and striking response measurements

At 6 g, larvae were exposed to 5, 15, 25, and 35°C for 1 h before measuring heart rate and response to a stimulus. For each exposure temperature, we recorded data from ten samples per rearing temperature, with both heart rate and response to stimulus measured for each animal. Measurements were recorded with the insect placed on a temperature-controlled plate (CP-200HT, TE Technology, Inc., Traverse City, Michigan) using a standalone temperature controller (PELT-5 Temperature Controller, Sable Systems International, North Las Vegas, NV) to maintain the exposure temperature for the duration of the trial.

Heart rate was measured with an infrared (IR) sensor (FD-T80 Diffuse Reflective Fiber Optic Cable, Sunx Sensors, West Des Moines, Iowa) connected to an amplifier (FX-11A Slim Body Analog Fiber Sensor, Sunx Sensors, West Des Moines, Iowa) with readings collected digitally using a custom Arduino circuit (Arduino UNO, arduino.org) and Python script. The IR sensor was aimed at the midline of the dorsal surface directly over the dorsal vessel of the larvae (Figure 4.1b). The IR sensor detects small changes in distance between the dorsal vessel and the sensor, created by the heartbeat or movement of the abdominal surface. Measurements were collected at the highest sampling rate the circuit and computer were capable of, which resulting in varying sampling rate throughout each trial. Sampling rate was approximately 1818 to 2955 Hz for each 1-2 min trial. Movement of the larvae during measurement resulted in significant changes in the IR signal intensity, obscuring the heart rate signal, so sections between movements were identified for analysis, ranging from 7.3 to 106.5 s in length. Each data section was smoothed in MATLAB using a moving average filter before the local maxima were identified using a built-in function. Heart rate for each sample was calculated as the total number of local maxima divided by the total time.

Response to a stimulus was measured by using tweezers to pinch the larvae on its second, right proleg to elicit a characteristic striking response that involves the insect bending laterally while opening the mandibles to strike [132]. Insects were recorded from above at 30 fps and three marks were made on the dorsal surface of the animal using a black marker (Sharpie, California, US): on the thorax, above the pinched proleg, and directly in front of the posterior horn. The location of these marks throughout the strike were

tracked automatically using Tracker software (physlets.org). A line was created between the marks on the thorax and above the proleg as well as those above the proleg and posterior end, creating an angle that represents the bend in the animal throughout its strike (Figure 4.1c). This angle was measured over time, and the change in this angle between time points represents the angular velocity of the strike. We calculated the maximum angular velocity using a running 4-point linear regression of the angle measurements over time, which represents the maximum striking reaction of each larvae.

4.2.4 Statistical analysis

R (Foundation for Open Access Statistics) was used for all statistical analyses. A linear model (LM) was used to test for the effect of one variable upon another. Analysis of variance (ANOVA) was used to compare values to determine any differences. To transform non-normal dependent variables to normal when necessary, a Box Cox transformation was used. To determine which means differed in a multiple comparison ANOVA, post-hoc analysis was done using Tukey's HSD.

4.3 Results

4.3.1 Viscosity

Hemolymph viscosity for each rearing temperature measured at the same temperature were similar. Average hemolymph viscosity was 3.5 ± 0.8 cP (mean ± S.D.) for cold-reared at 15°C, 2.7 ± 0.9 cP for room-reared at 25°C, and 3.1 ± 0.9 cP for warm-reared at 35°C (Figure 4.2). As the temperature increased from 5 to 35°C, the average hemolymph viscosity for room-reared larvae decreased from 10.1 to 2.6 cP, representing a four-fold change across this temperature. Average hemolymph viscosity for warm-reared larvae decreased from 8.7 to 3.1 cP across the same temperature range, a 2.8x change. The hemolymph viscosity of warm-reared larvae were not significantly different from that of room-reared larvae at each temperature measured (ANOVA with Tukey's HSD: $p>0.97$; Table 4.1; Figure 4.2).

Average hemolymph viscosity for cold-reared larvae decreased from 5.1 to 1.9 cP as temperature increased from 5 to 35°C, representing a 2.7x change. At 5°C, hemolymph viscosity of cold-reared larvae was significantly lower than that of both room- and warm-reared larvae (ANOVA with Tukey's HSD: $p<0.04$; Table 4.1). Hemolymph viscosity of cold-reared larvae was significantly lower than that of room-reared larvae at 15°C (ANOVA with Tukey's HSD: $p<0.008$; Table 4.1) and of warm-reared larvae at 35°C (ANOVA with Tukey's HSD: $p<0.0003$; Table 4.1). At 25°C, hemolymph viscosity was similar across all three rearing regimes (Figure 4.2).

Table 4.1: Summary of ANOVA comparing hemolymph viscosity for rearing temperature, measurement temperature, and interaction of the two.

Source	df	MS	*F*	*P*
Rearing temperature	2	0.5909	24.188	<0.0001
Measurement temperature	3	2.6844	109.878	<0.0001
Rearing × Measurement temperature	6	0.0994	4.069	0.00102
Residuals	108	0.0244		

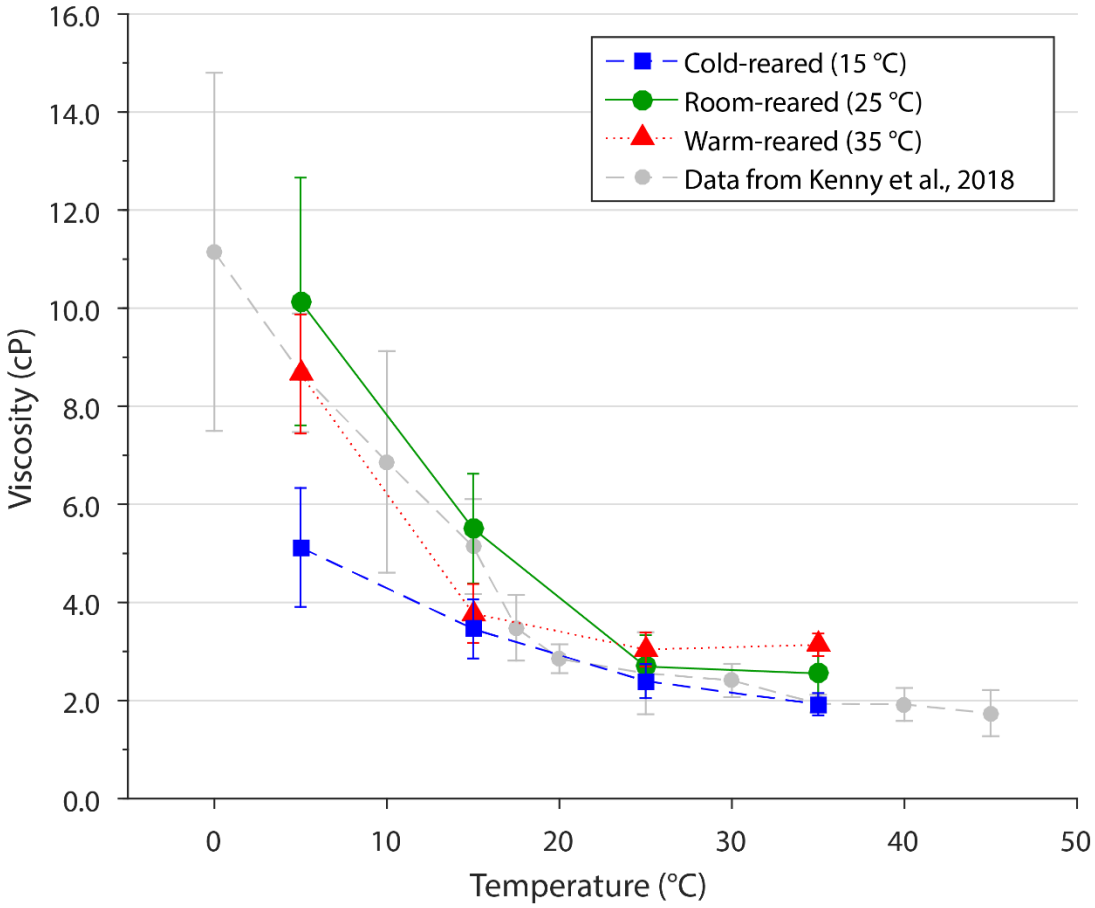

Figure 4.2: Temperature dependence of hemolymph viscosity from cold-, room-, and warm-reared *Manduca sexta* larvae. Previous hemolymph viscosity values from [4] shown for comparison. Filled points represent the average value for each temperature and rearing condition, with error bars representing 95% confidence intervals for the mean.

4.3.2 Hemocytes

Hemocyte volume was similar across larvae from all three rearing regimes, with 0.71 ± 0.28 x 10^6 cells/mL (Table 4.2; Figure 4.3a). Across all larvae tested, 808 ± 324 hemocytes were found in each hemolymph sample with a total of 96,934 hemocytes tested for viability, circularity, and diameter. The viability and circularity of hemocytes were similar for both cold- and room-reared larvae (ANOVA with Tukey's HSD: $p>0.75$; Figure 4.3b and 4.3c). Hemocytes of cold-reared larvae were 85 ± 7% viable and had a circularity ratio of 0.86 ± 0.01. Hemocytes of room-reared larvae were 84 ± 8% viable and had a circularity ratio of 0.86 ± 0.02. Hemocytes of warm-reared larvae were significantly less viable and less circular than those of other rearing regimes, with 79 ± 6% viability (ANOVA with Tukey's HSD: $p<0.001$) and a circularity ratio of 0.85 ± 0.02 (ANOVA with Tukey's HSD: $p<0.005$). The diameter of hemocytes was similar for room- and warm-reared larvae (ANOVA with Tukey's HSD: $p=0.22$), measuring an average diameter of 10.1 ± 0.4 µm and 9.9 ± 0.5 µm, respectively. Hemocyte diameter for cold-reared larvae was significantly larger than that of other rearing regimes (ANOVA with Tukey's HSD: $p<0.0001$), with an average diameter of 11.2 ± 0.7 µm (Figure 4.3d).

Table 4.2: Summary of ANOVA comparing cell volume, viability, circularity, and diameter for rearing temperature.

Cell property	Source	df	MS	*F*	*P*
Volume	Rearing temperature	2	0.2678	2.017	0.138
	Residuals	117	0.1327		
Viability	Rearing temperature	2	$2.478 \cdot 10^{20}$	11.38	<0.0001
	Residuals	117	$2.177 \cdot 10^{20}$		
Circularity	Rearing temperature	2	0.010589	68.26	<0.0001
	Residuals	117	0.000155		
Diameter	Rearing temperature	2	0.010589	68.26	<0.0001
	Residuals	117	0.000155		

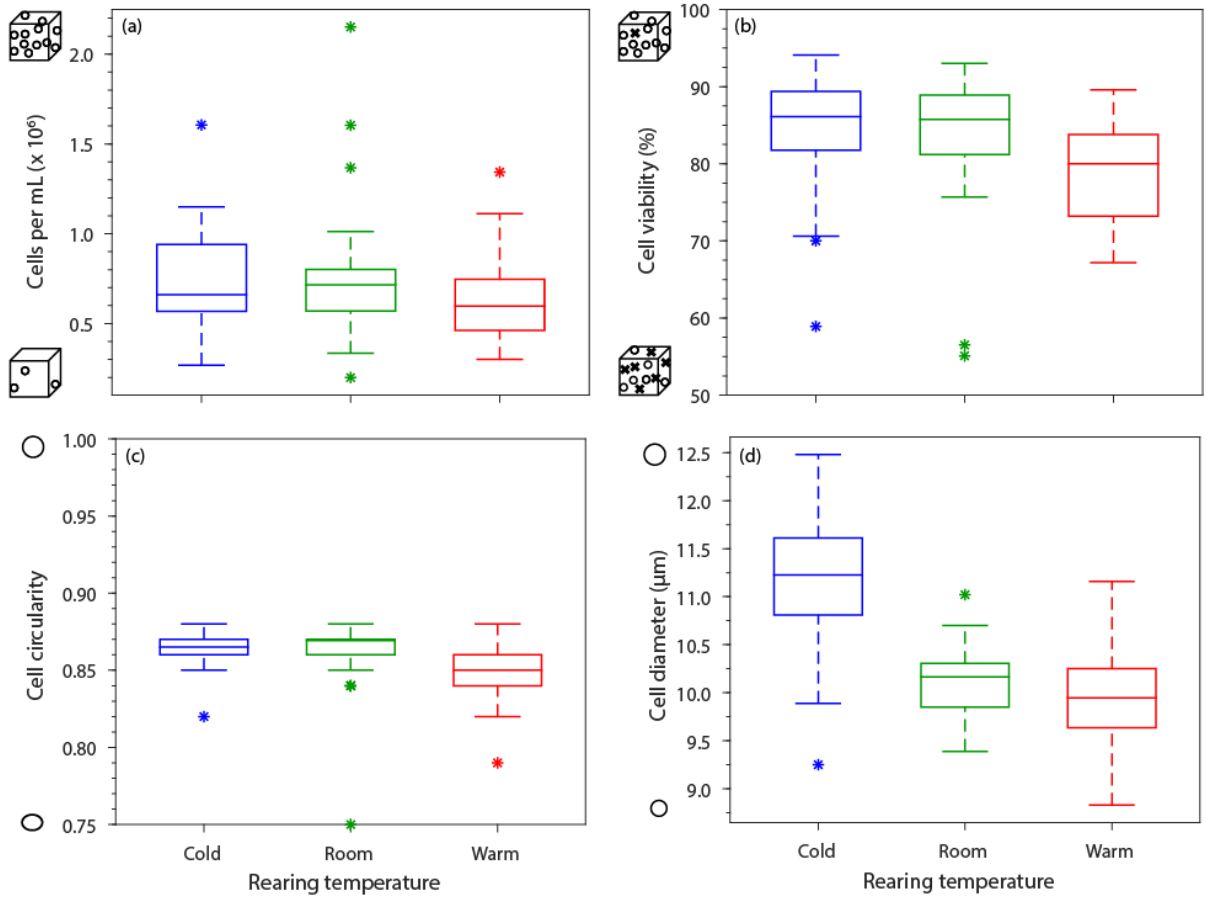

Figure 4.3: Hemocyte properties, including volume (a), viability (b), circularity (c), and diameter (d) from cold-, room-, and warm-reared *Manduca sexta* larvae. Box-and-whisker plots show median, quartiles, and outliers for each rearing condition.

4.3.3 Heart rate

Heart rates ranged from 3.4 to 74.0 bpm across the 120 larvae tested. Exposure temperature had a significant effect on heart rate (LM: $F = 1209$, $df = 118$, $p<0.0001$), with an increase in heart rate from an average of 16.1 to 60.7 bpm as exposure temperature increased from 5 to 35°C. Assuming a linear relationship between heart rate and temperature, similar to other insects across this temperature range [133], heart rate increased by approximately 1.5 bpm per 1°C increase in exposure temperature. Rearing temperature did not affect heart rate at exposure temperatures of 5, 15, or 25°C (ANOVA with Tukey HSD: $p>0.29$; Table 4.3). At 35°C exposure temperature, heart rate of room-reared larvae was significantly higher, with an average of 65.8 ± 4.6 bpm, than that of both cold- (57.8 ± 2.2 bpm) and warm-reared (58.4 ± 8.5 bpm) larvae (ANOVA with Tukey HSD: $p<0.04$; Figure 4.4a).

Table 4.3: Summary of ANOVA comparing heart rate for rearing temperature, exposure temperature, and interaction of the two.

Source	df	MS	*F*	*P*
Rearing temperature	2	126	4.082	0.0195
Exposure temperature	3	23490	506.545	<0.0001
Rearing × Exposure temperature	6	250	2.699	0.0176
Residuals	108	1669		

4.3.4 Striking response

Maximum angular speed during striking response of each larvae ranged from 1.4 to 1,381.6 degrees/s across the 120 larvae tested. Exposure temperature had a significant effect on maximum angular speed (LM: $F = 209.6$, $df = 118$, $p<0.0001$), showing an increase in maximum angular speed from an average of 24 to 776 degrees/s as exposure temperature increased from 5 to 35°C. Rearing temperature did not affect maximum angular speed at each exposure temperature (ANOVA with Tukey HSD: $p>0.1$; Table 4.4; Figure 4.4b).

Table 4.4: Summary of ANOVA comparing striking response for rearing temperature, exposure temperature, and interaction of the two.

Source	df	MS	*F*	*P*
Rearing temperature	2	384	6.037	0.00327
Exposure temperature	3	12050	126.280	<0.0001
Rearing × Exposure temperature	6	237	1.240	0.29171
Residuals	108	3435		

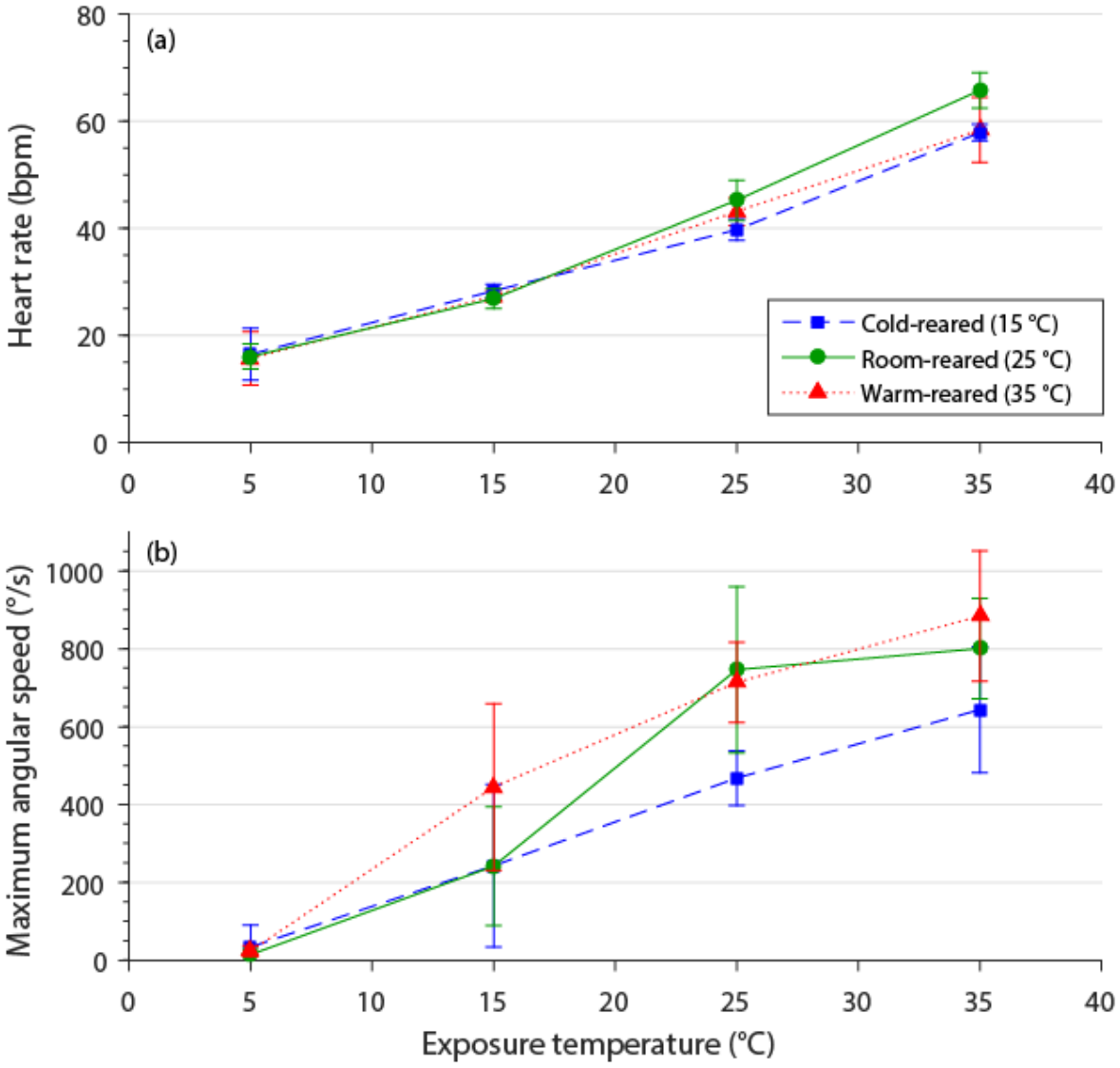

Figure 4.4: Temperature dependence of heart rate (a) and strike response measured as maximum angular speed (b) for cold-, room-, and warm-reared *Manduca sexta* larvae. Filled points represent the average value for each temperature and rearing condition, with error bars representing 95% confidence intervals for the mean.

4.4 Discussion

In this study, we show that cold-reared *Manduca sexta* larvae modulate their hemolymph viscosity in some way to lower viscosity particularly at low temperatures. Since increased hemolymph viscosity at low temperatures could adversely affect hemolymph flow, temperature-mediated changes in viscosity such as those measured here would be advantageous. Assuming Poseuille flow in the circulatory system, the power input to produce flow of hemolymph is directly proportional to hemolymph viscosity [78]. At colder temperatures, we find a 1.6 to 2 fold decrease in hemolymph viscosity for cold-reared insects compared to room- and warm-reared insects. This decrease would result in the same decrease in power input to produce

the same flow of hemolymph through the circulatory system. Considering that metabolism and activity are known to decrease as temperature decreases in insects [6, 85, 86], a decrease in power to circulate hemolymph would be profitable to the insect for conservation of energy at low temperatures. However, the difference in hemolymph viscosity seen here between different thermally acclimated insects did not manifest in performance measurements. Heart rate and striking response of the larvae at different temperatures remained unaffected by rearing temperature, despite differences in hemolymph viscosity. Additionally, although lower hemolymph viscosity in cold-reared insects represents a new method of cold acclimation, the mechanism underlying this change is still in question.

We did not find any changes in hemocyte concentration across different rearing temperatures, despite hemolymph viscosity being strongly influenced by the presence of hemocytes [4]. Considering that insects are known to vary hemocyte concentration due to nutrition, seasons, and immune stimuli [125-127], we might expect insects to modulate hemocyte numbers to maintain hemolymph viscosity. However, hemocytes play an important role in insect immune response, which may outweigh regulation of hemolymph viscosity, particularly with changes in temperature. Although there were no changes in number of hemocytes across rearing temperature, several hemocyte properties were affected by thermal acclimation. Warm-reared insects had fewer viable cells, likely due to heat damage [134, 135], than room-reared insects but this did not affect hemolymph viscosity in comparison. Cold-reared insects had significantly larger cells, likely due to an influx of water into the cell, causing it to swell. Swelling is a common response of tissue cells to hypothermia [136, 137] and occurs due to impaired function of the membrane-bound ion pumps, causing intracellular hyperosmolarity which leads to water uptake and swelling [138, 139]. At low shear rates (0.5-100 s^{-1}), larger blood cells in mammalian blood have been shown to decrease blood viscosity [140, 141], which may account for the decreased hemolymph viscosity measured here from cold-reared insects.

It is also possible that changes in the hemolymph plasma composition may account for lower hemolymph viscosity in cold-reared insects. Hemolymph plasma is composed of water, inorganic salts, amino acids, and organic compounds such as proteins and lipids [6]. Hemolymph proteins play an important role in the cold tolerance of insects, including both thermal hysteresis proteins and ice nucleator proteins [6, 112, 119, 142, 143]. Concentrations of several other hemolymph solutes also increase at cold temperatures, including glycerol and glucose [112, 143, 144]. However, increases in protein and other solute concentrations in blood plasma increases blood viscosity in both mammals [123, 145] and fish [31]. This would not explain the decrease in hemolymph viscosity seen for cold-reared insects. In contrast, plasma osmolality decreases with decreasing temperature in insects [124], which has been shown to decrease blood viscosity in humans [146]. Measurements of plasma composition and osmolality in insects reared at different temperature regimes represents a future area of study that might further explain the differences in hemolymph viscosity seen here.

While rearing temperature did not affect heart rate in these larvae, exposure temperature did have a significant effect on heart rate. Increasing heart rate with increasing temperature has been observed in several insect species [133, 147-149]. Here, we found a 7.5 bpm increase in heart rate for every 5°C increase in temperature, which is comparable to the 11.1 to 23.8 bpm increase found in the cockroach *Periplaneta americana* over the same change in temperature considering differences in resting heart rate [133]. Heart rate did not vary with rearing temperature except for room-reared larvae at 35°C, which could be due to

heat damage, especially for warm-reared larvae, which would affect heart function [133, 147]. Despite differences in hemolymph viscosity for cold-reared insects to warm- and room- reared insects at low temperatures, this did not manifest in heart rate measurements despite the effect of hemolymph viscosity on flow through the heart. Besides hemolymph viscosity, there are many other factors that affect heart rate that may account for the lack of variation with rearing temperature. Heart rhythmicity and directionality are modulated by neuropeptides and neurotransmitters [150] which can acclimate based on temperature to preserve functionality [151]. Additionally, heart rate is only a single measure of heart function and may not be the only factor in determining hemolymph flow through the heart. Future studies should measure the precise kinematics of the heart wall, including heart contraction pattern or amplitude, in response to temperature acclimation and changes in hemolymph viscosity.

Similarly, maximum striking response was not affected by rearing temperature, but did increase with increasing exposure temperature. This direct relationship between exposure temperature and striking response is expected, knowing that muscle actuation is directly related to temperature in insects [117, 118]. However, considering that these larvae also use hydraulic mechanisms to move that potentially rely on hemolymph viscosity [152, 153], we would expect changes in viscosity in cold-reared larvae to manifest in this striking response as well. However, similar to heart rate, movement also significantly involves muscular actuation which occurs via neural action and does acclimate to temperature [151] and may preserve striking response across rearing temperatures. While differences in hemolymph viscosity do not manifest in striking response, other behaviors which rely nearly exclusively on hemolymph movement may show significant differences. In *Manduca sexta* larvae in particular, it is generally considered that extension of the prolegs occurs predominantly through hydraulic mechanisms, however, there is some evidence of neuromuscular actuation [154]. In several coleopteran, unfolding of the hind wings has been shown to occur solely via hydraulic mechanisms involving microfluidic control of hemolymph in the wing veins [155, 156]. We would expect changes in hemolymph viscosity to significantly affect wing unfolding, especially considering the small size of the wing veins, where viscosity plays a bigger role [78].

These findings provide the first measure of the effect of temperature acclimation on insect hemolymph viscosity. We found that cold-reared insects had lower hemolymph viscosity at low temperatures than room- and warm-reared insects. Although the specific mechanism for this difference in hemolymph viscosity is still not understood, we did also find differences in hemocyte properties. These differences included larger hemocyte diameter in cold-reared insects and less viable, less circular hemocytes in warm-reared insects. Insect cold tolerance and hardiness is of particular interest since, as poikilotherms, insects survive a wide range of environmental and body temperatures. Understanding the effect of cold-acclimation on insect hemolymph viscosity represents another step towards understanding insect cold tolerance.

Acknowledgements

We acknowledge the assistance of Talia Weiss, Dr. Mark Stremler, and Joel Garrett. In particular we would like to thank Dr. Dan Sweeney for Arduino and code assistance, as well as Dr. Scott Verbridge and Dr. Megan Cox for help with and use of their Vi-Cell Cell Counter. We also thank Dr. Joel McGlothlin for use of his incubators. Also, the Statistical Applications and Innovations Group (SAIG) at Virginia Tech was crucial to the completion of the statistical analyses. Partially funded by NSF 1558052 and 0966125.

Chapter 5

Morphological and kinematic characteristics of the heart of the beetle *Zophobas morio*

Abstract

The dorsal vessel is a long, narrow tube along the dorsal midline that acts as the primary pumping organ of the insect circulatory system. Posteriorly, the dorsal vessel consists of a muscularized heart which contracts using a peristaltic motion of the heart wall. This motion can produce flows in two directions in some species. However, the mechanics of how the heart pumps, and thus generates hemolymph flow, are not well understood, particularly in beetles. Here, we measured the morphological characteristics and heart wall kinematics during peristalsis in the beetle *Zophobas morio*. Geometric characteristics of the dorsal vessel were quantified using dissection and thin sectioning, finding an average length of 10.9 mm and cross-sectional area of 0.0182 mm^2, although this varied along the length. Kinematic characteristics of heart contraction were found using infrared sensors and ultrasound imaging, finding a wave contraction speed of approximately 18 mm/s with tube occlusion ranging from 100% to 65.4%. This study presents the first measurement of both morphological and kinematic characteristics of the heart in a beetle in order to expand our knowledge of circulatory system structure and function.

Keywords: insects, dorsal vessel, heart, peristalsis, morphology, kinematics

5.1 Introduction

Insects have an open circulatory system, in which the movement of hemolymph functions to transport nutrients, remove waste, thermoregulate, and provide an immune response [6, 12, 14, 19]. The primary contractile organ of the circulatory system is the dorsal vessel (DV), which is a long, hollow tube along the dorsal midline. The DV is divided functionally into two major regions: the thoracic aorta and the abdominal heart. The aorta is a simple tube that acts as a conduit for hemolymph that is actively propelled by the heart [6, 19]. The heart is separated into chambers, each containing a pair of ostia, which are slit-like openings on each side of the heart that allow hemolymph to enter [6] and vary in morphology across species [157]. The basic ultrastructure of the DV wall includes a cylinder of muscle fibers between two sheaths of connective tissue, with thickness, length, and diameter of the heart varying with species [6, 17-20]. Insect heart morphology has only been studied in detail in a few species, including *Drosophila* [158], *Anopheles gambiae* [19], and *Rhodnius prolixus* [18], however, few have examined it in beetles [16].

Muscular actuation of the insect heart to generate flow has also been studied, showing variation among insect species. In general, the heart consists of two major muscle groups: spirally arranged muscle fibers and ventrally attached longitudinal fibers (termed alary muscles). These muscles function for contraction and dilation of the heart, respectively, although the actual contribution of the alary muscles has been questioned [6, 18, 19]. Hemolymph propulsion by the heart is accomplished by a wave of depolarization originating at one end of the heart and moving through each chamber anteriorly. When depolarization begins at the posterior end, the striated, spiral muscle fibers contract, reducing the volume of the heart and pushing hemolymph anteriorly [159]. As the depolarization wave moves down the length of the heart, it continues to cause the heart to contract and propels hemolymph anteriorly in a bolus-like fashion [20, 159]. This transition of systole (contraction) and diastole (relaxation) down the heart chambers creates a wave-like contraction pattern of the heart wall that has been described as peristaltic [19, 20]. Heart contraction can be bidirectional, propelling hemolymph either towards the head (anterograde) or toward the posterior (retrograde) where it empties into the hemocoel [2, 19]. Depending on the insect species and developmental stage, anterograde propulsion generally dominates heart contraction, with periodic reversals for retrograde flow [150, 160]. In addition, the flow rates of hemolymph within the DV have been visualized and estimated in *Galleria mellonella* [22], *Anopheles gambiae* [19], and *Schistocerca americana* [21]. However, despite preliminary studies of the morphology, muscular action, and hemolymph flow in the insect heart, the precise kinematics of the heart wall are not known.

Circulation of hemolymph through the open insect coelem performs vital functions such as nutrient delivery, waste removal, immune response, and thermoregulation [6, 20]. Hemolymph flow produced by the DV is governed by the physical properties of the hemolymph, as well as the DV morphology and kinematics. The properties of the peristaltic wave of contraction down the length of the heart will determine volume flow rate of hemolymph. Specifically, numerical simulations of peristaltic tubular pumps have found that fluid flow is dependent on contraction frequency, contraction wave speed, and tube occlusion [161]. Flow speeds within peristaltic tubular pumps can be pulsatile and can exceed the speed of compression of the wave, particularly at or above 60% occlusion of the tube [161]. Additionally, with single contraction waves, as is seen in many insect hearts [19], numerical models show retrograde fluid flow within the tube throughout peristalsis due to negative pressures [162]. Considering the diversity of insect species, contraction wave speed and tube occlusion likely vary across insect species and developmental

stages. Contraction speed down the length of the heart has been measured as 14 mm/s in *Tenebrio molitor* [159]. Tube occlusion is also known to vary with flow direction in *Anopheles gambiae*, where anterograde contractions did not involve complete occlusion of the heart, but retrograde contractions were more forceful with complete constriction [19]. A full understanding of the heart wall movement and kinematics during heart pumping is unknown in any insect species, which is crucial to understanding hemolymph flow within the DV and potentially the entire coelem.

In this study, we measured the morphology and kinematics of the heart in *Zophobas morio* adults. Specifically, we used dissection and thin sectioning to measure the length, cross-sectional area, and other morphological characteristics of the heart of this beetle. We also used infrared sensors and ultrasound imaging to measure speed of contraction of the heart and the cross-sectional area of the heart throughout contraction and dilation. Understanding how the insect heart wall moves will help us understand how it produces flow and ultimately, the full structure and function of the DV and the circulatory system in this insect. This will be extremely valuable in advancing our knowledge of the insect circulatory system.

5.2 Methods

5.2.1 Animals

Zophobas morio adults were obtained from a lab-grown colony from the Socha Lab at Virginia Tech originating from larvae obtained from Carolina Biological Company (Burlington, North Carolina). Beetles were offered bran meal (Carolina Biological, Burlington, North Carolina) and water *ad libitum*. This species was used because while previous studies have examined the dorsal vessel in several species, including *Rhodnius prolixus* [18] and *Anopheles gambiae* [19], few have examined it in beetles [16]. We are also studying the interaction of circulation and respiration in this species in the lab. Considering that insects make up 61-71% of described eukaryotic species and beetles make up roughly 40% of insects [163], this is a significant gap in our understanding.

5.2.2 Dissection

Beetles were sacrificed with fumes of ethyl acetate, weighed on a digital scale (ALT04, Mettler Toledo, Columbus, Ohio), and photos of the intact beetle were obtained (Nikon D90, Nikon, USA). Elytra, wings, and legs were removed from the beetle using dissecting scissors. A longitudinal cut was then made along the midline of the ventral surface using a scalpel under a stereoscope (Zeiss Stemi 2000-C, Fisher Scientific, United Kingdom) and the ventral exoskeleton was pinned back. The viscera was removed to reveal the dorsal vessel, and photos (Nikon D90, Nikon, USA) of the exposed dorsal vessel were taken. These images were used for measurements of heart length, number of pairs of alary muscles, and length of each alary muscle pair along the heart. Measurements were made using ImageJ [164]. The dorsal vessel of 12 *Zophobas morio* adults were dissected and photographed for measurements. The entire heart was not always visible in every dissection, but measurements of visible alary muscle pairs were made from each specimen.

5.2.3 Fluorescent staining

Beetles were anesthetized on ice and the legs, elytra, and wings were removed using dissecting scissors. Lateral incisions were made down both sides of the abdomen and thorax, with transverse incisions to remove the ventral surface of the abdomen and thorax. The head was removed with a scalpel and the viscera were delicately removed using tweezers. Staining and imaging were then performed with the help of Dr. Julián Hillyer and Garrett League at Vanderbilt University following protocol described in [20]. Specimens were washed with PBS 1x, fixed in 16% paraformaldehyde, washed again with PBS 1x, and stained in a 0.3 μmol I-1 phalloidin-Alexa Fluor 488 in PBS with 2 μL Triton X-100 added. They were then mounted with Aqua Poly/Mount on a slide and imaged on a compound fluorescent scope (Nikon 90i, Nikon, USA) with an attached camera (Nikon Digital Sight DS-QilMc, Nikon, USA). Z-stacks for each specimen were collected and combined to form single focused image using EDF module of NIS-Elements. Fluorescent staining was done in one *Zophobas morio* adult.

5.2.4 Microtome sectioning

In order to view and measure the cross-section of the *Zophobos morio* heart, we also dissected, fixed, and sectioned thin slices of the heart. The dorsal vessel was dissected as described previously except the beetle was anesthetized via dry nitrogen gas beforehand. Anesthetization allowed us to view the heart pumping throughout dissection to verify that muscular structures which stabilize the heart were not injured during dissection, as these might affect heart cross-section. The lateral and ventral exoskeleton as well as the head and thorax were removed. Fixation and sectioning were performed at the Virginia-Maryland College of Veterinary Medicine Morphology Laboratory. The remaining dorsal section of the abdomen was placed into cacodylate buffer (pH=7.1) for at least 24 hours before fixation in 25% glutardialdehyde solution for 2 hours at 4°C. The specimen was then washed three times with buffer before fixation in 1.5% osmium tetroxide in buffer, followed by washing in buffer three more times, all at 2°C. The sample was then dehydrated in a graded alcohol series with 30 min each at 70% (2°C), 80%, 90%, 96%, and twice at 100% (room temperature: ~22°C). As an intermedium, the sample was then placed in 50%, 75%, and three times at 100% propylenoxide for 15 minutes each, before being left overnight in a 9:1 mix of propylenoxide and Epon (812, epoxipropyl ether of glycerol) mixture to allow evaporation of propylenoxide. Finally, the sample was embedded in fresh 100% Epon for 24-72 hours at 60°C for polymerization.

The embedded sample was then sectioned, beginning at the posterior end, using a microtome (Leica Ultracut UCT, Leica Microsystems, Buffalo Grove, Illinois) at 1.0-1.5 μm thickness. After 2-5 sections were obtained, approximately 100 μm of the sample was removed before another 2-5 sections were obtained. Sections were dried on a low-temperature hot plate before staining with 1% toluidine and 0.5% safranin O dye then fixing on a glass slide. Images of each section were obtained using a light microscope (JEM-1400, JEOL, Peabody, Massachusetts). Measurements within each image were made using ImageJ [164]. Cross-sectional area of the heart was measured by outlining the inner surface of the heart wall. To measure heart wall thickness, 4 measurements were made for each section, 1 each at the dorsal, ventral, and both lateral sides of the heart cross section from the inner to the outer surface of the heart wall (Figure 5.1). Also, distance of the heart to the dorsal exoskeleton was measured via a straight line from the outer surface of the exoskeleton to the inner surface of the dorsal heart wall (Figure 5.1). The dorsal vessel of one beetle was sectioned via microtome, across a length of 4.9 mm of the dorsal vessel, resulting in 135 total sections.

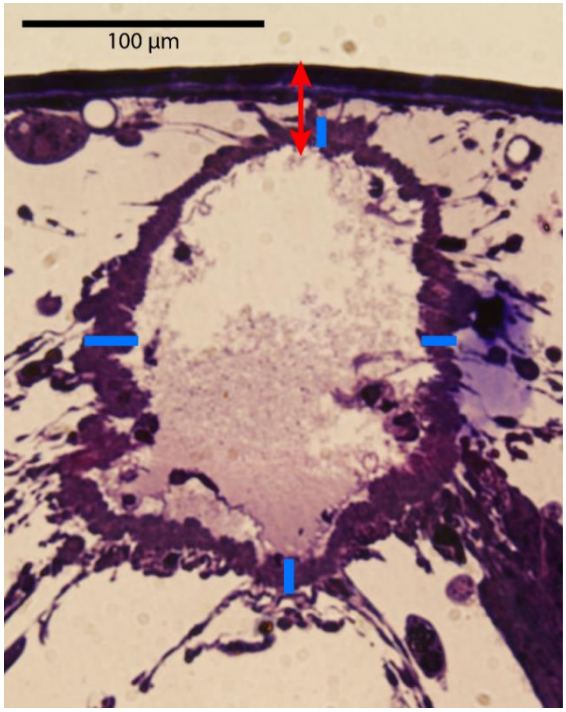

Figure 5.1: Microtome section of the dorsal vessel of a *Zophobas morio* beetle, showing image measurements of wall thickness (blue lines) and distance from the dorsal surface (red arrow).

5.2.5 Infrared sensor measurements

Additionally, we measured the speed of contraction down the length of the heart using infrared sensors aimed at the heart through the dorsal surface of the beetle. Beetles were anesthetized using dry nitrogen gas before mounted on sticky tack with legs restrained. The elytra and wings were pinned back to reveal the dorsal surface of the abdomen. Animals were then left alone to acclimate for at least 25 minutes to allow heart rate to return to resting rate. Two infrared (IR) sensors (FD-T80 Diffuse Reflective Fiber Optic Cable, Sunx Sensors, West Des Moines, Iowa) connected to an amplifier (FX-11A Slim Body Analog Fiber Sensor, Sunx Sensors, West Des Moines, Iowa) were aimed 8 mm apart at the midline of the dorsal surface of the abdomen directly over the dorsal vessel. IR readings were collected digitally using a custom Arduino circuit (Arduino UNO, arduino.org) and Python script. The IR sensors detected small changes in distance between the dorsal vessel and the sensor, created by the heartbeat or movement of the abdominal surface. Measurements were collected at the highest sampling rate the circuit and computer were capable of, which resulted in varying sampling rate throughout each trial. Sampling rate was calculated using the reported time as approximately 2271 to 2650 Hz on average for each 1-2 min trial.

Movement of the beetle during measurement created large changes in the IR signal, obscuring the heart rate signal, so sections between movements were identified for analysis, ranging from 5.3 to 26.1 s in length. For each section, the time at which contraction began was identified for each heart beat as the point at which the IR reading began to decrease. Assuming anterograde pumping of the heart, contraction of the heart would be read by the posteriorly placed IR sensor first. Thus, the difference between the time at the start of contraction for the posteriorly placed IR sensor to the anteriorly placed IR sensor was calculated as the travel time for the wave of contraction down the heart during pumping. Knowing the distance between the sensors, the wave speed was calculated. Heart contraction wave speed was calculated for 9 *Zophobas morio* adults.

5.2.6 Ultrasound imaging

After IR sensor measurements, the dorsal vessel was viewed in the same beetles via ultrasound imaging (Vevo 2100 with MS700 transducer, Visualsonics, Canada) at 50 MHz to view changes in the cross-section of the heart as it pumps, in both the transverse and longitudinal view. Ultrasound image depth was maintained at 4 mm, with image width varying for each ultrasound video. Ultrasound transmission gel (Aquasonic 100, AquasonicGel, Michigan) was placed between the ultrasound transducer and the dorsal surface of the animal, being careful not to obscure the spiracles, located laterally near the abdominal margin. Ultrasound videos were collected of both the transverse and longitudinal view of the beetle heart at 50 to 287 fps, depending on image size, which ranged from 3 by 2.73 mm to 3 by 9.73 mm. In total, the heart of 14 beetles were viewed and recorded via ultrasound, in both transverse and longitudinal views.

In many of the videos in transverse view, the heart wall was observed to fully contract and occlude the tubular heart. However, in some videos, the heart wall did not fully occlude the lumen and can be clearly seen at full contraction. From these instances, the cross-sectional area of the heart at full dilation and contraction for 10 consecutive pumping events in transverse views of the heart in 7 beetles were measured using ImageJ [164]. From these measurements of cross-sectional area, the percent occlusion of the heart during contraction was calculated as the difference in area at dilation to area at contraction. For 4 beetles, ultrasound videos of transverse views of the heart were recorded at increments of 0.2 mm down the length of the heart, moving anteriorly a total of 4 mm. The cross-sectional area of the heart at full dilation for 5 consecutive pumping events was measured for each ultrasound video down the length of the heart using ImageJ [164].

In longitudinal view, the wave-like contraction of the heart can be viewed as it travels down a length of the heart in view. Using MATLAB, the distance between the dorsal surface and an easily identifiable point on the tissues on or around the heart were tracked over time in two locations along the length of the dorsal vessel (Figure 5.10). As the heart contracted, this distance decreased, and as the heart relaxed, this distance increased. For each heartbeat, the time at which contraction began was identified as the point at which the distance began to decrease (Figure 5.11). The sections of ultrasound video analyzed using this method all showed clear anterograde pumping of the heart. Thus, the difference between the time at the start of contraction for the posterior measurement to the anterior measurement was calculated as the travel time for the wave of contraction down the heart during pumping. The distance between the two measurements was also measured which allowed for calculation of contraction wave speed. Heart contraction wave speed was calculated for 3 *Zophobas morio* adults.

5.2.7 Statistical analyses

R (Foundation for open Access Statistics) was used for all statistical analyses. A linear model (LM) was used to test for the effect of one variable upon another. Analysis of variance (ANOVA) was used to compare values to determine any differences. Post-hoc analysis to determine which means differed in multiple comparison ANOVA was done using Tukey's range test.

5.3 Results

5.3.1 Dissection

The length of the dissected heart was 10.9 ± 0.7 mm (average ± S.D.)(n=10), ranging from 10.1 to 12.1 mm. Heart length was not correlated with total body length (LM: F = 1.575, df = 9, p = 0.241), but did correlate with mass (LM: F = 6.092, df = 9, p<0.04). Each beetle had 6 pairs of alary muscles (Figure 5.2). The anterior 5 pairs of alary muscles were similar in size, with an average width of 1.90 ± 0.20 mm, ranging from 1.46 to 2.30 mm. The posterior-most alary muscle pair was significantly smaller in width than the other 5 pairs (ANOVA with Tukey's HSD: p<0.0001; Table 5.1), with an average width of 0.81 ± 0.10 mm.

Table 5.1: Summary of ANOVA comparing alary muscle width for each alary muscle pair from most anterior to posterior.

Source	df	MS	*F*	*P*
Alary pair	5	0.9245	25.66	<0.0001
Residuals	46	0.0360		

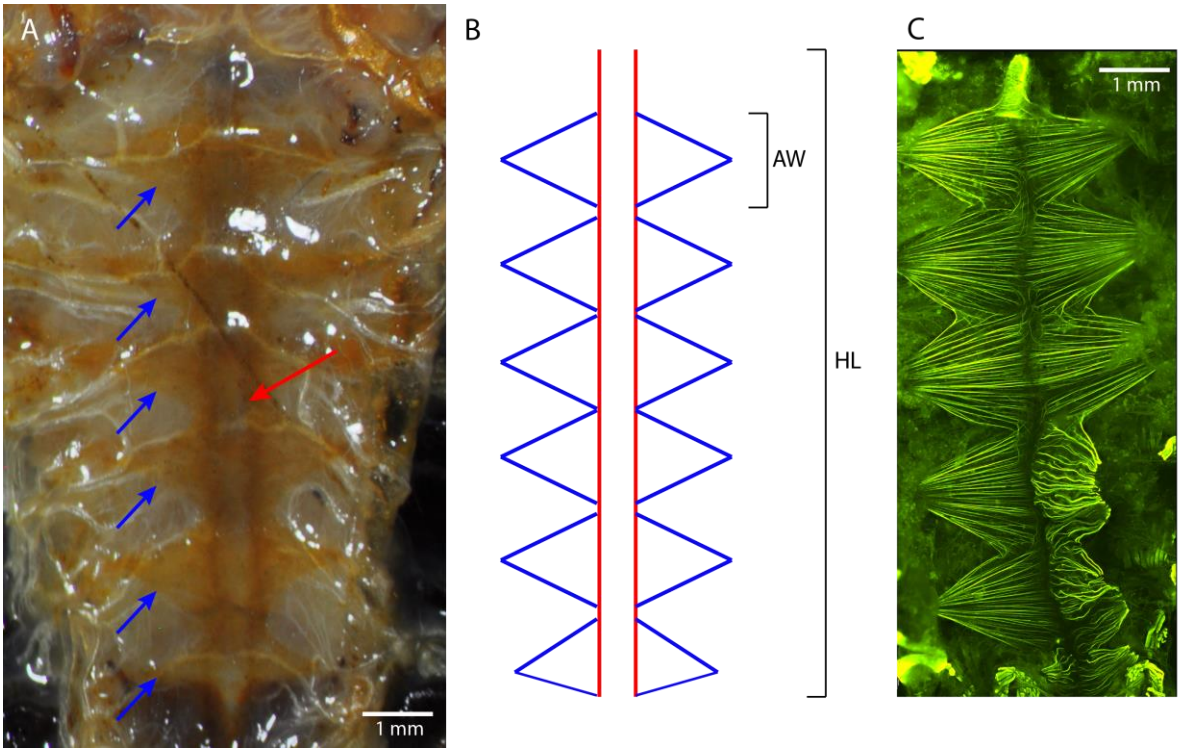

Figure 5.2: Photo of the dissected dorsal vessel (A), showing the inner portion of the dorsal surface of a *Zophobas morio* beetle where anterior is at the top of the photo and posterior is at the bottom. Schematic representation of the heart and alary muscles (B) is also shown, where blue lines and arrows indicate the diamond-shaped alary muscle pairs that surround the ride lines and arrows which indicate the heart. Measurements of heart length (HL) and alary muscle width (AW) are represented as well. Photo of the fluorescent stained heart with alary muscles is also shown (C) in the same orientation. The alary muscles in this specimen were damaged during dissection, causing them to lose tension and appear crumpled.

5.3.2 Fluorescent staining

Fluorescent staining showed alary muscle pairs down the length of the heart, although some were damaged during dissection (Figure 5.2). Due to this damage, the muscles did not maintain tension on the heart and altered the natural shape of the heart. The posterior-most alary muscle pair was also not visible. Connections between alary muscles and the heart occurred across the ventral surface of the heart, obscuring the view of the heart itself. However, helically wound muscle fibers were identified on the heart (Figure 5.3).

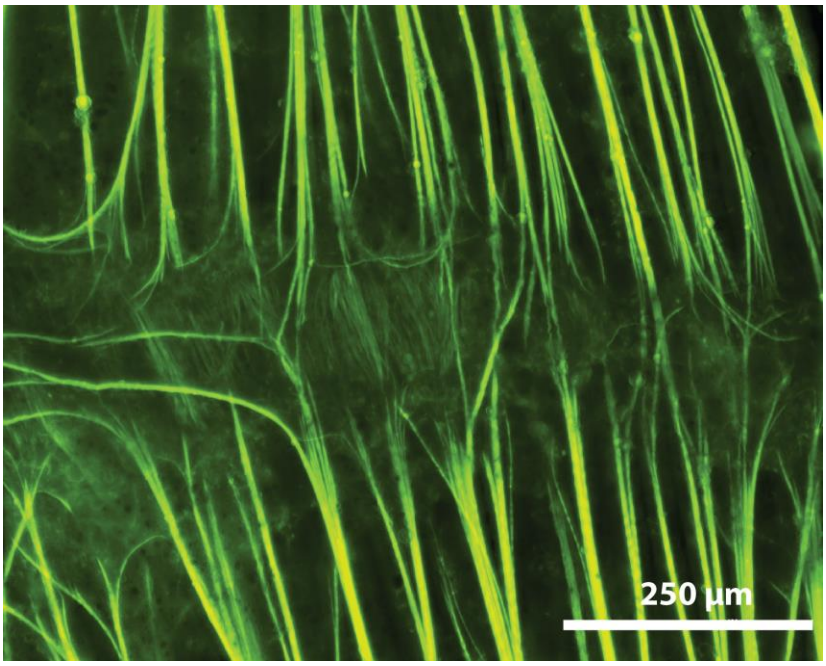

Figure 5.3: Zoomed-in view of the heart of a *Zophobas morio* adult, where anterior is left and posterior is right. The hearts runs from left to right through the center of the bright alary muscle fibers. The helical musculature is faint but visible on the heart.

5.3.3 Microtome sectioning

The cross-sectional area of the heart was 0.0182 ± 0.0099 mm^2 (average ± S.D.), ranging from 0.0010 to 0.0416 mm^2 (Figure 5.4A). The thickness of the heart wall was 0.0194 ± 0.0093 mm, ranging from 0.004 to 0.066 mm (Figure 5.4C). The distance from the dorsal surface to the inside of the heart was 0.0506 ± 0.0362 mm, ranging from 0.0189 to 0.2366 mm (Figure 5.4B). Cross-sectional area of the heart varied with both heart wall thickness (LM: $F = 104$, $df = 130$, $p<0.0001$; Figure 5.5A) and distance from the dorsal surface (LM: $F = 38.65$, $df = 128$, $p<0.0001$; Figure 5.5B), showing a decrease in area with an increase in both wall thickness and distance from the dorsal surface. Thickness increased with distance from the dorsal surface (LM: $F = 67.3$, $df = 128$, $p<0.0001$; Figure 5.5C).

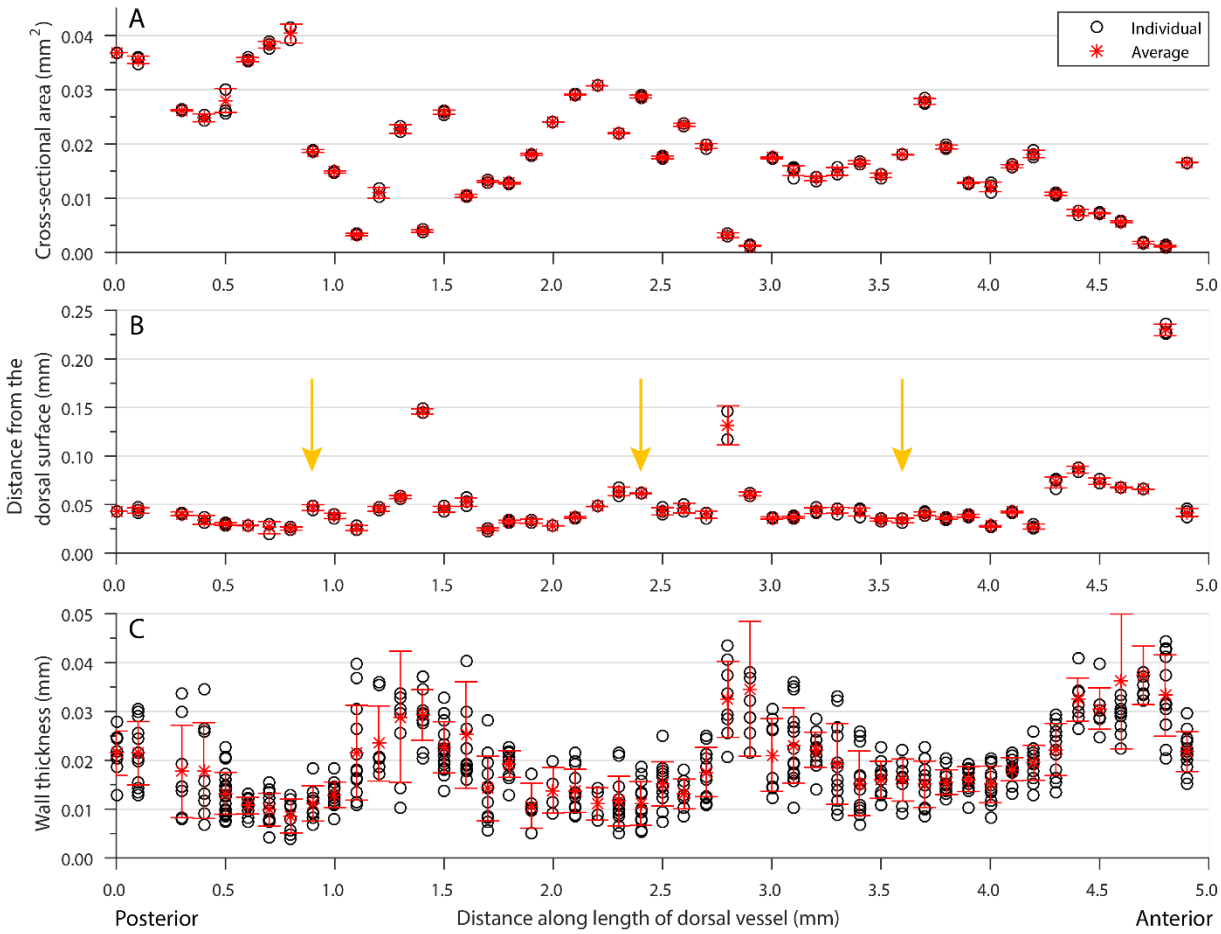

Figure 5.4: Cross-sectional area (A), distance from the dorsal surface (B), and wall thickness (C) of the dorsal vessel of a *Zophobas morio* adult across the length of the dorsal vessel. Open, black circles indicate individual measurements and red stars indicate average values for each distance along the length of the heart with bars to denote standard deviation. Locations of valve-like structures (Figure 5.6) are indicated by orange arrows.

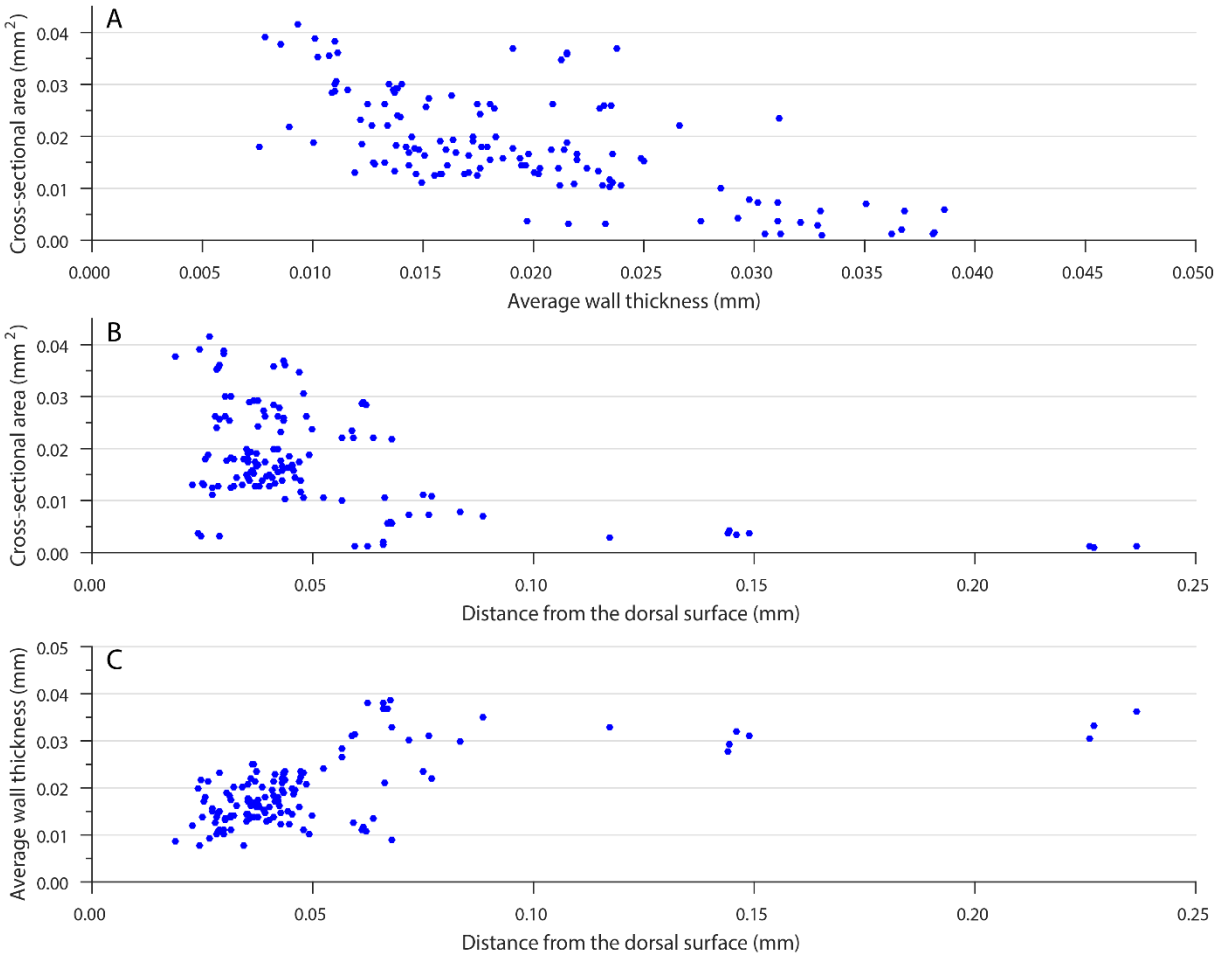

Figure 5.5: Cross-sectional area vs average wall thickness (A) and vs distance from the dorsal surface (C) of the dorsal vessel. As average wall thickness and distance from the dorsal surface increase, cross-sectional area decreases. Average wall thickness vs distance from the dorsal surface (C) of the dorsal vessel is also shown. As distance from the dorsal surface increases, average wall thickness also increases.

At regular intervals along the length of the dorsal vessel, large increases in wall thickness and distance from the dorsal vessel occur with large decreases in cross-sectional area. These changes occurred at distances of approximately 1.4, 2.8, and 4.8 mm (Figure 5.4). Appearance of folds in the exoskeleton above the dorsal surface identify these locations as occuring where sclerites overlap along the dorsal surface, and may indicate the change from one heart chamber to the next. If so, this would indicate heart chamber lengths of 1.4 and 2.0 mm.

Additionally, at three locations down the length of the dorsal vessel, the cross-sectional shape of the heart appeared less regular, showing inward folds of the heart wall (Figure 5.6). These occurred at distances of 0.9, 2.4, and 3.6 mm along the length of the dorsal vessel, with one in each of the potential heart chambers (Figure 5.4).

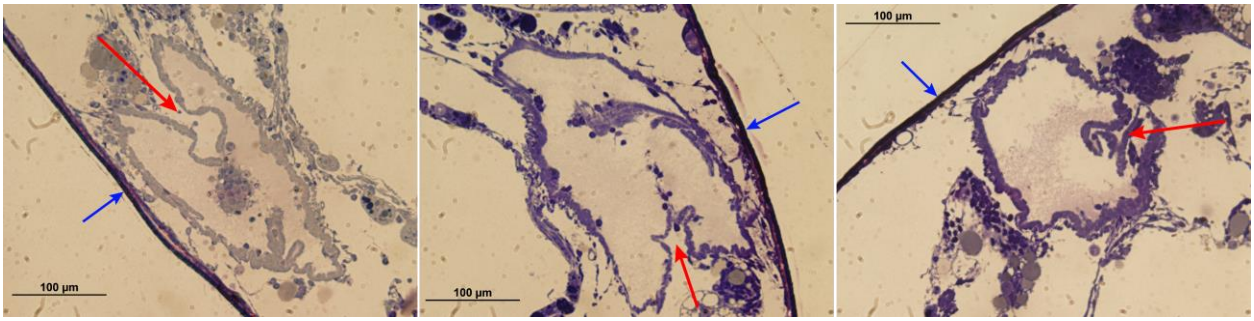

Figure 5.6: Microtome sections of the dorsal vessel of a *Zophobas morio* beetle at distances of 0.9 (A), 2.4 (B), and 3.6 (C) mm down the length of the dorsal vessel. The dorsal surface of the exoskeleton is indicated with blue arrows. The heart wall appears to fold inward on the right lateral side of each cross-section, indicated with red arrows. These inward folds of the heart wall may denote ostial valves in the heart, where hemolymph enters.

5.3.4 IR readings

Based on IR sensor readings 8 mm apart along the dorsal surface above the heart, the speed of contraction down the heart during pumping was 18.6 ± 8.8 mm/s, ranging from 5.9 to 32.0 mm/s (Figure 5.7).

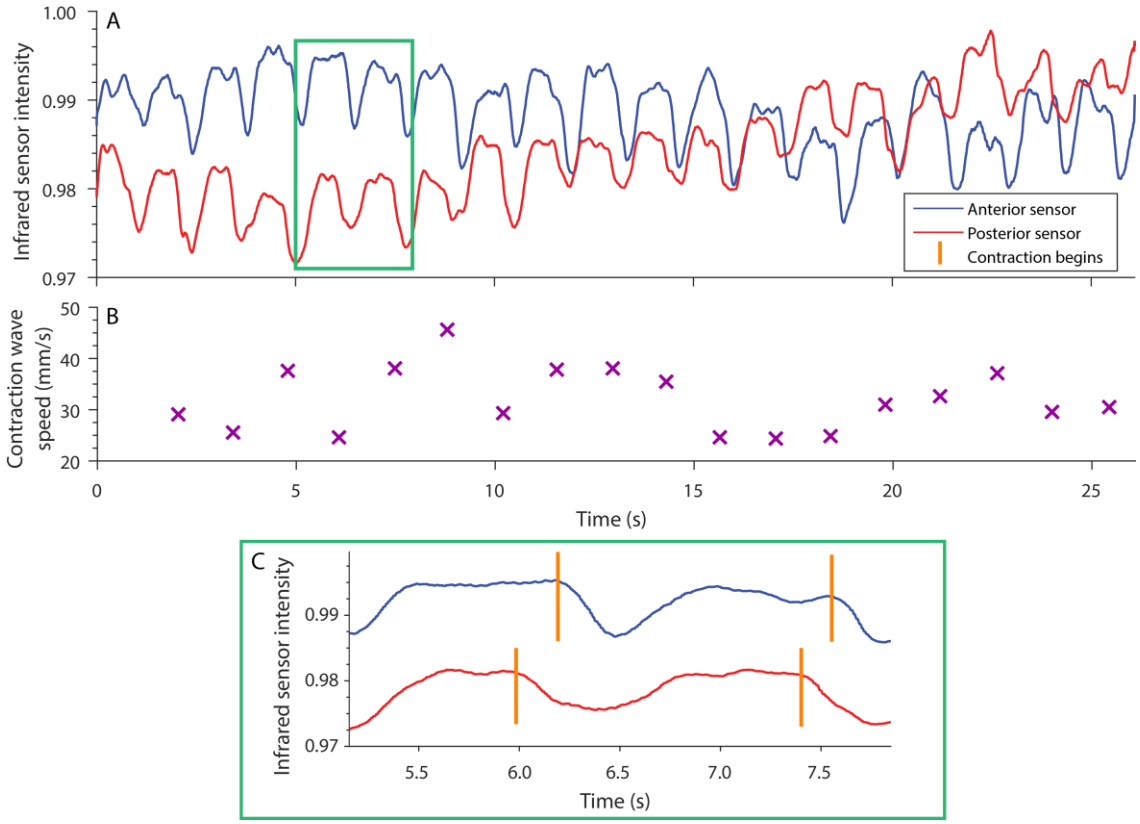

Figure 5.7: Sample smoothed IR trace (A) showing IR intensity for the anterior and posterior sensor over time as well as contraction speed for each heart pump over time (B). Average sampling rate for this trace is 1304 Hz. This trace has been smoothed using a moving window smoothing in MATLAB with a window width of 150 points, unsmoothed trace is shown in Figure D.1.3 as Animal 10. Inset (C) shows a section of the data from 5 to 8 s where the times at which contraction of the dorsal vessel begins are labelled.

5.3.5 Transverse ultrasound imaging

Based on a transverse view of the dorsal vessel via ultrasound, the heart becomes 100% occluded during pumping events at some locations along its length. However, in some locations, full occlusion does not occur (Figure 5.8). At locations with minimal occlusion in 7 *Zophobas morio* adults, the heart became 81.6 ± 6.7% occluded, ranging from 65.4 to 91.4%.

Cross-sectional area of the dorsal vessel at full dilation down a 4 mm length of 3 insects was 0.1016 ± 0.0416 mm^2, ranging from 0.0350 to 0.2220 mm^2. Shape of the cross-section of the heart at full dilation varied, appearing circular in some sections and oval in shape in others. At regular intervals down the length of the dorsal vessel, cross-sectional area decreased, possibly indicating a change from one heart chamber to the next (Figure 5.9). Based on the location with the minimum cross-sectional area each time area decreased, heart chamber lengths would be 1.4, 1.8, and 2.6 mm.

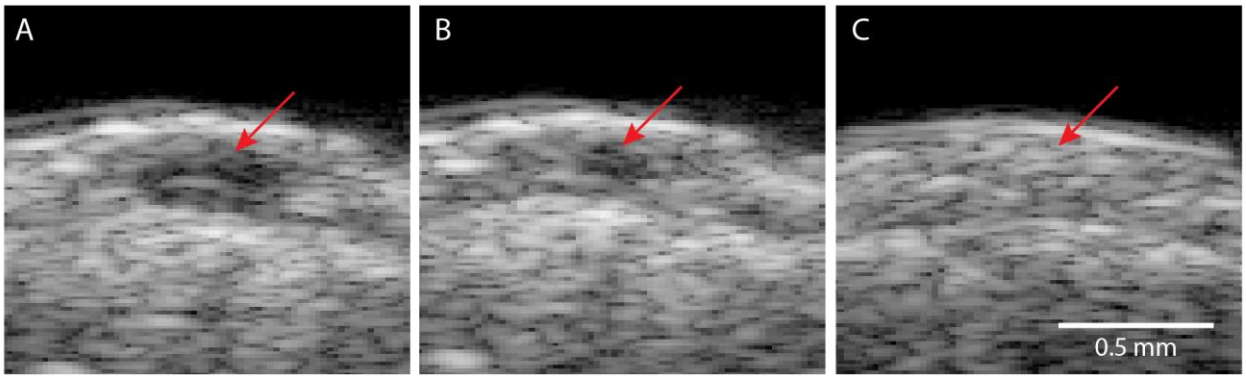

Figure 5.8: Ultrasound image of transverse view of the dorsal vessel (red arrows) in a *Zophobas morio* adult at full dilation (A) and contraction (B) showing occlusion of the heart during pumping. For comparison, full occlusion of the dorsal vessel (C) at a different location down the length of the heart is shown.

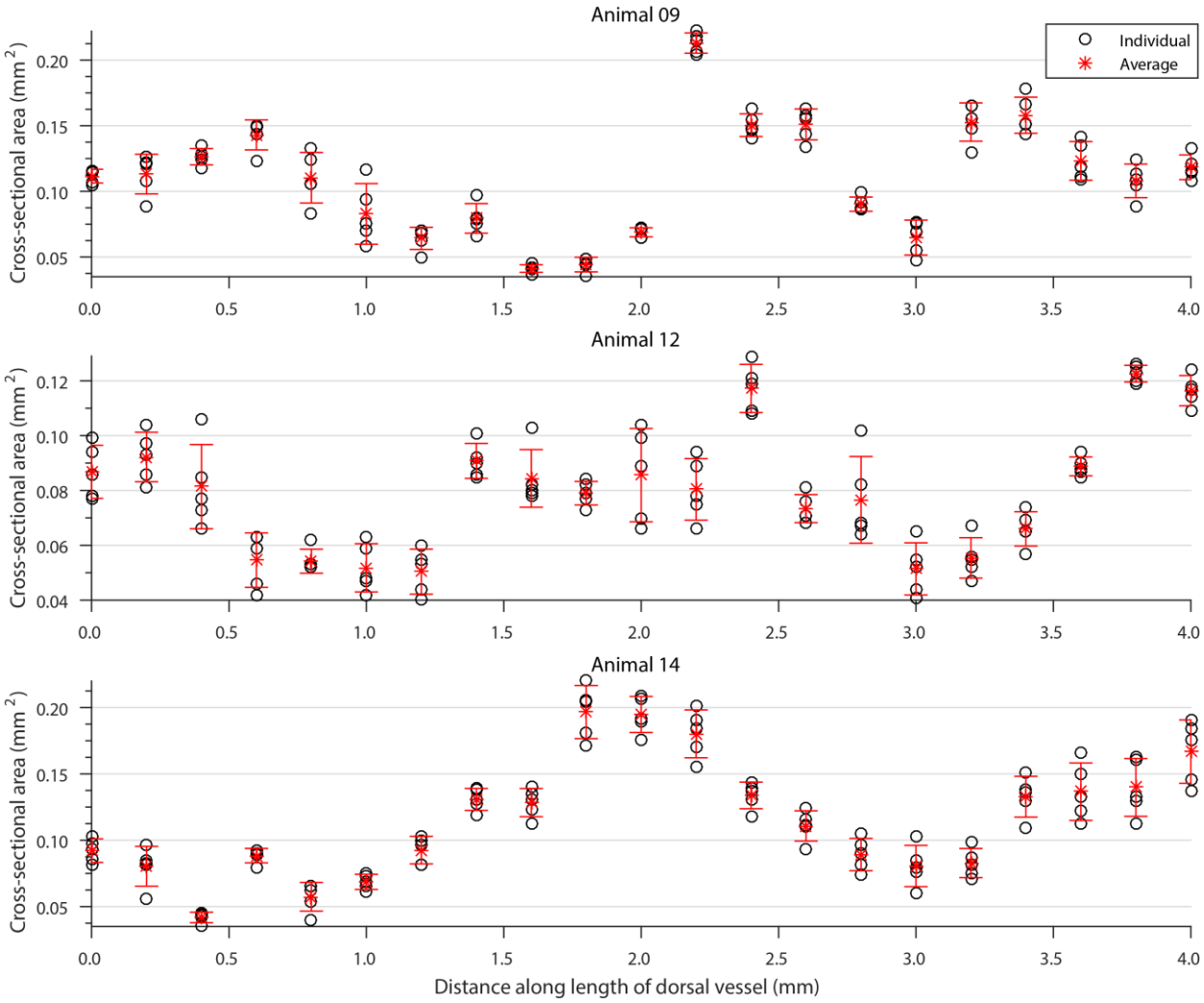

Figure 5.9: Cross-sectional area of the dorsal vessel of three *Zophobas morio* adults at full dilation down the length of the heart. Open, black circles indicate individual measurements and red stars indicate average values for each distance along the length of the heart with bars to denote standard deviation.

5.3.6 Longitudinal ultrasound imaging

Measurements of contraction distance were made for 7 to 14 consecutive heartbeats 2.1 to 2.6 mm along the length of the heart, allowing for measurements in two consecutive heart chambers (Figure 5.10). The speed of contraction down the heart during pumping was 18.1 ± 4.3 mm/s, ranging from 10.2 to 27.3 mm/s.

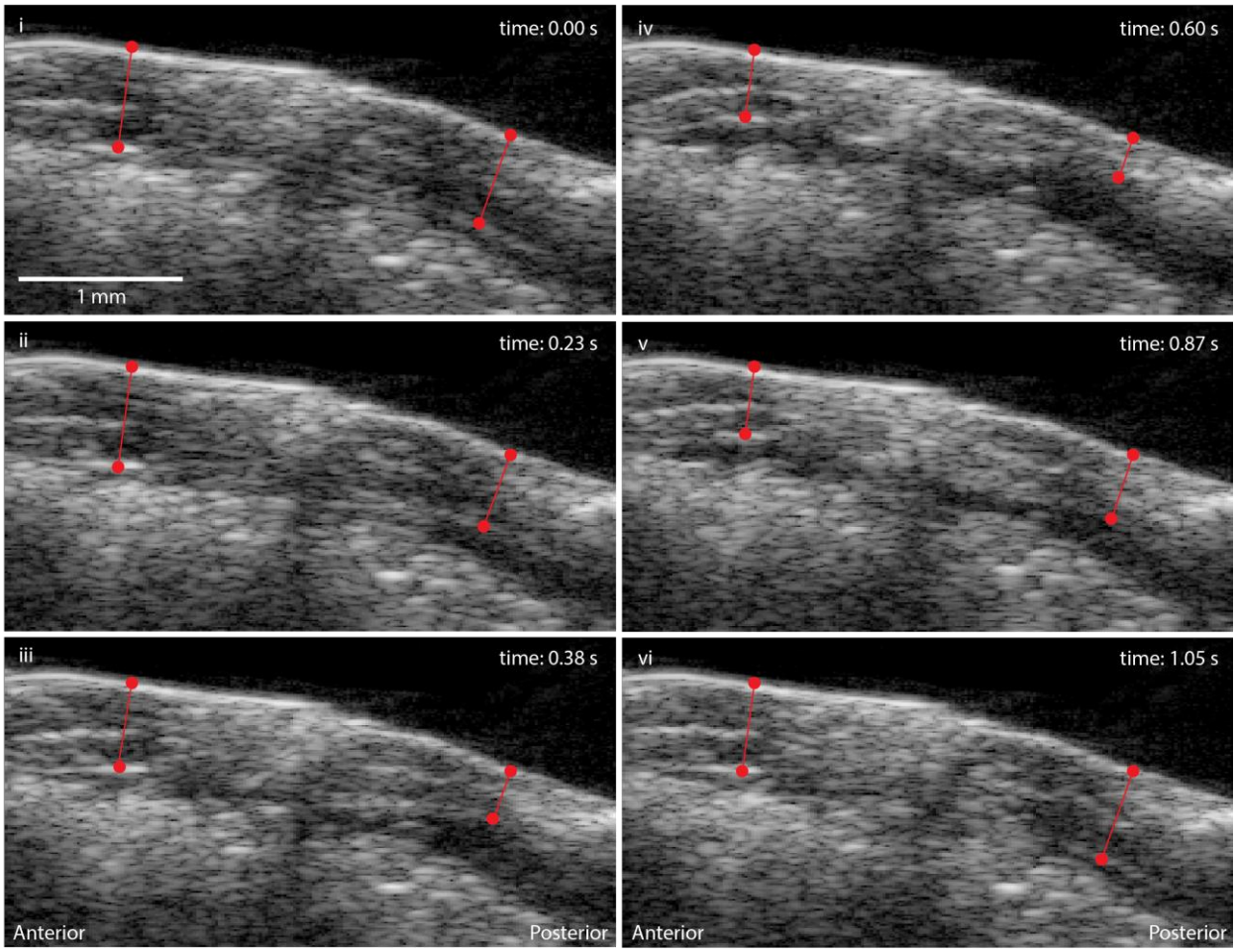

Figure 5.10: Ultrasound images of the longitudinal view of the dorsal vessel spanning two abdominal segments in a *Zophobas morio* adult. Ultrasound images were collected at a sampling rate of 197 Hz. Red filled-in circles represent tracked points with red lines showing distance between them. Images show the heart through a full pumping cycle (i-vi) as the contraction wave travels down the length of the heart.

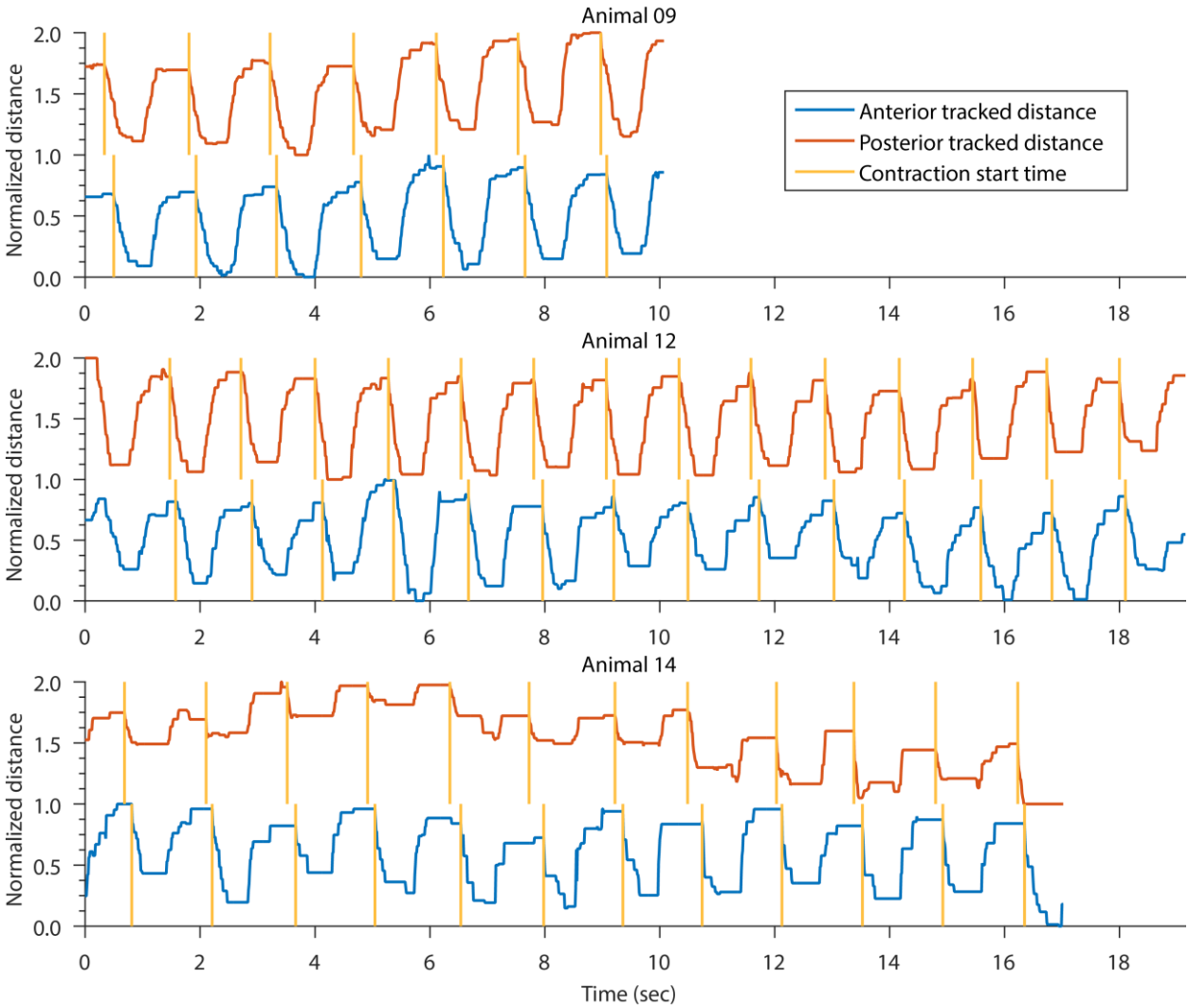

Figure 5.11: Distance between the heart and the dorsal surface over time for two locations along the heart in longitudinal ultrasound videos of three *Zophobas morio* adults. Distance was measured in two consecutive heart chambers, and decreases with heart contraction. Times at which contraction began for each heartbeat are labelled. Distance was measured between tracked points on the dorsal surface and an easily identifiable point on the tissues on or around the heart. Ultrasound images were collected at a frame rate of 98, 77, and 95 Hz for animals 9, 12, and 14, respectively.

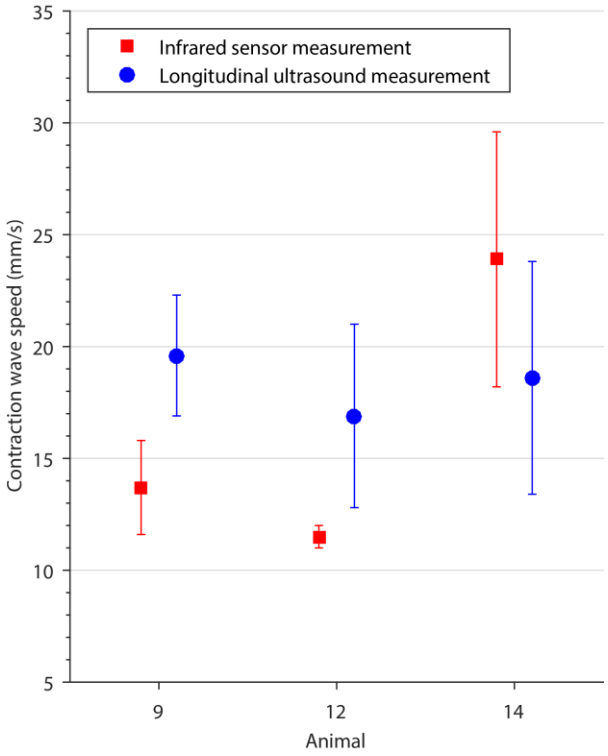

Figure 5.12: Contraction wave speed down the length of the dorsal vessel in three *Zophobas morio* adults measured using infrared sensors and longitudinal ultrasound. Measurements via infrared sensors were collected approximately 10, 8, and 30 min prior to ultrasound image collection for animals 9, 12, and 14, respectively. Filled markers indicate average values for each measurement and animal, with bars to denote standard deviation.

5.4 Discussion

Here, measurements of the morphology and kinematics of the heart in *Zophobas morio* adults are presented for the first time. Dissection and microtome sectioning provided detailed views of the structure of the heart in which length, cross-sectional area, and chamber length were measured. IR sensors and ultrasound imaging provided measurements of the heart in motion to determine the heart wall kinematics throughout heart pumping. These measurements included cross-sectional area at maximum dilation, percent occlusion of the heart during pumping, and contraction wave speed down the length of the heart. These are the first measurements of heart wall kinematics in an insect species, and provide the foundation for developing a model of the dorsal vessel to better understand circulatory flow within insects.

Previously, the morphology of the insect heart has only been studied in detail in *Anopheles gambiae* [19, 20], *Rhodnius prolixus* [18], *Tenebrio molitor* [159], and *Drosophila melanogaster* [158, 165]. These species and *Z. morio* adults vary considerably in mass, length, and shape, meaning direct measurements of heart morphology may not be exactly comparable; however, similarities in structure can be seen. In *Z. morio*, the heart is 10.9 mm long, which is approximately 44% of the total length of the insect. In other species, the heart extends through the abdomen only [20, 158] as it does here, with the aorta extending through the thorax and head so that the dorsal vessel runs the entire length of the body [18, 20]. While the number of alary muscle pairs varies with each species, from four in *D. melanogaster* [158] to seven in *R. prolixus* [18], the presence of a smaller, posterior pair appears in each insect. In fact, in *A. gambiae*, there are six complete pairs of alary muscles, with musculature resembling the anterior half of an alary muscle pair at the posterior end of the heart [19]. In dissections of *Z. morio* adults, we found six alary muscle pairs, where the posterior pair was only half as wide as the five more anterior pairs, which, similar to *A. gambiae*, might be only the anterior half of a full alary muscle pair. Additionally, we measured the length of the heart

chambers using three different methods: dissection, microtome sectioning, and transverse ultrasound imaging. Measurements from the three methods were similar, finding the length of heart chambers to be 1.9 ± 0.2, 1.7 ± 0.4, and 1.9 ± 0.6 mm, respectively. Variation in cross-sectional area and wall thickness of the heart within each chamber has been observed in *A. gambiae* as well [19]. This variation has been attributed to the tension created by the alary muscles on the heart wall, which would be minimal at the location between chambers where an alary muscle pair ends and a new one begins. A lack of tension from the alary muscles would decrease area, allowing the heart wall to fold inward and appear thicker, giving the heart a segmented appearance that resembles chambers [19]. Ostial valves along the heart were found in each of the heart chambers sectioned, which was similarly observed in *A. gambiae* [19, 20]. Essentially, the morphological characteristics of the heart in adult beetles is similar to those of other insect species.

Cross-sectional area of the heart down its length varied considerably between microtome sectioning and transverse ultrasound measurements. The largest cross-sectional area measured via ultrasound was nearly five-fold the largest measurement via sectioning. This difference is likely due to the state of the heart during each of these measurements. For sectioning, the heart had been dissected, which likely altered the natural state, particularly by potentially severing muscular or tissue connections that hold the heart open. The heart was also fixed in a completely relaxed state for sectioning, whereas ultrasound measurements were taken on the heart at full dilation. During dilation, muscles may be functioning to dilate the heart to a greater extent than when at rest. Transverse ultrasound measurements may represent the largest possible cross-sectional area of the heart, whereas microtome sections yield the cross-sectional area at rest.

Based on ultrasound data, the heart of *Z. morio* adults does experience full, 100% occlusion during systole in some parts of the heart. However, some sections along the length do not fully constrict, experiencing as little as 65% occlusion. In *A. gambiae*, regions of the heart were noted to experience full constriction; however, tube occlusion varied with flow direction [19]. In models of peristaltic flow within tubes, occlusion percent can significantly affect both average and maximum flow speed, as well as backflow and pressure differences [161, 166]. In fact, in numerical models with large occlusion ratios and long wavelengths, as is seen here in the insect heart, the flow velocity exceeds the speed of the contraction wave [166]. Average occlusion even exceeded 80%, at which the maximum flow speeds can be nearly double the contraction wave speed with short wavelengths [161]. However, we did observe differences in occlusion along the length of the heart as well, finding areas of 100% occlusion where cross sectional area was smallest. It is possible that the area between heart chambers constricts completely, while the middle of the chamber does not. This variation in occlusion across heart chambers may function to prevent backflow or to vary pressure differences across and within the heart, as pressure will increase with occlusion [161]. While numerical simulations of peristaltic tubular pumps can give us an idea of how the insect heart functions to produce hemolymph flow, the heart is more complex than previously thought and may require a more detailed model including chambers and varying occlusion to better understand the flow within.

We found that the anterograde contraction wave moves down the length of the heart at about 18 mm/s. IR and longitudinal ultrasound views generally agreed in this measurement (Figure 5.12), and a limited number of consistent heartbeats recorded via IR may contribute to differences between measurement types. Previously, contraction wave speed down the heart had not been measured using direct measurements of the heart wall kinematics. In *Manduca sexta* pupae, the speed of the anterograde peristaltic waves down the heart was measured using thermographic sensors to be about 60 mm/s at 24°C [167]. In *Tenebrio molitor*, a tenebrionid beetle similar in size to *Z. morio*, the contraction wave speed was measured using intracellular electrodes to measure the wave of depolarization traveling down the heart; with a heart rate of 60 bpm, a

conduction velocity of 14 mm/s was measured in the heart [159]. These wave speeds are similar in magnitude to what has been found here. Wave speed will significantly affect flow speeds of hemolymph through the heart, where increased wave speed will increase flow speed nonlinearly. However, as wave speed increases, back flow within the heart is predicted to increase in numerical models of peristaltic tubular pumps [161]. Additionally, it is likely that hemolymph flow speed exceeds the wave speed of 18 mm/s, considering that we observed 80% or more occlusion on average [161]. Future measurements of hemolymph flow speed would be advantageous for comparing contraction wave speed and to further understand the relationship between heart wall kinematics and hemolymph flow within the heart.

This is the first study to measure heart wall kinematics during pumping in an insect species. It also provides the first morphological data of the heart in *Zophobas morio* adults. Understanding both the morphology and kinematics of the heart will help us to ultimately understand and model hemolymph flow generation within the heart. Here, we found a more complex system including heart chambers with varying cross-sectional area and occlusion during pumping, which requires a more complex model of flow than has been previously considered. Modeling the peristaltic pumping of the heart will be valuable to fully understand the structure and function of the dorsal vessel and circulatory system as a whole.

Acknowledgements

We acknowledge the assistance of Dr. Hodjat Pendar, Joshua Pulliam, and Michelle Prisbe. In particular, we would like to thank Kathy Lowe at the Virginia-Maryland College of Veterinary Medicine for help with microtome fixation and sectioning. We thank Dr. Craig Goergen and Arvin Soepriatna for use of the ultrasound machine and help with imaging. We also thank Dr. Julián Hillyer and Garrett League for help with fluorescent staining and discussion. Lastly, we thank Dr. Dan Sweeney for Arduino and code assistance. Partially funded by NSF 1558052 and 0966125.

Chapter 6

Conclusions

The major goal of this dissertation was to study the structural and kinematics of portions of the insect respiratory and circulatory systems to better understand how they function to transport fluids at the microscale. To accomplish this goal, I used various experimental and data analysis techniques, including synchrotron x-ray microtomography, b-mode ultrasound videography, image analysis and processing, as well as viscosity, behavioral, and composition measurements. Specifically, within this dissertation I characterized the geometry of the tracheal network, the physical properties of hemolymph, as well as the morphology and kinematics of the heart in insects. This chapter provides a brief summary of these results and poses new areas for future research.

6.1 Tracheal network

In Chapter 2, I found that Murray's law does not apply to the tracheal system of *Platynus decentis* adults. Instead, I found that x=2.14 with k=1 (equation (2.1) in Chapter 2) for the tracheal network, which differs from other biological transport networks. It is likely that the assumptions of Murray's law do not apply to the tracheal system, including the mechanisms of flow generation or metabolic maintenance costs. To test these assumptions, studies of additional insect species and development stages is warranted.

The method of flow generation in insects is a mixed system, employing a combination of active ventilation and diffusion. Murray's law assumes an energetic cost to the organism to move fluid against the viscous resistance of the vessel wall, which is true for active ventilation, but not for diffusion. *Platynus decentis* adults are known to utilize rhythmic tracheal compression [9], but also employ diffusion to transport oxygen to tissues and CO_2 to the environment. In contrast, *Tenebrio molitor* larvae use only diffusion for the transport of gases within the tracheal network [168]. In theory, an optimal tracheal network for a solely diffusive system would maintain x=2, k=1 (equation (2.1) in Chapter 2) for all branching groups [39, 44]. Measurement of the tracheal geometry of these larvae using the methods in Chapter 2 could be used to test this theory. In fact, microtomography of *T. molitor* larvae, pupae, and adults has already been collected by Rás et al. [169] and could be used for this analysis. Additionally, active ventilation has been studied across several species, including some ant, bumble bee, and fly species [7, 54]. Although the exact contribution of active ventilation and diffusion for airflow within the tracheal system is unknown in any species,

measurement of the tracheal geometry within additional species may illuminate patterns between active ventilation behaviors and geometry.

For optimal network design, Murray's law also assumes a cost for the organism to maintain the network through its functional life. Although the tracheal network is known to change throughout insect development [11, 62-65] which requires some metabolic cost, it does not change continuously. Larger changes, notably in the tracheal diameter and formation of new tracheoles, occur only at molts [62, 64, 65] suggesting that the cost to maintain the tracheal system varies throughout development. Thus, the geometry of the system may vary as well. Analysis of tracheal branching geometry at various developmental stages of a single insect species would provide a better understanding of how the cost of metabolic maintenance may contribute to the morphology of the tracheal network.

The results of Chapter 2 represent the first test of Murray's law in the insect tracheal system. While these results provide a deeper understanding of the physiology of the tracheal system, there are still gaps in our full understanding of flow considerations and production within the respiratory system. The methods used here provide an opportunity for future measurements in other species and development stages to fill those gaps in our knowledge.

6.2 Hemolymph

In Chapters 3 and 4, I characterized the viscosity of hemolymph from *Manduca sexta* larvae. More specifically, I studied the relationship between hemolymph viscosity and temperature for this species. As temperature decreased, hemolymph viscosity increased, more so at temperatures below 22.7°C. However, when larvae were reared at cold temperatures, their hemolymph viscosity was lower at lower temperatures than warm- or room-reared larvae, suggesting some effect of thermal acclimation on hemolymph viscosity. Hemolymph viscosity and the effects of temperature are crucial in understanding the fluid mechanics of hemolymph flow within the hemocoel of the insect. The effect of environmental temperature on hemolymph viscosity could be an underappreciated factor in how insects use physiological mechanisms to cope with changes in temperature, including activity levels, defensive responses, and heart rate.

While the results in this dissertation provide a better understanding of the physical properties of hemolymph, they are limited to only a single insect species and development stage. Unfortunately, the methods used to measure viscosity in Chapters 3 and 4 require a minimum of 0.7 mL of hemolymph, which is significantly greater than the body volume of many insects. Measurement of hemolymph viscosity in the larvae of other large lepidopteran species would be possible and would provide comparison values for those measured here for hemolymph viscosity across temperatures. However, measuring the hemolymph viscosity in many other insect species and developmental stages, particularly those with smaller body size and/or hemolymph content, will require different methods. One promising candidate is magnetic rotational spectroscopy, which can measure viscosity in a much smaller volume of liquid [114]; however, this method has not yet been applied successfully to hemolymph. Initial attempts using this method with hemolymph of *Manduca sexta* larvae failed due to aggregation of hemocytes on the nanorod [170]. A different method requiring a smaller volume of hemolymph would be needed to answer further research questions, such as, how does hemolymph viscosity vary in pupae or adults? Does hemolymph viscosity of insects from different climates and temperature regimes have a different response to temperature?

In Chapter 4, I addressed the effects of thermal acclimation on hemolymph viscosity, finding that cold-reared insects had lower hemolymph viscosity at low temperatures than insects reared at warm and room temperatures. In an attempt to understand the mechanism behind this difference, I also measured hemocyte volume and other hemocyte properties, finding that cold-reared larvae have significantly larger hemocytes than both room- and warm-reared larvae. While larger hemocytes may affect viscosity, further experiments would be necessary to fully ascertain the effect of hemocyte size on hemolymph viscosity. Using a centrifuge, hemocytes could be isolated from the hemolymph of both cold- and room-reared larvae and re-suspended at a known cell volume in insect ringer's solution. Viscosity could then be measured following the protocol in Chapter 4, and differences could be attributed to the difference in hemocyte size. In addition, to fully understand the mechanism behind the difference in hemolymph viscosity, changes in the plasma composition due to rearing temperature would need further study. Measurement of protein and lipid content, as well as osmolality, in hemolymph from cold-, room-, and warm-reared larvae may vary, and thus affect viscosity.

The results of Chapter 3 represent the first measurement of insect hemolymph viscosity and how it varies with temperature. The results of Chapter 4 further describe how environmental temperature affects hemolymph viscosity in the context of thermal acclimation. Considering that flow of hemolymph within the circulatory system is dependent on the physical properties of hemolymph, these results provide necessary information to fully comprehend the structure and function of the insect circulatory system. Additionally, the effect of cold-acclimation on insect hemolymph viscosity represents another step towards understanding insect cold tolerance.

6.3 Dorsal vessel

In Chapter 5, I characterized the morphology and kinematics of the heart in *Zophobas morio* adults. Specifically, I used dissection and microtome sectioning to measure various morphological features of the heart, including the overall heart length and the length of each heart chamber. I also measured cross-sectional area and wall thickness down the length of the heart, identifying ostial valves in each heart chamber. I used infrared sensors and ultrasound measurements to quantify occlusion in the heart during pumping events as well as the speed of the contraction wave down the length of the heart. While morphology of the insect heart has been studied in other insect species [18-20, 158, 159, 165], this study is the first to also identify the kinematics of the heart wall. The geometry of the heart, especially during pumping, is critical to understand hemolymph flow production by the heart and throughout the circulatory system.

The measurements of heart morphology in Chapter 5 provide novel data for the heart of this beetle, but further measurements can be made to understand finer morphological details. Sections of the heart provided cross-sectional area and wall thickness through a portion (~45%) of the heart length. Further sectioning through the entire length of the heart, and repeated sectioning in additional animals would provide a more complete view of the heart in this species. In addition, although ostial valves were identified in each heart chamber, I only obtained two to three 1.5 μm thick sections of each valve. This does not show the full ostial valve structure, only a view of a small portion of the length of the valve. Additional sections through the entire length of the valves would allow for a full understanding of the structure of the ostial valves in this species, including the method of hemolymph inflow at these locations. Also, sectioning through the aorta

would provide the morphological characteristics of the entire dorsal vessel. Measurements of these additional morphological features would provide a full geometry of the dorsal vessel in this species.

Ultrasound views of the insect heart during pumping, as in used in Chapter 5, is a novel technique for viewing the heart motion throughout pumping events. This method is relatively easy, noninvasive, and provides information about the kinematics of the heart wall throughout the heartbeat, including contraction wave speed and percent conclusion. While these measurements in *Zophobas morio* adults in Chapter 5 are the first measured with this method, further measurements in additional insect species and developmental stages are warranted to fully understand heart wall kinematics across all insects. The only limitations of this technique are the resolution, especially for smaller species, and that the animal must be fully restrained with the dorsal surface unobstructed. Additionally, the effect of various treatments such as temperature, thermal acclimation, and disease on the contraction wave speed and percent occlusion could be measured with this technique. Heart rate is known to increase with increasing temperature [133, 147-149]; however, the effect of temperature on contraction speed and occlusion of the heart is still unknown. Hemolymph also plays a crucial role in insect immune response, with hemocytes aggregating at ostial valves after infection [171]. This aggregation may affect the kinematics of the heart wall throughout pumping, which could be viewed using ultrasound.

The results of Chapter 5 represent the first measurements of heart wall kinematics using longitudinal and transverse ultrasound. This is also the first study to characterize the morphology of the heart in the beetle *Zophobas morio*. Understanding how the heart wall moves will help us understand how it produces flow and ultimately, the full structure and function of the dorsal vessel and the circulatory system.

6.4 Circulatory model

Flow of hemolymph within the insect circulatory system is governed by both the geometry of the circulatory network and the physical properties of the hemolymph. This dissertation has made significant progress towards understanding and characterizing both of these factors. In Chapters 3 and 4, I measured the density and viscosity of insect hemolymph for the first time, including the effect of temperature on viscosity. In Chapter 5, I characterized the morphology and kinematics of the insect heart, including basic physiological measurements as well as the contraction wave speed and percent occlusion during pumping. Together these measurements can inform computational models of the insect heart, in an effort to fully simulate hemolymph flow within the heart. Numerical simulations of peristaltic tubular pumps have been created using various occlusion fractions, wave speeds, and sizes [161]. To create a model of the insect heart, we can include the parameters measured for the heart and hemolymph from Chapters 3, 4, and 5 to model hemolymph flow within the heart. The physiological relevance of this model could be improved by including observations of the heart chambers, including changes in cross-sectional area, wall thickness, and occlusion throughout each chamber during pumping. I found that the morphology of the insect heart is more complex than originally thought, as is the relationship between hemolymph viscosity and temperature. A numerical simulation could be used to measure the effect of changes in hemolymph viscosity and percent occlusion down the heart length on hemolymph flow within the heart. Modeling the peristaltic pumping of the heart will be valuable to fully understand the structure and function of the dorsal vessel and circulatory system as a whole.

References

[1] J. J. Socha and F. De Carlo, Use of synchrotron tomography to image naturalistic anatomy in insects, in *Developments in X-Ray Tomography VI*, 2008, vol. 7078, p. 70780A: International Society for Optics and Photonics.

[2] J. W. Andereck, J. G. King, and J. F. Hillyer, Contraction of the ventral abdomen potentiates extracardiac retrograde hemolymph propulsion in the mosquito hemocoel, *PLoS One*, vol. 5, no. 9, p. e12943, 2010.

[3] J. Kestin, M. Sokolov, and W. A. Wakeham, Viscosity of liquid water in the range −8 C to 150 C, *Journal of Physical and Chemical Reference Data*, vol. 7, no. 3, pp. 941-948, 1978.

[4] M. C. Kenny, M. N. Giarra, E. Granata, and J. J. Socha, How temperature influences the viscosity of hornworm hemolymph, *Journal of Experimental Biology*, p. jeb. 186338, 2018.

[5] G. P. Mead, N. A. Ratcliffe, and L. R. Renwrantz, The separation of insect haemocyte types on Percoll gradients; methodology and problems, *Journal of Insect Physiology*, vol. 32, no. 2, pp. 167-177, 1986.

[6] R. Chapman, A. Douglas, and M. Siva-Jothy, *The Insects: Structure and Function*. 2013, pp. 107-131.

[7] J. J. Socha, T. D. Förster, and K. J. Greenlee, Issues of convection in insect respiration: insights from synchrotron X-ray imaging and beyond, *Respiratory Physiology & Neurobiology*, vol. 173, pp. S65-S73, 2010.

[8] T. Weis-Fogh, Functional design of the tracheal system of flying insects as compared with the avian lung, *Journal of Experimental Biology*, vol. 41, no. 2, pp. 207-227, 1964.

[9] M. W. Westneat, O. Betz, R. W. Blob, K. Fezzaa, W. J. Cooper, and W.-K. Lee, Tracheal respiration in insects visualized with synchrotron X-ray imaging, *Science*, vol. 299, no. 5606, pp. 558-560, 2003.

[10] J. J. Socha, M. W. Westneat, J. F. Harrison, J. S. Waters, and W.-K. Lee, Real-time phase-contrast x-ray imaging: a new technique for the study of animal form and function, *BMC Biology*, vol. 5, no. 1, p. 6, 2007.

[11] A. Ghabrial, S. Luschnig, M. M. Metzstein, and M. A. Krasnow, Branching morphogenesis of the *Drosophila* tracheal system, *Annual Review of Cell and Developmental Biology,* vol. 19, no. 1, pp. 623-647, 2003.

[12] T. Hefnawy, Biochemical and physiological studies of certain ticks (Ixodoidea). Hemolymph volume determined by isotope and dye dilution during the gonotrophic cycle of *Argas (Persicargas) persicus* (Oken) and *A.(P.) arboreus* Kaiser, Hoogstraal, and Kohls (Argasidae), *The Journal of Parasitology,* pp. 358-364, 1972.

[13] T. Ichikawa, Mechanism of hemolymph circulation in the pupal leg of tenebrionid beetle *Zophobas atratus*, *Comparative Biochemistry and Physiology Part A: Molecular & Integrative Physiology,* vol. 153, no. 2, pp. 174-180, 2009.

[14] J. Woodcock, Physical properties of blood and their influence on blood-flow measurement, *Reports on Progress in Physics*, vol. 39, no. 1, p. 65, 1976.

[15] G. Pass, Accessory pulsatile organs: evolutionary innovations in insects, *Annual Review of Entomology,* vol. 45, no. 1, pp. 495-518, 2000.

[16] C. S. Wirkner, M. Tögel, and G. Pass, The arthropod circulatory system, in *Arthropod Biology and Evolution*: Springer, 2013, pp. 343-391.

[17] B. Baccetti and E. Bigliardi, Studies on the fine structure of the dorsal vessel of arthropods, *Cell and Tissue Research,* vol. 99, no. 1, pp. 13-24, 1969.

[18] R. G. Chiang, J. Chiang, and K. Davey, Morphology of the dorsal vessel in the abdomen of the blood-feeding insect *Rhodnius prolixus*, *Journal of Morphology,* vol. 204, no. 1, pp. 9-23, 1990.

[19] J. D. Glenn, J. G. King, and J. F. Hillyer, Structural mechanics of the mosquito heart and its function in bidirectional hemolymph transport, *Journal of Experimental Biology,* vol. 213, no. 4, pp. 541-550, 2010.

[20] G. P. League, O. C. Onuh, and J. F. Hillyer, Comparative structural and functional analysis of the larval and adult dorsal vessel and its role in hemolymph circulation in the mosquito *Anopheles gambiae*, *Journal of Experimental Biology,* vol. 218, no. 3, pp. 370-380, 2015.

[21] W.-K. Lee and J. J. Socha, Direct visualization of hemolymph flow in the heart of a grasshopper (*Schistocerca americana*), *BMC Physiology,* vol. 9, no. 1, p. 2, 2009.

[22] K. Sláma and J. Lukáš, Myogenic nature of insect heartbeat and intestinal peristalsis, revealed by neuromuscular paralysis caused by the sting of a braconid wasp, *Journal of Insect Physiology,* vol. 57, no. 2, pp. 251-259, 2011.

[23] L. Wasserthal, Interaction of circulation and tracheal ventilation in holometabolous insects, *Advances in Insect Physiology,* vol. 26, pp. 297-351, 1996.

[24] L. T. Wasserthal, Influence of periodic heartbeat reversal and abdominal movements on hemocoelic and tracheal pressure in resting blowflies *Calliphora vicina*, *Journal of Experimental Biology,* vol. 215, no. 2, pp. 362-373, 2012.

[25] D. Wharton, M. L. Wharton, and J. Lola, Blood volume and water content of the male American cockroach, *Periplaneta americana L.*—Methods and the influence of age and starvation, *Journal of Insect Physiology,* vol. 11, no. 4, pp. 391-404, 1965.

[26] R. Lee, The variation of blood volume with age in the desert locust (*Schistocerca gregaria Forsk.*), *Journal of Insect Physiology,* vol. 6, no. 1, pp. 36-51, 1961.

[27] T. Amin and J. Sirs, The blood rheology of man and various animal species, *Experimental Physiology,* vol. 70, no. 1, pp. 37-49, 1985.

[28] R. Brill and D. Jones, The influence of hematocrit, temperature and shear rate on the viscosity of blood from a high-energy-demand teleost, the yellowfin tuna *Thunnus albacares*, *Journal of Experimental Biology,* vol. 189, no. 1, pp. 199-212, 1994.

[29] J. Clarke and S. Nicol, Blood viscosity of the little penguin, *Eudyptula minor*, and the Adelie penguin, *Pygoscelis adeliae*: Effects of temperature and shear rate, *Physiological Zoology,* vol. 66, no. 5, pp. 720-731, 1993.

[30] K. D. Dunlap, Ontogeny and scaling of hematocrit and blood viscosity in western fence lizards, *Sceloporus occidentalis*, *BioOne,* vol. 2006, no. 3, pp. 535-538, 2006.

[31] J. Macdonald and R. Wells, Viscosity of body fluids from Antarctic notothenioid fish, in *Biology of Antarctic Fish*: Springer, 1991, pp. 163-178.

[32] N. M. Palenske and D. K. Saunders, Blood viscosity and hematology of American bullfrogs (*Rana catesbeiana*) at low temperature, *Journal of Thermal Biology,* vol. 28, no. 4, pp. 271-277, 2003.

[33] G. K. Snyder, Influence of temperature and hematocrit on blood viscosity, *American Journal of Physiology--Legacy Content,* vol. 220, no. 6, pp. 1667-1672, 1971.

[34] R. Wells and J. Baldwin, Oxygen transport potential in tropical reef fish with special reference to blood viscosity and haematocrit, *Journal of Experimental Marine Biology and Ecology,* vol. 141, no. 2-3, pp. 131-143, 1990.

[35] U. Windberger, A. Bartholovitsch, R. Plasenzotti, K. Korak, and G. Heinze, Whole blood viscosity, plasma viscosity and erythrocyte aggregation in nine mammalian species: reference values and comparison of data, *Experimental Physiology,* vol. 88, no. 3, pp. 431-440, 2003.

[36] W. Zhou, M. Fujita, and S. Yamamoto, Effects of ambient temperatures on blood viscosity and plasma protein concentration of broiler chickens (*Gallus domesticus*), *Journal of Thermal Biology,* vol. 24, no. 2, pp. 105-112, 1999.

[37] M. LaBarbera, Principles of design of fluid transport systems in zoology, *Science,* vol. 249, no. 4972, pp. 992-1000, 1990.

[38] K. A. McCulloh, J. S. Sperry, and F. R. Adler, Water transport in plants obeys Murray's law, *Nature,* vol. 421, no. 6926, pp. 939-942, 2003.

[39] T. F. Sherman, On connecting large vessels to small. The meaning of Murray's law., *The Journal of General Physiology,* vol. 78, no. 4, pp. 431-453, 1981.

[40] C. D. Murray, The physiological principle of minimum work applied to the angle of branching of arteries, *The Journal of General Physiology,* vol. 9, no. 6, p. 835, 1926.

[41] G. S. Kassab, Scaling laws of vascular trees: of form and function, *American Journal of Physiology-Heart and Circulatory Physiology,* 2006.

[42] H. Uylings, Optimization of diameters and bifurcation angles in lung and vascular tree structures, *Bulletin of Mathematical Biology,* vol. 39, no. 5, pp. 509-520, 1977.

[43] G. B. West, J. H. Brown, and B. J. Enquist, A general model for the origin of allometric scaling laws in biology, *Science,* vol. 276, no. 5309, pp. 122-126, 1997.

[44] X. Shan, M. Wang, and Z. Guo, Geometry optimization of self-similar transport network, *Mathematical Problems in Engineering,* vol. 2011, 2011.

[45] A. F. Miguel, Fluid flow in a porous tree-shaped network: optimal design and extension of Hess–Murray's law, *Physica A: Statistical Mechanics and Its Applications,* vol. 423, pp. 61-71, 2015.

[46] J. Sznitman, Respiratory microflows in the pulmonary acinus, *Journal of Biomechanics,* vol. 46, no. 2, pp. 284-298, 2013.

[47] D. Stephenson, A. Patronis, D. M. Holland, and D. A. Lockerby, Generalizing Murray's law: An optimization principle for fluidic networks of arbitrary shape and scale, *Journal of Applied Physics,* vol. 118, no. 17, p. 174302, 2015.

[48] L. Gosselin and A. K. da Silva, Constructal microchannel networks of rarefied gas with minimal flow resistance, *Journal of Applied Physics,* vol. 101, no. 11, p. 114902, 2007.

[49] M. Canny, The transpiration stream in the leaf apoplast: water and solutes, *Philosophical Transactions of the Royal Society of London B: Biological Sciences,* vol. 341, no. 1295, pp. 87-100, 1993.

[50] L. A. Taber, S. Ng, A. M. Quesnel, J. Whatman, and C. J. Carmen, Investigating Murray's law in the chick embryo, *Journal of Biomechanics,* vol. 34, no. 1, pp. 121-124, 2001.

[51] M. LaBarbera and G. E. Boyajian, The function of astrorhizae in stromatoporoids: quantitative tests, *Paleobiology,* vol. 17, no. 2, pp. 121-132, 1991.

[52] J. F. Harrison, Tracheal system, in *Encyclopedia of Insects*: Elsevier, 2009, pp. 1011-1015.

[53] M. R. Webster, J. J. Socha, L. Teresi, P. Nardinocchi, and R. De Vita, Structure of tracheae and the functional implications for collapse in the American cockroach, *Bioinspiration & Biomimetics,* vol. 10, no. 6, p. 066011, 2015.

[54] M. W. Westneat, J. J. Socha, and W.-K. Lee, Advances in biological structure, function, and physiology using synchrotron X-ray imaging, *Annual Review of Physiology,* vol. 70, pp. 119-142, 2008.

[55] O. Betz *et al.*, Imaging applications of synchrotron X-ray phase-contrast microtomography in biological morphology and biomaterials science. I. General aspects of the technique and its advantages in the analysis of millimetre-sized arthropod structure, *Journal of Microscopy,* vol. 227, no. 1, pp. 51-71, 2007.

[56] P. Cloetens, R. Barrett, J. Baruchel, J.-P. Guigay, and M. Schlenker, Phase objects in synchrotron radiation hard x-ray imaging, *Journal of Physics D: Applied Physics,* vol. 29, no. 1, p. 133, 1996.

[57] P. Cloetens *et al.*, Observation of microstructure and damage in materials by phase sensitive radiography and tomography, *Journal of Applied Physics,* vol. 81, no. 9, pp. 5878-5886, 1997.

[58] S. Ramanujan, *Ramanujan's collected works*. Chelsea, New York, 1962.

[59] J. J. Socha, W.-K. Lee, J. F. Harrison, J. S. Waters, K. Fezzaa, and M. W. Westneat, Correlated patterns of tracheal compression and convective gas exchange in a carabid beetle, *Journal of Experimental Biology,* vol. 211, no. 21, pp. 3409-3420, 2008.

[60] H. L. Contreras, E. C. Heinrich, and T. J. Bradley, Hypotheses regarding the discontinuous gas exchange cycle (DGC) of insects, *Current Opinion in Insect Science,* vol. 4, pp. 48-53, 2014.

[61] N. G. Schimpf, P. G. Matthews, R. S. Wilson, and C. R. White, Cockroaches breathe discontinuously to reduce respiratory water loss, *Journal of Experimental Biology,* vol. 212, no. 17, pp. 2773-2780, 2009.

[62] B. R. Helm and G. Davidowitz, Mass and volume growth of larval insect tracheal system within a single instar, *Journal of Experimental Biology,* p. jeb. 080648, 2013.

[63] J. Harrison, M. R. Frazier, J. R. Henry, A. Kaiser, C. Klok, and B. Rascón, Responses of terrestrial insects to hypoxia or hyperoxia, *Respiratory Physiology & Neurobiology,* vol. 154, no. 1-2, pp. 4-17, 2006.

[64] G. J. Beitel and M. A. Krasnow, Genetic control of epithelial tube size in the *Drosophila* tracheal system, *Development,* vol. 127, no. 15, pp. 3271-3282, 2000.

[65] V. Wigglesworth, Growth and regeneration in the tracheal system of an insect, *Rhodnius prolixus* (Hemiptera), *Journal of Cell Science,* vol. 3, no. 29, pp. 115-137, 1954.

[66] A. Schmitz and S. F. Perry, Stereological determination of tracheal volume and diffusing capacity of the tracheal walls in the stick insect *Carausius morosus* (Phasmatodea, Lonchodidae), *Physiological and Biochemical Zoology,* vol. 72, no. 2, pp. 205-218, 1999.

[67] C. Noirot and C. Noirot-Timothée, The structure and development of the tracheal system, in *Insect Ultrastructure*: Springer, 1982, pp. 351-381.

[68] A. Kaiser, C. J. Klok, J. J. Socha, W.-K. Lee, M. C. Quinlan, and J. F. Harrison, Increase in tracheal investment with beetle size supports hypothesis of oxygen limitation on insect gigantism, *Proceedings of the National Academy of Sciences,* vol. 104, no. 32, pp. 13198-13203, 2007.

[69] A. Krogh, Studien über Tracheenrespiration III. Die Kombination von mechanischer Ventilation mit Gasdiffusion nach Versuchen an Dytiscus-Larven, *Pflügers Arch,* vol. 179, pp. 113-120, 1920.

[70] P. L. Miller, The supply of oxygen to the active flight muscles of some large beetles, *Journal of Experimental Biology*, vol. 45, no. 2, pp. 285-304, 1966.

[71] J. R. Lighton, *Measuring metabolic rates: a manual for scientists*. Oxford University Press, 2018.

[72] K. Sláma, A new look at insect respiration, *The Biological Bulletin*, vol. 175, no. 2, pp. 289-300, 1988.

[73] J. Lighton and D. Garrigan, Ant breathing: testing regulation and mechanism hypotheses with hypoxia, *Journal of Experimental Biology*, vol. 198, no. 7, pp. 1613-1620, 1995.

[74] J. S. Terblanche, E. Marais, S. K. Hetz, and S. L. Chown, Control of discontinuous gas exchange in *Samia cynthia*: effects of atmospheric oxygen, carbon dioxide and moisture, *Journal of Experimental Biology*, vol. 211, no. 20, pp. 3272-3280, 2008.

[75] K. Sláma, Extracardiac haemocoelic pulsations and the autonomic neuroendocrine system (coelopulse) of terrestrial insects, *Terrestrial Arthropod Reviews*, vol. 1, no. 1, pp. 39-80, 2008.

[76] X. Zheng *et al.*, Bio-inspired Murray materials for mass transfer and activity, *Nature Communications*, vol. 8, p. 14921, 2017.

[77] S. Vogel, *Vital Circuits: On Pumps, Pipes, and the Workings of Circulatory Systems*. Oxford University Press on Demand, 1993.

[78] S. Vogel, *Life in Moving Fluids: The Physical Biology of Flow*. Princeton University Press, 1996.

[79] R. Wells, L. Beard, and G. C. Grigg, Blood viscosity and hematocrit in the estuarine crocodile, *Crocodylus porosus*, *Comparative Biochemistry and Physiology Part A: Physiology*, vol. 99, no. 3, pp. 411-414, 1991.

[80] G. K. Snyder, Blood viscosity in annelids, *Journal of Experimental Zoology Part A: Ecological Genetics and Physiology*, vol. 206, no. 2, pp. 271-277, 1978.

[81] M. A. Gertz and R. A. Kyle, Hyperviscosity syndrome, *Journal of Intensive Care Medicine*, vol. 10, no. 3, pp. 128-141, 1995.

[82] D. M. Eckmann, S. Bowers, M. Stecker, and A. T. Cheung, Hematocrit, volume expander, temperature, and shear rate effects on blood viscosity, *Anesthesia & Analgesia*, vol. 91, no. 3, pp. 539-545, 2000.

[83] J. A. Dormandy, Influence of blood viscosity on blood flow and the effect of low molecular weight dextran, *British Medical Journal*, vol. 4, no. 5789, pp. 716-719, 1971.

[84] V. Dulceata, Thermoregulation–temperature homeostasis, *Marathon*, vol. 6, no. 2, pp. 150-153, 2014.

[85] T. M. Casey, Activity patterns, body temperature and thermal ecology in two desert caterpillars (Lepidoptera: Sphingidae), *Ecology*, vol. 57, no. 3, pp. 485-497, 1976.

[86] K. Mellanby, Low temperature and insect activity, *Proceedings of the Royal Society of London. Series B, Biological Sciences*, pp. 473-487, 1939.

[87] A. A. Guarneri, C. Lazzari, A. A. P. Xavier, L. Diotaiuti, and M. G. Lorenzo, The effect of temperature on the behaviour and development of *Triatoma brasiliensis*, *Physiological Entomology*, vol. 28, no. 3, pp. 185-191, 2003.

[88] L. Taylor, Analysis of the effect of temperature on insects in flight, *The Journal of Animal Ecology*, pp. 99-117, 1963.

[89] J. Sueur and A. F. Sanborn, Ambient temperature and sound power of cicada calling songs (*Hemiptera: Cicadidae: Tibicina*), *Physiological Entomology*, vol. 28, no. 4, pp. 340-343, 2003.

[90] M. Katsuki and T. Miyatake, Effects of temperature on mating duration, sperm transfer and remating frequency in *Callosobruchus chinensis*, *Journal of Insect Physiology*, vol. 55, no. 2, pp. 113-116, 2009.

[91] P.-C. Wickman, The influence of temperature on the territorial and mate locating behaviour of the small heath butterfly, *Coenonympha pamphilus (L.)(Lepidoptera: Satyridae)*, *Behavioral Ecology and Sociobiology*, vol. 16, no. 3, pp. 233-238, 1985.

[92] J. Overgaard and H. A. MacMillan, The integrative physiology of insect chill tolerance, *Annual Review of Physiology*, vol. 79, pp. 187-208, 2017.

[93] S. Ragland and R. Sohal, Ambient temperature, physical activity and aging in the housefly, *Musca domestica*, *Experimental Gerontology*, vol. 10, no. 5, pp. 279-289, 1975.

[94] J. C. Jones, The circulatory system of insects, in *The Physiology of Insecta*, vol. 3, M. Rockstein, Ed.: Academic Press, 1964, pp. 1-107.

[95] O. Reynolds, IV. On the theory of lubrication and its application to Mr. Beauchamp tower's experiments, including an experimental determination of the viscosity of olive oil, *Philosophical Transactions of the Royal Society of London*, vol. 177, pp. 157-234, 1886.

[96] V. M. Muggeo, Segmented: an R package to fit regression models with broken-line relationships, *R News*, vol. 8, no. 1, pp. 20-25, 2008.

[97] G. S. Kell, Density, thermal expansivity, and compressibility of liquid water from 0. deg. to 150. deg.. correlations and tables for atmospheric pressure and saturation reviewed and expressed on 1968 temperature scale, *Journal of Chemical and Engineering Data*, vol. 20, no. 1, pp. 97-105, 1975.

[98] C. L. Guard and D. E. Murrish, Effects of temperature on the viscous behavior of blood from antarctic birds and mammals, *Comparative Biochemistry and Physiology Part A: Physiology*, vol. 52, no. 2, pp. 287-290, 1975.

[99] N. M. Palenske and D. K. Saunders, Comparisons of blood viscosity between amphibians and mammals at 3 C and 38 C, *Journal of Thermal Biology*, vol. 27, no. 6, pp. 479-484, 2002.

[100] F.-J. Neumann, H. Schmid-Schönbein, and H. Ohlenbusch, Temperature-dependence of red cell aggregation, *Pflügers Archiv European Journal of Physiology*, vol. 408, no. 5, pp. 524-530, 1987.

[101] S. Chien, S. Usami, R. J. Dellenback, M. I. Gregersen, L. B. Nanninga, and M. M. Guest, Blood viscosity: influence of erythrocyte aggregation, *Science,* vol. 157, no. 3790, pp. 829-831, 1967.

[102] M. A. Lichtman and E. Kearney, Cellular deformability during maturation of the myeloblast: Possible role in marrow egress, *New England Journal of Medicine,* vol. 283, no. 18, pp. 943-948, 1970.

[103] N. O. Petersen, W. B. McConnaughey, and E. L. Elson, Dependence of locally measured cellular deformability on position on the cell, temperature, and cytochalasin B, *Proceedings of the National Academy of Sciences,* vol. 79, no. 17, pp. 5327-5331, 1982.

[104] M. E. Clark and J. C. Jones, Hematocrit method for determining total hemocyte counts of larvae of the tobacco budworm, *Heliothis virescens* (Lepidoptera: Noctuidae), *Annals of the Entomological Society of America,* vol. 73, no. 6, pp. 683-685, 1980.

[105] M. Brust *et al.*, Rheology of human blood plasma: Viscoelastic versus Newtonian behavior, *Physical Review Letters,* vol. 110, no. 7, p. 078305, 2013.

[106] M. F. McMullin *et al.*, Guidelines for the diagnosis, investigation and management of polycythaemia/erythrocytosis, *British Journal of Haematology,* vol. 130, no. 2, pp. 174-195, 2005.

[107] J. G. Sørensen, T. N. Kristensen, and V. Loeschcke, The evolutionary and ecological role of heat shock proteins, *Ecology Letters,* vol. 6, no. 11, pp. 1025-1037, 2003.

[108] W. J. Gehring and R. Wehner, Heat shock protein synthesis and thermotolerance in *Cataglyphis*, an ant from the Sahara desert, *Proceedings of the National Academy of Sciences,* vol. 92, no. 7, pp. 2994-2998, 1995.

[109] J. Dahlgaard, V. Loeschcke, P. Michalak, and J. Justesen, Induced thermotolerance and associated expression of the heat-shock protein Hsp70 in adult *Drosophila melanogaster*, *Functional Ecology,* vol. 12, no. 5, pp. 786-793, 1998.

[110] B. J. Sinclair, P. Vernon, C. J. Klok, and S. L. Chown, Insects at low temperatures: an ecological perspective, *Trends in Ecology & Evolution,* vol. 18, no. 5, pp. 257-262, 2003.

[111] M. Holmstrup, M. Bayley, and H. Ramløv, Supercool or dehydrate? An experimental analysis of overwintering strategies in small permeable arctic invertebrates, *Proceedings of the National Academy of Sciences,* vol. 99, no. 8, pp. 5716-5720, 2002.

[112] K. E. Zachariassen, Physiology of cold tolerance in insects, *Physiological Reviews,* vol. 65, no. 4, pp. 799-832, 1985.

[113] S. Beetz, T. K. Holthusen, J. Koolman, and T. Trenczek, Correlation of hemocyte counts with different developmental parameters during the last larval instar of the tobacco hornworm, *Manduca sexta*, *Archives of Insect Biochemistry and Physiology*, vol. 67, no. 2, pp. 63-75, 2008.

[114] A. Tokarev, B. Kaufman, Y. Gu, T. Andrukh, P. H. Adler, and K. G. Kornev, Probing viscosity of nanoliter droplets of butterfly saliva by magnetic rotational spectroscopy, *Applied Physics Letters*, vol. 102, no. 3, p. 033701, 2013.

[115] S. L. Chown and S. Nicolson, *Insect physiological ecology: mechanisms and patterns*. Oxford University Press, 2004.

[116] J. F. Harrison, H. A. Woods, and S. P. Roberts, *Ecological and environmental physiology of insects*. Oxford University Press, 2012.

[117] F. Goller and H. Esch, Comparative study of chill-coma temperatures and muscle potentials in insect flight muscles, *Journal of Experimental Biology*, vol. 150, no. 1, pp. 221-231, 1990.

[118] A. Neville and T. Weis-Fogh, The effect of temperature on locust flight muscle, *Journal of Experimental Biology*, vol. 40, no. 1, pp. 111-121, 1963.

[119] D. L. Denlinger and R. E. Lee Jr, *Low temperature biology of insects*. Cambridge University Press, 2010.

[120] N. M. Teets and D. L. Denlinger, Physiological mechanisms of seasonal and rapid cold-hardening in insects, *Physiological Entomology*, vol. 38, no. 2, pp. 105-116, 2013.

[121] H. A. MacMillan *et al.*, Cold acclimation wholly reorganizes the *Drosophila melanogaster* transcriptome and metabolome, *Scientific Reports*, vol. 6, p. 28999, 2016.

[122] L. G. Neven, Physiological responses of insects to heat, *Postharvest Biology and Technology*, vol. 21, no. 1, pp. 103-111, 2000.

[123] H. C. Kwaan, Role of plasma proteins in whole blood viscosity: a brief clinical review, *Clinical Hemorheology and Microcirculation*, vol. 44, no. 3, pp. 167-176, 2010.

[124] K. E. Zachariassen, Seasonal variation in hemolymph osmolality and osmotic contribution of glycerol in adult *Rhagium inquisitor L.*(Col., Cerambycidae), *Norwegian Journal of Entomology*, vol. 20, no. 2, pp. 259-262, 1973.

[125] S. Bardoloi and L. K. Hazarika, Seasonal variations of body weight, lipid reserves, blood volumes, and hemocyte population of *Antheraea assama* (Lepidoptera: Satumiidae), *Environmental Entomology*, vol. 21, no. 6, pp. 1398-1403, 1992.

[126] J. C. Jones, Current concepts concerning insect hemocytes, *American Zoologist*, pp. 209-246, 1962.

[127] J. Kurtz, A. Wiesner, P. Götz, and K. P. Sauer, Gender differences and individual variation in the immune system of the scorpionfly *Panorpa vulgaris* (Insecta: Mecoptera), *Developmental & Comparative Immunology*, vol. 24, no. 1, pp. 1-12, 2000.

[128] C. M. Fittinghoff and L. M. Riddiford, Heat sensitivity and protein synthesis during heat-shock in the tobacco hornworm, *Manduca sexta*, *Journal of Comparative Physiology B*, vol. 160, no. 4, pp. 349-356, 1990.

[129] J. G. Kingsolver, H. J. MacLean, S. B. Goddin, and K. E. Augustine, Plasticity of upper thermal limits to acute and chronic temperature variation in *Manduca sexta* larvae, *Journal of Experimental Biology*, vol. 219, no. 9, pp. 1290-1294, 2016.

[130] H. Colinet, B. J. Sinclair, P. Vernon, and D. Renault, Insects in fluctuating thermal environments, *Annual Review of Entomology*, vol. 60, 2015.

[131] E. J. Kim, W. J. Rhee, and T. H. Park, Isolation and characterization of an apoptosis-inhibiting component from the hemolymph of *Bombyx mori*, *Biochemical and Biophysical Research Communications*, vol. 285, no. 2, pp. 224-228, 2001.

[132] E. Walters, P. Illich, J. Weeks, and M. Lewin, Defensive responses of larval *Manduca sexta* and their sensitization by noxious stimuli in the laboratory and field, *Journal of Experimental Biology*, vol. 204, no. 3, pp. 457-469, 2001.

[133] J. C. Jones, Factors affecting heart rates in insects, *The Physiology of Insecta*, vol. 4, pp. 119-167, 1974.

[134] E. Steinhaus, *Insect Pathology V1: An Advanced Treatise*. Elsevier, 2012.

[135] G. Wilson and S. Sohi, Effect of temperature on healthy and microsporidia-infected continuous cultures of *Malacosoma disstria* hemocytes, *Canadian Journal of Zoology*, vol. 55, no. 4, pp. 713-717, 1977.

[136] D. M. Enerson, Cellular swelling. I. Hypothermia graded hypoxia, and the osmotic effects of low molecular weight dextran on isolated tissues, *Annals of Surgery*, vol. 163, no. 2, p. 169, 1966.

[137] D. C. Marsh, S. L. Lindell, L. E. Fox, F. O. Belzer, and J. H. Southard, Hypothermic preservation of hepatocytes: I. Role of cell swelling, *Cryobiology*, vol. 26, no. 6, pp. 524-534, 1989.

[138] H. Petrowsky and P.-A. Clavien, Principles of Liver Preservation, in *Transplantation of the Liver*, R. W. Busuttil and G. B. G. Klintmalm, Eds. 3rd ed., 2015, pp. 582-599.

[139] H. A. MacMillan, J. L. Andersen, V. Loeschcke, and J. Overgaard, Sodium distribution predicts the chill tolerance of *Drosophila melanogaster* raised in different thermal conditions, *American Journal of Physiology-Regulatory, Integrative and Comparative Physiology*, vol. 308, no. 10, pp. R823-R831, 2015.

[140] J. Crowley, J. Metzger, E. Merrill, and C. Valeri, Whole blood viscosity in beta thalassemia minor, *Annals of Clinical & Laboratory Science*, vol. 22, no. 4, pp. 229-235, 1992.

[141] H. Stone, H. Thompson Jr, and K. Schmidt-Nielsen, Influence of erythrocytes on blood viscosity, *American Journal of Physiology-Legacy Content*, vol. 214, no. 4, pp. 913-918, 1968.

[142] J. Duman and K. Horwath, The role of hemolymph proteins in the cold tolerance of insects, *Annual Review of Physiology*, vol. 45, no. 1, pp. 261-270, 1983.

[143] N. Li, Relationships between cold hardiness, and ice nucleating activity, glycerol and protein contents in the hemolymph of caterpillars, *Aporia crataegi L*, *CryoLetters*, vol. 33, no. 2, pp. 134-142, 2012.

[144] L. Sømme, The effect of temperature, anoxia, or injection of various substances on haemolymph composition and supercooling in larvae of *Anagasta kuehniella* (Zell.), *Journal of Insect Physiology*, vol. 12, no. 9, pp. 1069-1083, 1966.

[145] A. H. Seplowitz, S. Chien, and F. R. Smith, Effects of lipoproteins on plasma viscosity, *Atherosclerosis*, vol. 38, no. 1-2, pp. 89-95, 1981.

[146] H. Meiselman, E. Merrill, E. Gilliland, G. Pelletier, and E. Salzman, Influence of plasma osmolarity on the rheology of human blood, *Journal of Applied Physiology,* vol. 22, no. 4, pp. 772-781, 1967.

[147] G. A. Edwards and W. L. Nutting, The influence of temperature upon the respiration and heart activity of *Thermobia* and *Grylloblatta*, *Psyche,* vol. 57, no. 2, pp. 33-44, 1950.

[148] L. A. White, J. M. Ringo, and H. B. Dowse, Effects of deuterium oxide and temperature on heart rate in *Drosophila melanogaster*, *Journal of Comparative Physiology B,* vol. 162, no. 3, pp. 278-283, 1992.

[149] T. Jennings, J. Ringo, and H. Dowse, The relationship of heart function to temperature in *Drosophila melanogaster* and its heritability, *Journal of Experimental Zoology Part A: Ecological Genetics and Physiology,* vol. 311, no. 9, pp. 689-696, 2009.

[150] J. F. Hillyer, Insect heart rhythmicity is modulated by evolutionarily conserved neuropeptides and neurotransmitters, *Current Opinion in Insect Science,* 2018.

[151] K. Y. Lagerspetz, Temperature acclimation and the nervous system, *Biological Reviews,* vol. 49, no. 4, pp. 477-514, 1974.

[152] B. A. Trimmer, A. E. Takesian, B. M. Sweet, C. B. Rogers, D. C. Hake, and D. J. Rogers, Caterpillar locomotion: a new model for soft-bodied climbing and burrowing robots, in *7th International Symposium on Technology and the Mine Problem*, 2006, vol. 1, pp. 1-10: Monterey, CA: Mine Warfare Association.

[153] L. Van Griethuijsen and B. Trimmer, Locomotion in caterpillars, *Biological Reviews,* vol. 89, no. 3, pp. 656-670, 2014.

[154] S. Mezoff, N. Papastathis, A. Takesian, and B. A. Trimmer, The biomechanical and neural control of hydrostatic limb movements in *Manduca sexta*, *Journal of Experimental Biology,* vol. 207, no. 17, pp. 3043-3053, 2004.

[155] J. Sun, M. Ling, W. Wu, B. Bhushan, and J. Tong, The hydraulic mechanism of the unfolding of hind wings in *Dorcus titanus platymelus* (order: Coleoptera), *International Journal of Molecular Sciences,* vol. 15, no. 4, pp. 6009-6018, 2014.

[156] J. Sun, W. Wu, M. Ling, B. Bhushan, and J. Tong, The hydraulic mechanism in the hind wing veins of *Cybister japonicus* Sharp (order: Coleoptera), *Beilstein Journal of Nanotechnology,* vol. 7, no. 1, pp. 904-913, 2016.

[157] G. Pass, B.-A. Gereben-Krenn, M. Merl, J. Plant, N. U. Szucsich, and M. Tögel, Phylogenetic relationships of the orders of Hexapoda: contributions from the circulatory organs for a morphological data matrix, *Arthropod Syst. Phylogeny,* vol. 64, pp. 165-203, 2006.

[158] B. Rotstein and A. Paululat, On the morphology of the *Drosophila* heart, *Journal of Cardiovascular Development and Disease,* vol. 3, no. 2, p. 15, 2016.

[159] T. Markou and G. Theophilidis, The pacemaker activity generating the intrinsic myogenic contraction of the dorsal vessel of *Tenebrio molitor* (Coleoptera), *Journal of Experimental Biology,* vol. 203, no. 22, pp. 3471-3483, 2000.

[160] K. Sláma, Mechanical aspects of heartbeat reversal in pupae of *Manduca sexta*, *Journal of Insect Physiology*, vol. 49, no. 7, pp. 645-657, 2003.

[161] L. Waldrop and L. Miller, Large-amplitude, short-wave peristalsis and its implications for transport, *Biomechanics and Modeling in Mechanobiology*, vol. 15, no. 3, pp. 629-642, 2016.

[162] M. Li and J. G. Brasseur, Non-steady peristaltic transport in finite-length tubes, *Journal of Fluid Mechanics*, vol. 248, pp. 129-151, 1993.

[163] G. G. Scudder, The importance of insects, *Insect Biodiversity: Science and Society*, vol. 1, p. 9, 2017.

[164] C. A. Schneider, W. S. Rasband, and K. W. Eliceiri, NIH Image to ImageJ: 25 years of image analysis, *Nature Methods*, vol. 9, no. 7, p. 671, 2012.

[165] N. Curtis, J. Ringo, and H. Dowse, Morphology of the pupal heart, adult heart, and associated tissues in the fruit fly, *Drosophila melanogaster*, *Journal of Morphology*, vol. 240, no. 3, pp. 225-235, 1999.

[166] S. Childress, *An introduction to theoretical fluid mechanics*. American Mathematical Soc., 2009.

[167] K. Slama and T. A. Miller, Physiology of heartbeat reversal in diapausing pupae of the tobacco hornworm, *Manduca sexta* (Lepidoptera: Sphingidae), *European Journal of Entomology*, vol. 98, no. 4, pp. 415-432, 2001.

[168] C. Loudon, Tracheal hypertrophy in mealworms: design and plasticity in oxygen supply systems, *Journal of Experimental Biology*, vol. 147, no. 1, pp. 217-235, 1989.

[169] M. Raś, D. Iwan, and M. J. Kamiński, The tracheal system in post-embryonic development of holometabolous insects: a case study using the mealworm beetle, *Journal of Anatomy*, vol. 232, no. 6, pp. 997-1015, 2018.

[170] P. Aprelev, M. Kenny, J. Socha, and K. Kornev, Rheological behavior of insect hemolymph on macro-, micro-, and nano-scales, in *Integrative and Comparative Biology*, 2017, vol. 57, pp. E193-E193: Oxford Univ Press Inc Journals Dept, 2001 Evans Rd, Cary, NC 27513 USA.

[171] J. F. Hillyer and M. R. Strand, Mosquito hemocyte-mediated immune responses, *Current Opinion in Insect Science*, vol. 3, pp. 14-21, 2014.

Appendices

Appendix A

Chapter 2 supporting information

A.1 Code repository

https://github.com/TheSochaLab/Does-Murray-s-law-apply-to-the-tracheal-sytem-in-insects--A-3D-study-of-the-beetle-Platynus-decentis

A.2 Supplemental materials

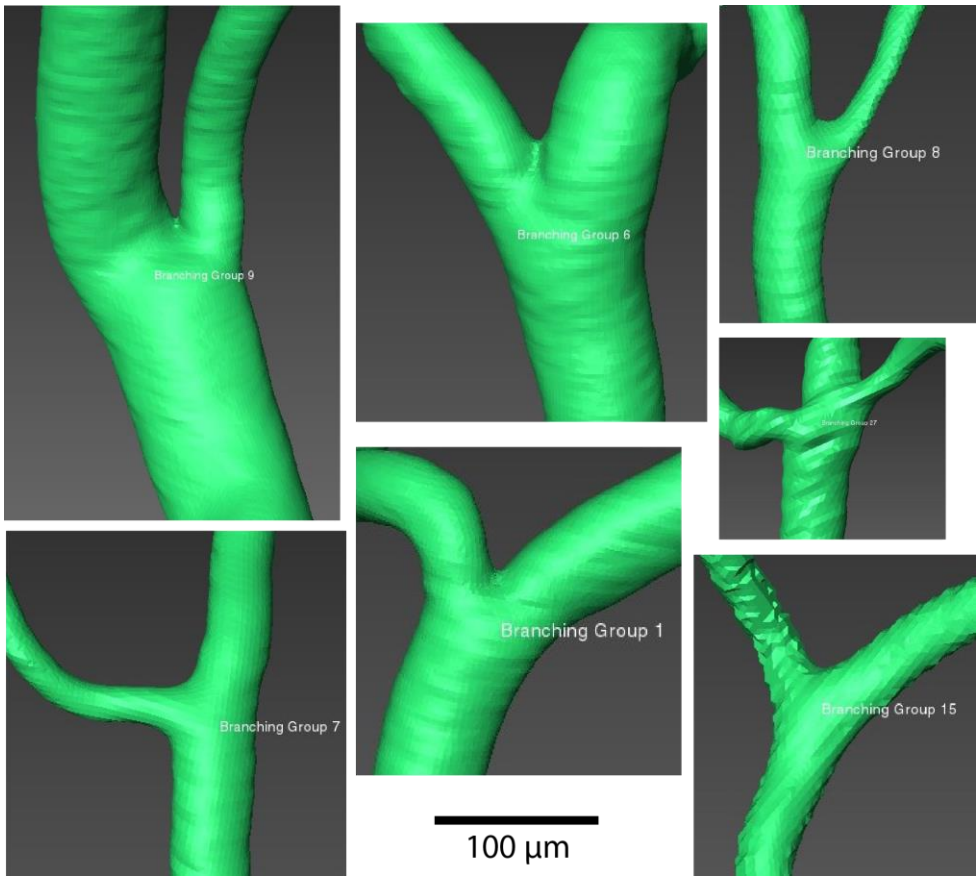

Figure A.2.1: Sampling of several tracheal branching groups from a single animal showing variation in size, angle, shape, and number of daughter tubes.

A.3 Avizo protocol

A Guide to Segmentation Using Avizo 8.1 (2nd edition)

Melissa Kenny (mck66@vt.edu) and Brittany Horton (hortonb@vt.edu)

Virginia Tech, Socha Lab

(1st edition authors: Elizabeth Lee, John Sheppard, Stephen Robinson, Jake Socha)

Table of Contents:

I. Getting Started

Start out by completing some basic tutorials offered in the Avizo User's Guide (Figure 1):

- Under the Help menu, select User's Guide
- Select Tutorials
- Work through the following:
    - Getting started – the basics of Avizo*
    - Reading images – how to read images
    - Visualizing 3D images – slices, isosurfaces, volume rendering
    - Image segmentation – segmentation of 3D image data
    - Surface reconstruction – surface reconstruction from 3D images

* *This tutorial is incredibly important to this protocol and highly recommended before continuing.*

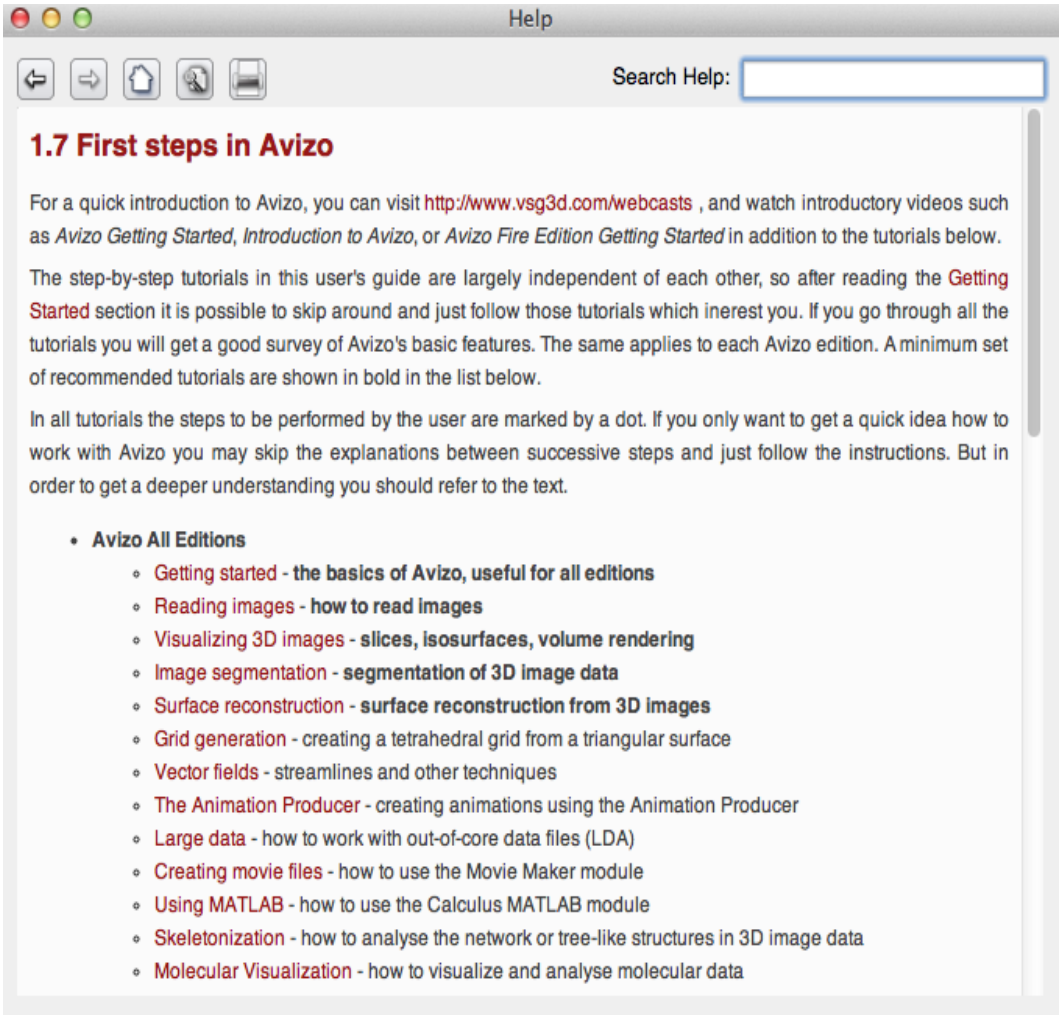

Figure A.3.1: A list of the Avizo tutorial options in the User's Guide. The first option, entitled "Getting started" is necessary to continue with this protocol.

II. Preparing Your Images

1) All the image files should be .tiff (tagged image file) in order to accurately represent the content.
   a) Use ImageJ to convert images from .hdf to .tiff if needed
      i) Create a folder on your computer containing the .hdf files
      ii) Create a different folder where the .tiff files will be stored
      iii) Open ImageJ (if you do not have this program, download it for free at http://imagej.nih.gov/ij/download.html)
      iv) In Image J, click Plugins → Macro → Run → "BatchConvert_hdf-to-tiff"
      (Note: If you use ImageJ 1.43 or later, simply go to Process → Batch → Convert)
      v) Fill in the pop up window appropriately as shown in Figure 2

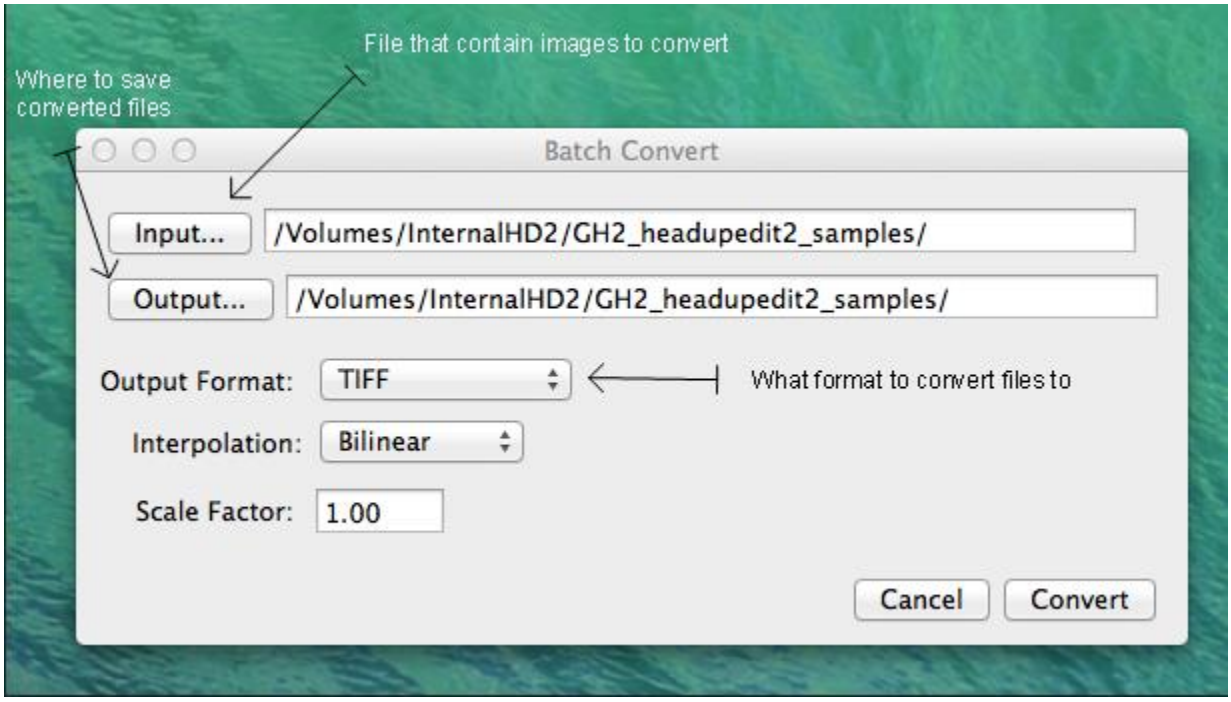

Figure A.3.2: ImageJ pop-up window to convert hdf images to tiff.

2) Images can be cropped so that only the relevant data is shown, however, in order to create a 3D view of the data in Avizo, every slice must be cropped in the same location by cropping them as a stack as follows (in ImageJ):
   a) First, load the images from an uncompressed file (File → import → raw)
   b) Select an area to crop to on all images by using the plugin "Plugin → stacks → crop (3D)"
   c) Check throughout the image sequence to make sure the specimen isn't clipped in any slice
   d) When you are satisfied with the amount of down sampling, select "image" and then "crop"

III. Loading Data for Segmentation

1. Open Avizo 8.1
   Note: In the Socha lab, there are at least 3 copies of Avizo. The Windows computer has Avizo 6.3 which is usable but is not the newest version and files in this will not always load correctly (or at all) in a newer version. On the Mac, there is 8.1 and 9.0. 9.0 is not yet fully functioning so this protocol uses 8.1 for all of its explanations.

2. If you are using Avizo version 6.3* ONLY: Once open, there will be a console window on the bottom of the screen. This is the window that code can be typed into. Type "app maxmalloc" and hit enter.
   a) App maxmallock tells Avizo to allocate the maximum amount of available memory in a series of continuous chunks. Inputting this in the command prompt before loading large data sets or any major operations may help conserve memory.

**In 8.1 and later, Avizo runs this automatically. However, in 6.3 the application typically allows 2GB of memory so if you try to load more than this the application is unable to function. This is unnecessary in 8.1 and later and attempting to run it will actually crash the program.*

3. Click on "File" then "open data"
   a) Highlight all of the .tiff image files that you would like to open
   b) Click "load"

4. If multiple images were selected, an alert box may pop up (Figure 3)

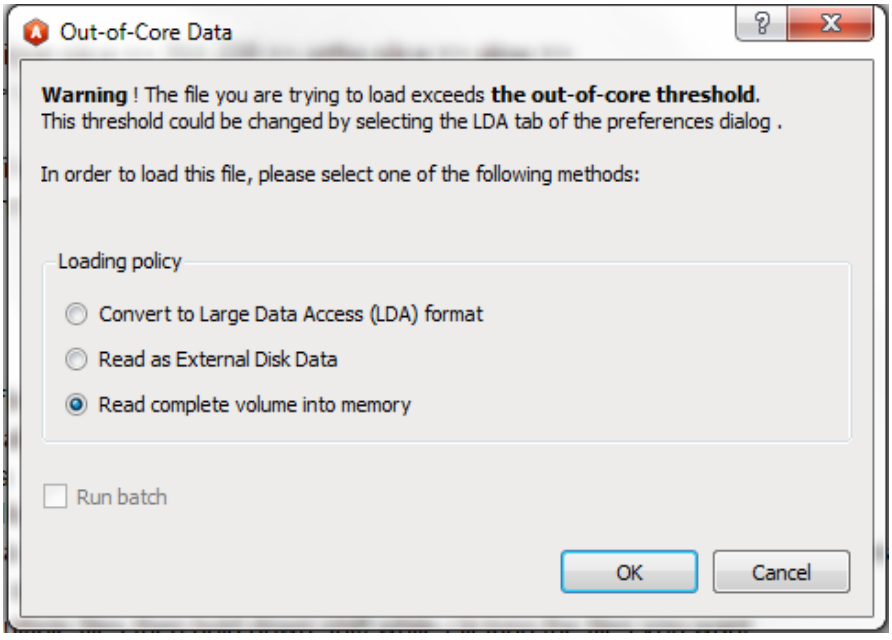

Figure A.3.3: Alert Box "Out-of-Core Data"

a) Select “Read complete volume into memory” and then OK
Note: Selecting any other methods will prevent Avizo from creating labelfields, which become important later on in order to accomplish segmentation. This is likely because of memory limitations and the power required for segmentation.
b) Your voxel size should be set to 1x1x1 unless you have resized the data before loading
c) Click “OK”

5. Now that you have the data loaded, you should see the file name within a 3D green button in the Main Panel (Figure 4). These ‘buttons’ are called modules, and this would be the raw data module.

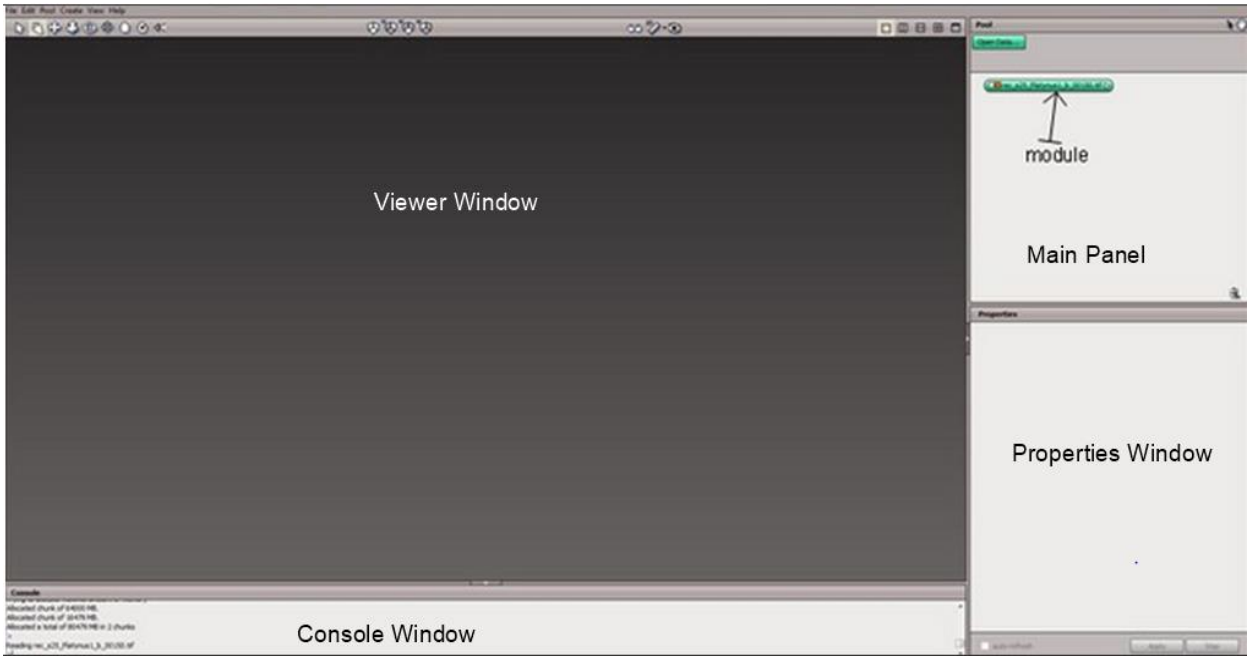

Figure A.3.4: Avizo screen after successfully opening the data.

IV. Modules

It is important to note that the colored ellipses that show up in the main panel of the Avizo screen are called modules. If you click on the module, properties will show in the properties window. Right clicking on the module will expose a drop down menu of visualization or computation options. Modules can be linked based on their source and through different parameters, such as for visualization or generation of a surface. In each module, there is an orange square to the left of the module name. Clicking on this square hides or exposes the contents of the module in the Viewer Window.

V. Ways to Visualize the Data Set

a. Ortho Slice

The most typical visual representation of the data is viewing the data as orthogonal slices or essentially, viewing the original .tif images that were loaded and being able to scroll through them in the 3D plane. If you are doing segmentation, this is the view you should start with.

To generate an Ortho Slice module,

1. Click on the raw image module
2. Right click (Ctrl+click on Mac) on the module and a menu will appear (Figure 5)
    a. Display → Ortho Slice → Create
    b. This creates a new module named "Ortho Slice" that is connected to the raw data module

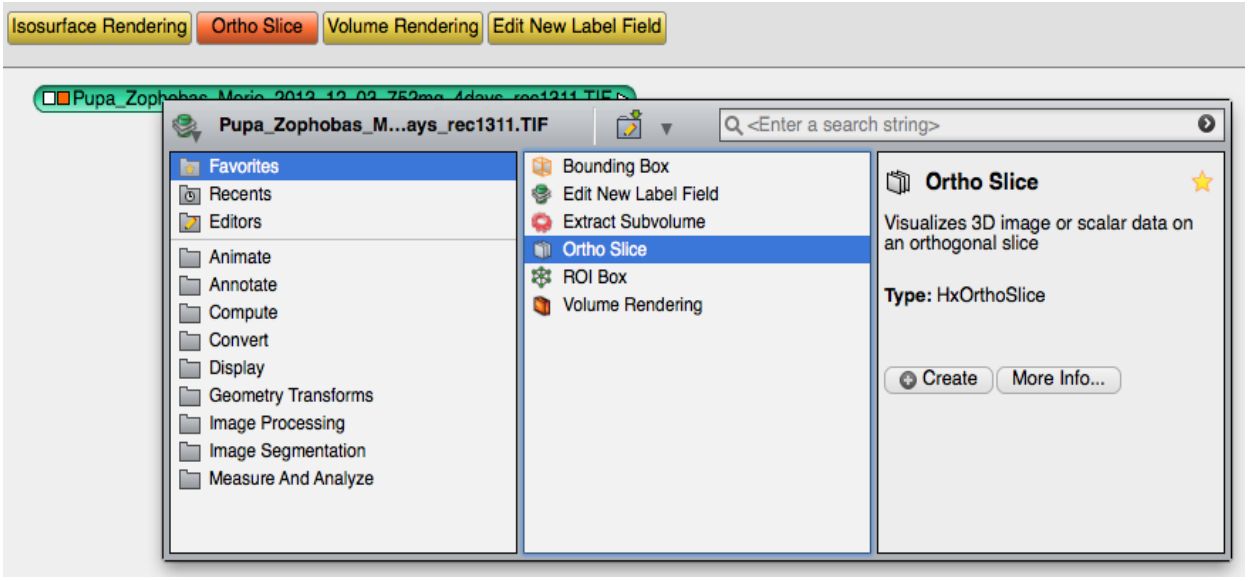

Figure A.3.5: Menu to generate Ortho Slice. If it does not show up in "Favorites", it is in the "Display" folder.

Clicking on the Ortho Slice module displays several options that can be changed that are shown in the properties window (Figure 6):

1. "Data:" shows the source data. If you change to a different raw image module in the dropdown menu, it will generate an Ortho Slice for that set of images
2. "Orientation:" allows you to view the xy, xz, and yz slices of the 3D data
3. "Slice Number:" controls which slice is shown in the viewer window and allows the viewer to scroll through the images or slices. This can also be changed by clicking the regular cursor option (right) at the top left and clicking on the slice and dragging up or down

4. The remaining options are not necessary for this protocol but more information can be found in Avizo help

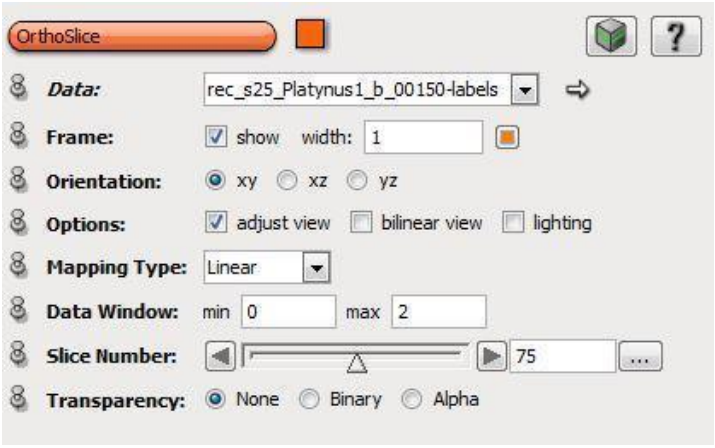

Figure A.3.6: Properties Window of OrthoSlice

b. **Slice**

Similar to the Ortho Slice, but instead of being perpendicular to the slice plane, the simple 'slice' can be rotated to view slices in different orientations throughout the 3D volume.

To generate a Slice module (termed Oblique Slice in older versions of Avizo)

1. Click on the raw image module
2. Ctrl+click (right click) on the module and choose: Display → Slice → Create (Figure 7)
3. This will create a new module named "Slice" that is connected to the raw data module

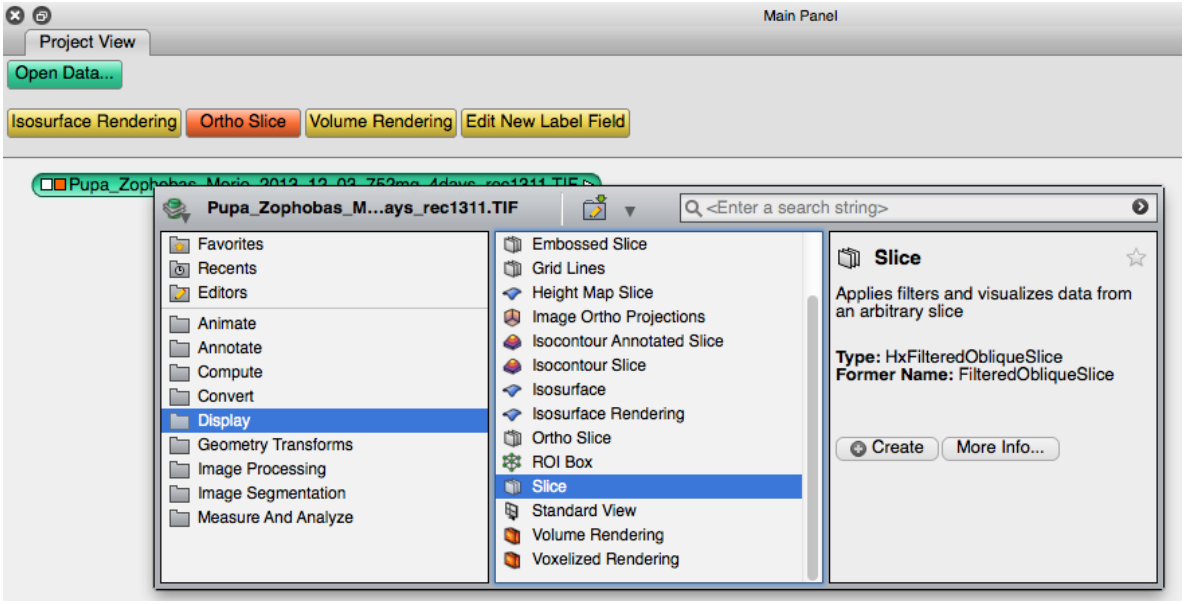

Figure A.3.7: Menu to generate Slice

If you click on the Slice module, there are several options that can be changed that are shown in the properties window (Figure 9):

1. "Data:" chooses the source data to view
2. "Orientation:" allows you to view the xy, xz, and yz slices
3. "Options:" → "rotate" turns off/on the rotate planes which allows the user to rotate the slice in the 3D volume to any possible angle and orientation using a 'sphere' made of three circles for each of the 3D planes (xy, yz, xz) – clicking on one of these circles allows the user to rotate the slice only around that plane (Figure 8)
4. "Sampling:" should be set to 'finest' to make any measurements although this will increase processing time, so a lower sampling can be used If measurements are not being taken
5. The remaining options are not necessary for this protocol but more information can be found in Avizo help

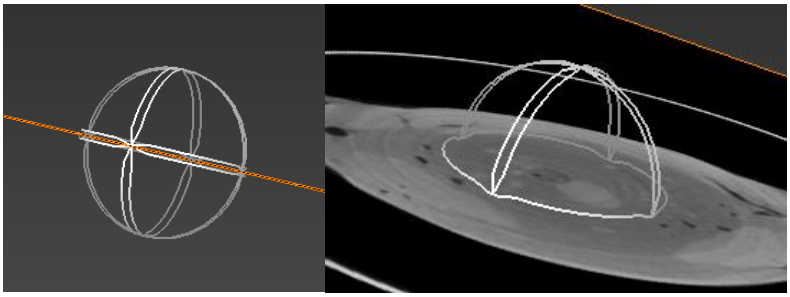

Figure A.3.8: Rotation Planes

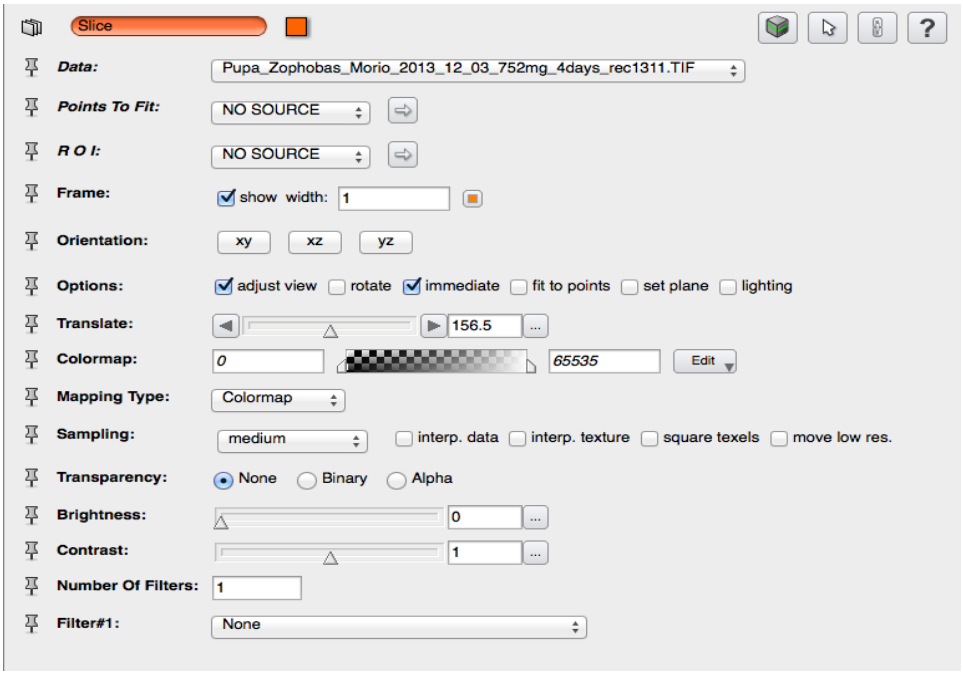

Figure A.3.9: Properties Window of Slice

c. **Isosurface**

Isosurface is a 3D display of the data based on a threshold made from interlaced polygons. To generate an isosurface:

1. Click on the raw image module
2. Ctrl+click on the module and choose: Display → Isosurface Rendering → Create (Figure 10)
   Note: Do not choose "Isosurface" as using this on stacked slices will cause Avizo to crash
3. This will create two new modules named "Volume Rendering Settings" and "Isosurface Rendering" which are paired and connected to the raw data module

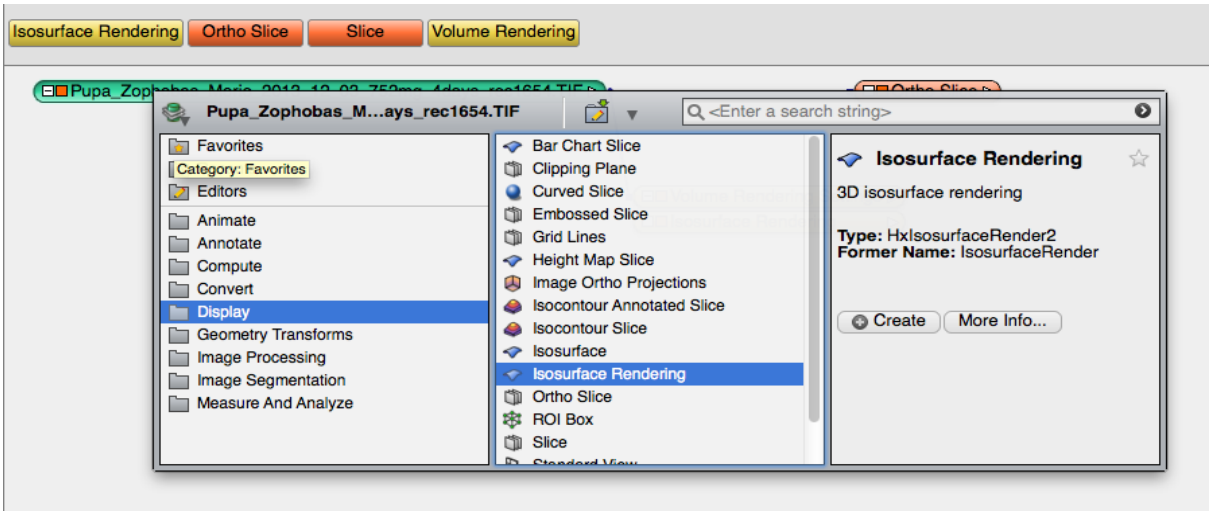

Figure A.3.10: Menu to generate Isosurface Rendering

If you click on the Volume Rendering Settings module, there are several options that can be changed in the properties window. However, in this protocol we do not alter these. More information can be obtained about the different options in Avizo help.

If you click on the Isosurface Rendering module, there are several options that can be changed that are shown in the properties window (Figure 11). The only option that we are concerned with is "Threshold:". This sliding scale determines the threshold value for the image which delineates which image values will be included in the surface and which will not.

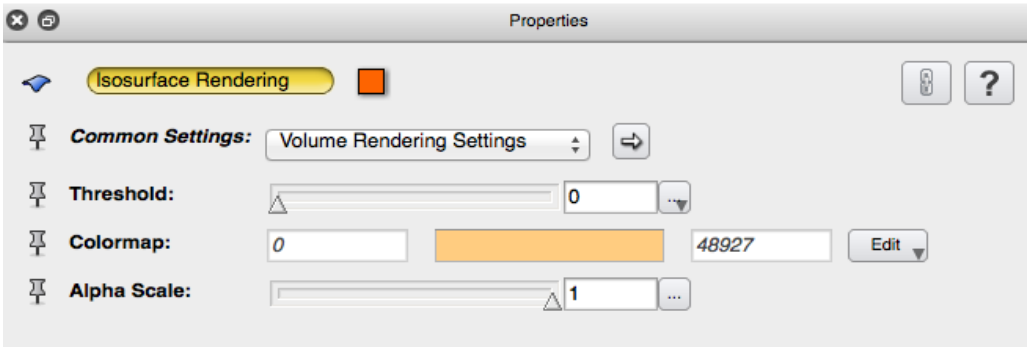

Figure A.3.11: Properties Window of Isosurface Rendering

VI. Prepping for Segmentation

1. Create a label field - Right click on the raw data module and choose ‘Edit New Label Field’

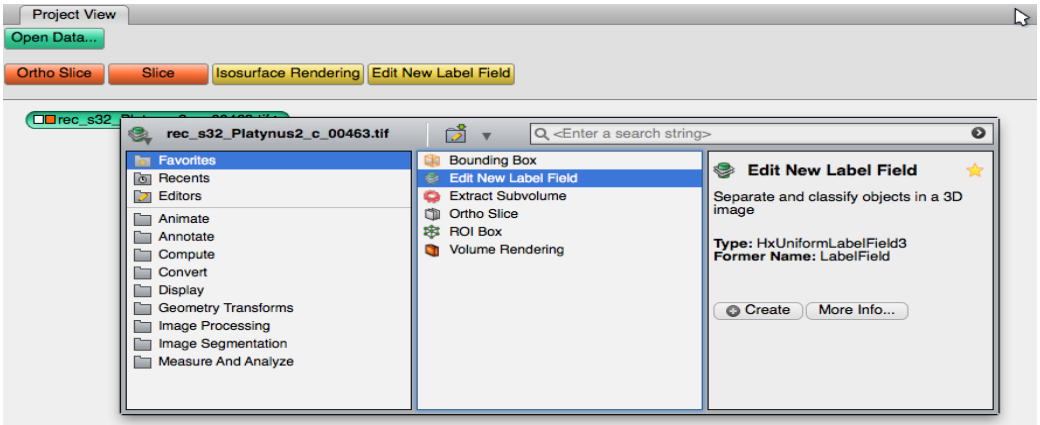

Figure A.3.12: Creating the Label Field

2. This creates a new module – the .labels module – which is directly underneath the raw data module (shown at right)

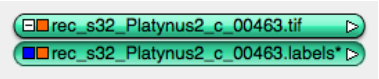

3. Once this is created, the main screen should show different views of the slices, including the 3D view, the xy plane, the xz plane, and the yz plane (Figure 13)
    a) If the main screen does not show these different views, click on the .labels module and at the top right corner of the properties window, click on the “Segmentation tool” (shown at right)

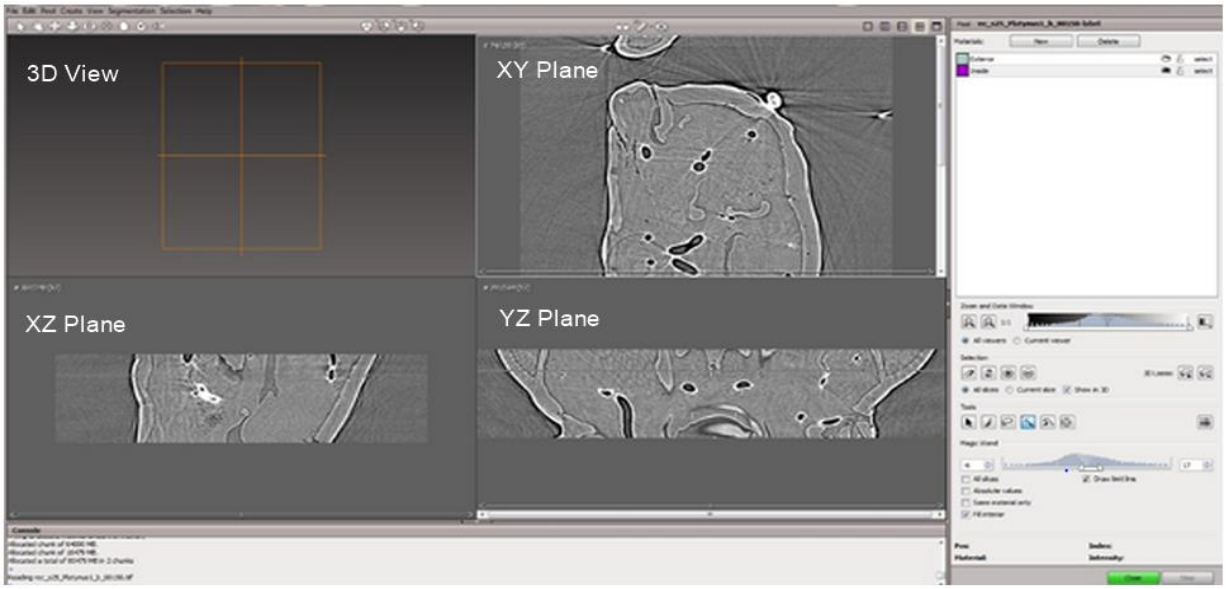

Figure A.3.13: Main screen after creation of a label field showing the different views

4. Once you have the four views, as seen above, make sure the view of interest (generally the xy plane) is outlined in white and then click the single viewer icon on the top right of the main window (both indicated in Figure 14)

Figure A.3.14: Getting to Single View

5. The result of clicking on the single box can be seen below in Figure 15. This is the view of the slice in the XY plane

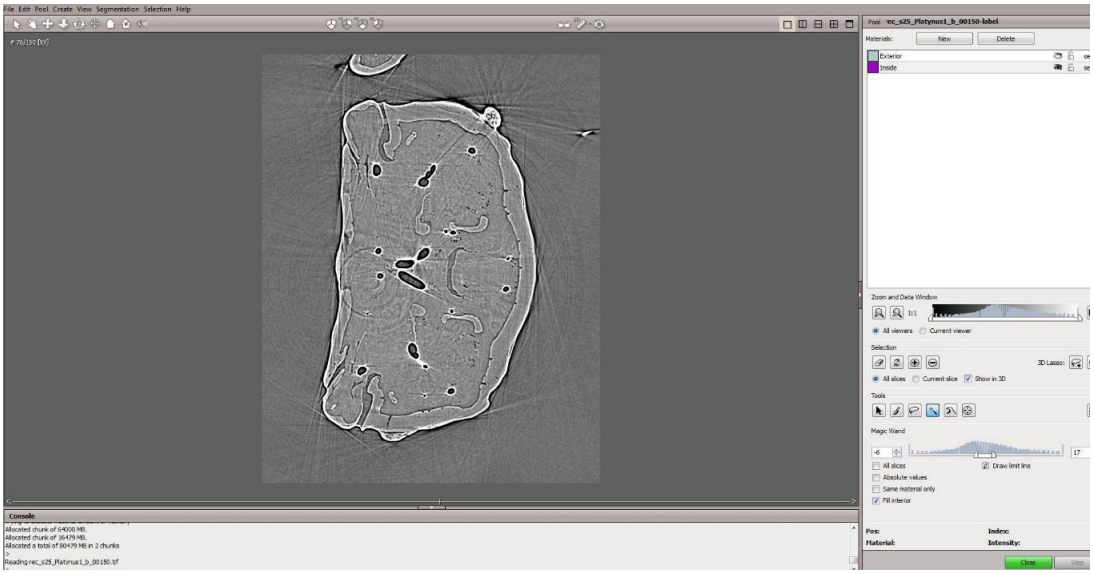

Figure A.3.15: Slice in the XY plane

a. Check to make sure you are in the plane of interest by looking in the top left corner
b. There is also a number in the top left corner that indicates the current slice number out of the total slices

6. When you are editing the label field, it is important to note that the tools used for moving through the data are different from the tools used previously. For example, the cursor will no longer flip through slices, instead use the roller ball on your mouse, the arrow keys on the keyboard, or the slider at the bottom of the main window. In order to zoom in and out; use the magnifying glass  shown in the properties window. Your cursor will then be used to highlight parts of the data for reconstruction.

VII. Saving Your Work

***Avizo is known to crash, so make sure to save your work frequently!!*

1. File → save project as ("save network as" on PC)
2. Name your file
3. File type should be .hx (project)
4. Click save
5. Popup box will appear → click "Autosave" (Figure 16)
    a) Auto Save will save all of the modules that you create (such as your .labels, .surf, etc) in a folder in the same location as the .hx files
        - *Note: If the .surf file is not saved separately, when you reopen the file later it will take a very long time to open as it is recalculating the surface. So before you save, click on the surface module and in the properties, change the Source/Data to "NO SOURCE". Then, when you save, it will ask to autosave the .surf file.*
    b) This allows you to open the .hx file with all the modules so you don't have to create them again or recalculate them
    c) Another file type that might be useful is the 'pack&go' which saves all file types together (.labels, .surf, .hx) which is useful if you plan to transfer the files to another folder

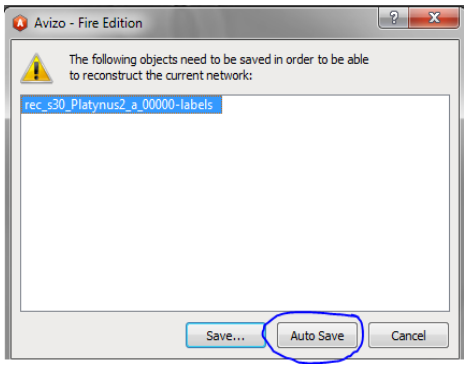

Figure A.3.16: Popup box for saving

VIII. Segmentation Tools

Segmentation in the label field can be done using a variety a tools shown in Figure 17.

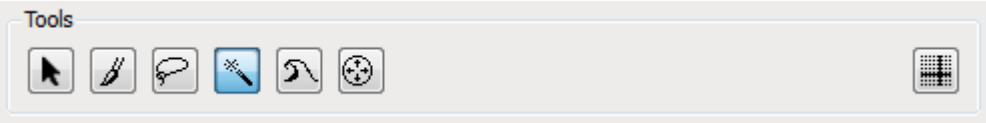

Figure A.3.17: Segmentation tools

Tools (from left to right, as shown in Figure 17):

1. **Pick Region** 

   This tool allows you to modify a selected area. This tool will become important once you have made your first selection using other tools. This can include making the selected area bigger or smaller or moving the area from one region to another. See Figure 18-19 for an example of moving the highlighted area from one region to another

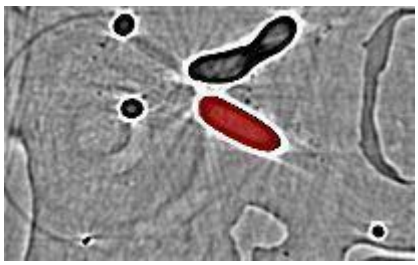

Figure A.3.18: Area selected

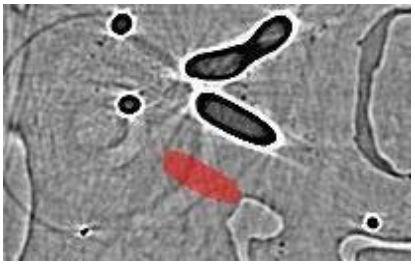

Figure A.3.19: Selected area moved to different region

2. **Brush** 

   This tool is a manual brush that can be used to directly select voxels. Use this if you want to manually choose specific voxels to add or remove. The brush size can be adjusted as necessary (Figure 20).

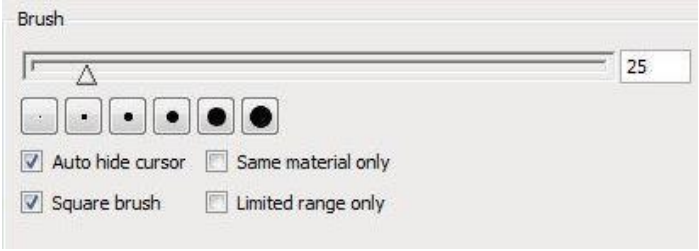

Figure A.3.20: Brush tool options

When to use:

- The brush is a circle, so this can be useful for selecting the voxels within a region that is close to a perfect circle
- There is also an option for choosing "square brush" (Figure 20), this is useful when selecting voxels within a region that is close to a perfect square or has right angles
- This tool is helpful for touching up structures when other tools produce flaws, such as selecting too many voxels or missing a small section due to its geometric qualities

3. **Lasso**

The lasso tool allows you to select a desired area by outlining it. A stylus can be advantageous with the lasso tool, but it can be effective with a mouse as well.

Other properties:

- Autotrace: click on the box next to the word 'boundary' → this allows the lasso tool to find the boundary of an area based on the pixel color when clicking around the outline of the area of interest (where the surface will be created)
    - The closer together you click the better the outline
    - When autotrace is clicked, the option to click "trace edges" becomes available (Figure 21) which will attempt to automatically find the boundary and right clicking will select the voxels within that boundary
- When to use:
    - The lasso tool (without autotrace) is mainly useful for larger structures that cannot be easily or accurately selected using automatic methods
    - Autotrace is useful for structures that have a very obvious boundary or edge
    - If you want to outline a region that has a geometric shape, you can switch to ellipse or rectangular

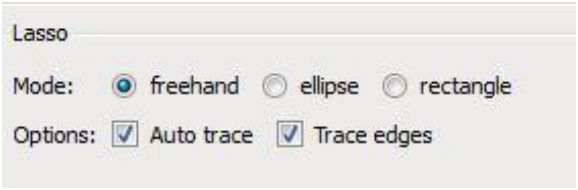

Figure A.3.21: Auto trace and Trace edges

4. **Magic Wand**

The magic wand is an extremely useful tool. The magic wand selects all touching voxels within a specific range of intensity values. To change the range of intensity or threshold values, drag the bar shown in the properties window (Figure 22).

- When to use:
    - When the area you want to select has voxels that appear to be of a similar intensity and are of a markedly different intensity than those around them
    - To get a rough selection of voxels
    - Keep in mind that in many cases the magic wand alone will not be sufficient.

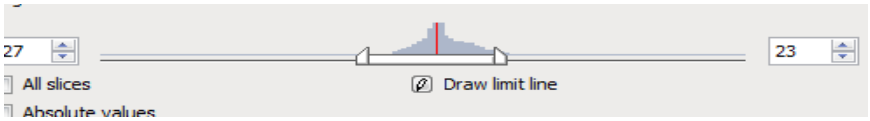

Figure A.3.22: Bar and limit line for Magic Wand Tool

5. **Propagating Front** 

This tool is similar to the magic wand. Instead of setting the intensity range, you click on a point in the middle of the area you want to select (Figure 23) to be your baseline intensity by clicking "Do it". The propagating front tool will select voxels of similar intensities as the baseline intensity. When you slide the "propagating front time slider" (Figure 25), you widen the range of intensities that will be selected.

- You may select multiple areas of similar intensities
- An "X" should appear in the middle of the desired area (Figure 23)
- If the wrong area was selected click 'clear'
- Click "do it" to try again
- Slide the triangle until the desired voxels are selected (Figure 25)

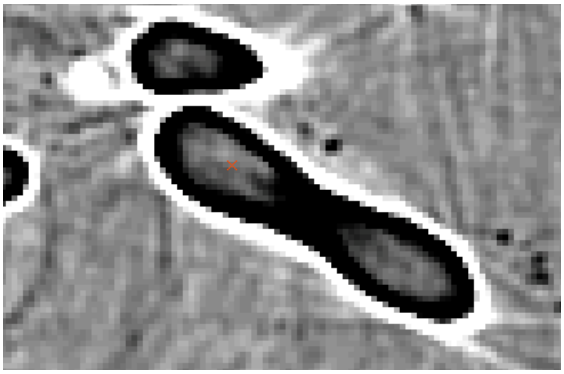

Figure A.3.23: Desired area selected

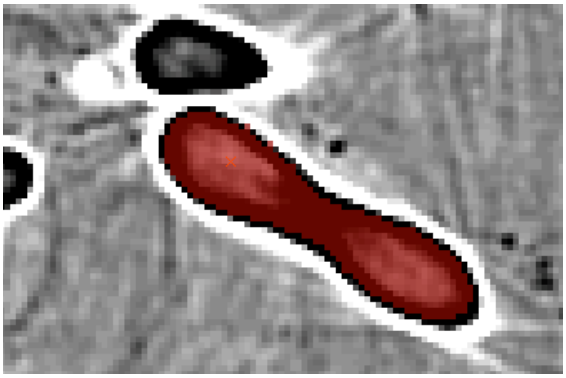

Figure A.3.24: Inside of area filled in

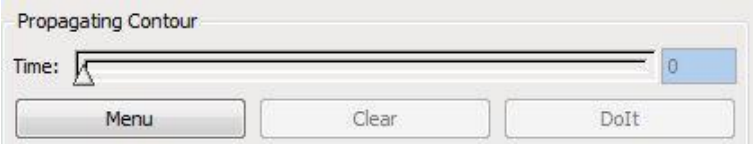

Figure A.3.25: Propagating Contour Time Slider

6. **Blow**

The blow tool expands the voxel selection gradually as you drag, until the desired structure is fully highlighted. First, click on the middle of the area, and hold click and drag away from selected area to increase the allowable intensities. The default tolerance of 35 is probably too high for most purposes; a tolerance of 8-10 tends to work best for data sets of this type. The higher the tolerance, the less dragging you have to do in order to select a greater range of voxel intensities.

7. **Adding/Subtracting from a Selection**

There are a few things to note before beginning segmentation. With the exception of the propagating front tool, only one area can be selected at a time using these tools. If a second area is selected on a slice that already has selected voxels, the original selected voxels will no longer be selected. Thus, to keep this from happening, hold down the shift key before clicking the next section. Conversely, to take certain voxels away from a selection, hold down the control key then select the voxels for removal.

8. **Adding a Selection to Segmentation**

- When you want to add the areas you have outlined, press the  in the selection section
- The area should go from being filled in red to being outlined in purple
    - Purple is the default color for the material used to create the inside of the tubes

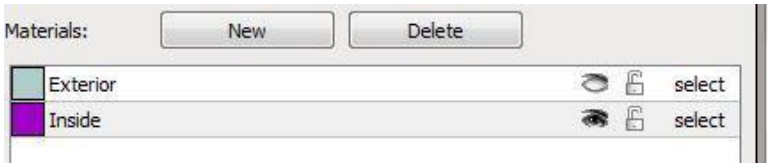

Figure A.3.26: Materials for Segmentation

- Add areas often as Avizo is known to crash!
- When all the areas have been added, click on the button in the lower right corner that says ‘close’

9. **Interpolation**

If you are outlining an area through the images that does not seem to change significantly throughout, use interpolation. Interpolation takes the first selected area and approximates the change throughout the slices to the final selected area.

1. Outline the area of interest in the first slide where you want to begin the interpolation
2. Scroll through the slices until either the shape of the area of interest changes abruptly or you’ve gone about 10-15 slices (more than this usually results in a poor interpolation)
3. Outline the area of interest in the slice where you’ve halted scrolling
4. Selection → interpolate (should see ‘interpolating slices a through b’ in the command window) - Shortcut: Press Ctrl+i

5. Scroll through all the slices between the two you selected. Check to see that slices are correctly outlined and make any necessary adjustments if needed

IX. Generate Surface

To generate the surface from the segmentation you created, you need to tell Avizo to compute the triangulation

1. Right click (Ctrl+click) on the .labels module and find the "Generate Surface" function and click "Create" (Figure 27)

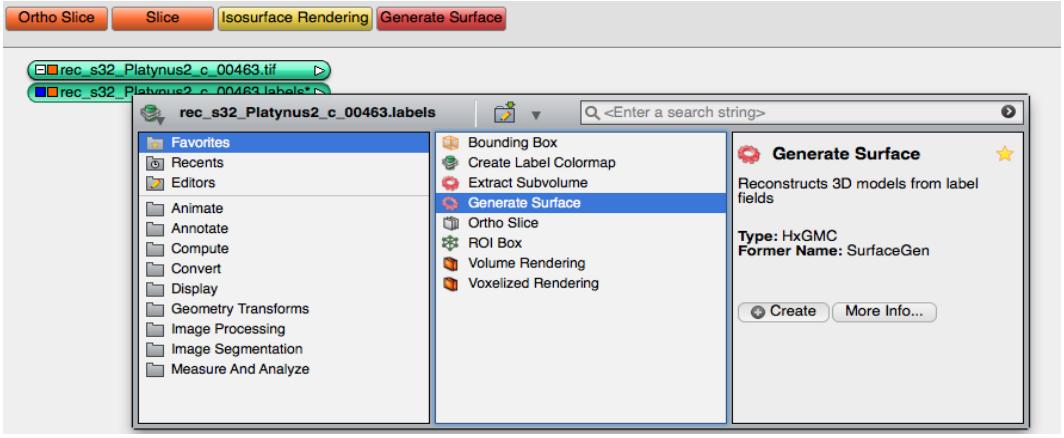

Figure A.3.27: Generate Surface function

2. A red module labeled 'Generate Surface' should be created and connected by a line to the .labels module in the display window
    a. Click on this module and look at the properties window (Figure 28)
    b. There are many different surface properties, the most important one here is the "Smoothing type:" which should be set to "unconstrained smoothing"
    c. Once you have your settings as you want them, click "Apply" in the bottom right of the properties window
    d. This might take a long time depending on how many slices you have

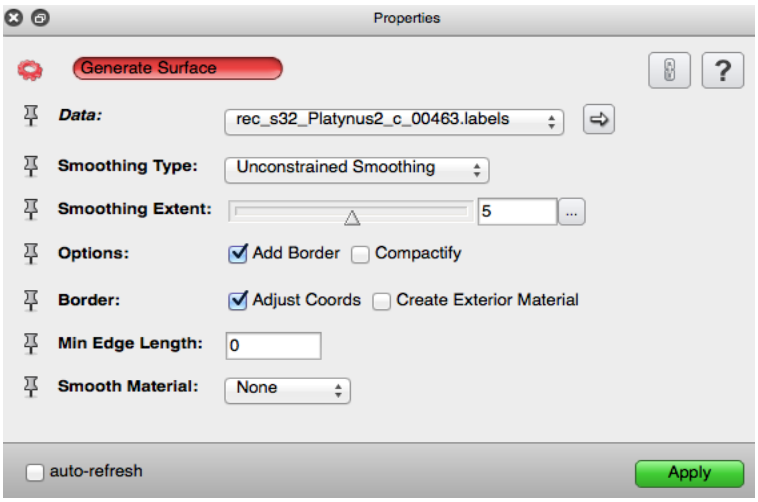

Figure A.3.28: Properties window for Generate Surface module

3. A .surf module should be created and connected to the Generate Surface module by a line
    a. The .surf file can then be saved separately from the .hx file, similar to the .labels file
    b. It is important to save the .surf file separately! Otherwise, it will recalculate the surface every time you open the file. In order to make it save separately, click on the .surf module and in the properties, change the Master to "NO SOURCE". Then, when you save, it will ask to autosave the .surf file. (You might also need to change the Data: to "NO SOURCE" in the properties window of the Generate Surface module.)

4. In order to view the surface, right click (Ctrl+click) on the .surf module and do to Display → Surface View → Create (Figure 29). You should now be able to view the surface and manipulate it in the main window.

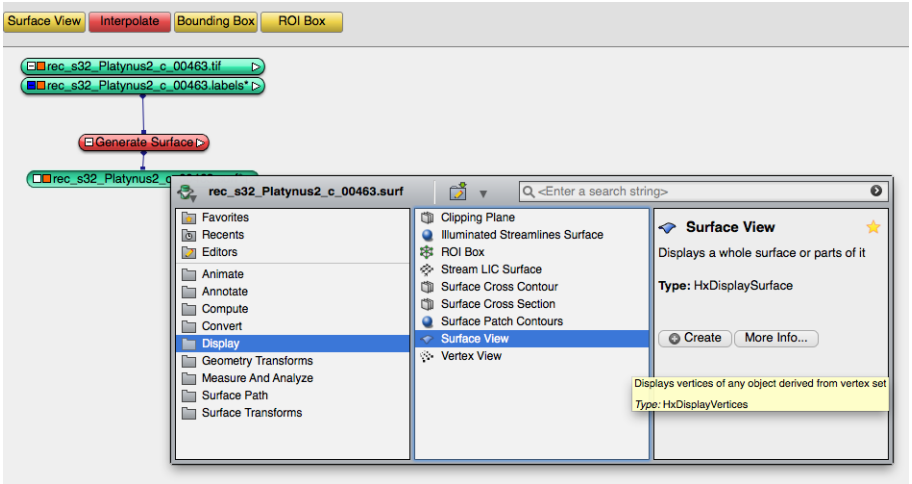

Figure A.3.29: Surface View

Note: If you create the surface and then go back to do segmentation, you will have to go through the process of creating the surface a second time and the module will be labeled SurfaceGen2

X. Toolbar

Figure A.3.30: Toolbar with descriptions of each numbered item below.

1. This is your regular mouse and go to for scrolling through slices
2. The hand allows you to rotate the image
3. The crossing arrows allow you to drag the image up-down-side-side (shortcut: hold trackball and drag)
4. The arrow zooms in/out of the image (shortcut: rolling trackball)
5. The circular arrows will shift the image a few degrees clockwise
6. The four arrows will allow you to click on a point in the image and it will zoom to that point
7. The house will go back to the home image
8. The house made out of arrows set the current view as your home view
9. The backwards arrows go to the perspective view
10. Select which plane to view the data on
11. Enable and disable stereo viewing
12. Measurement tool (length, angle, etc)
13. Takes a snapshot of the screen and saves it
14. Choose how you want the screen to be set up

XI. Taking Measurements

1. Choose the measurement tool (#12 in Figure 30)
2. This tool has several different options, including measuring length and angles in both 2D and 3D. Since you are working with 3D data, using the 3D tool is much more helpful as the endpoints of the line or angle you generate will stick on the 3D slice or surface
3. Once you begin making a measurement, this will generate a standalone 'Measurement' module where you measurements are stored and the visibility of each measurement can be turned off or on (Figure 31). Remember your measurements are in units/pixels and will need to be converted to your units of choice
4. Take a snapshot of the measurement on screen (#13 in Figure 30) for your records

Figure A.3.31: Properties of a Measurement module with one measurement showing.

Appendix B

Chapter 3 supporting information

B.1 Code repository

https://github.com/TheSochaLab/How-temperature-affects-the-viscosity-of-hornworm-hemolymph

B.2 Supplemental materials

Table B.2.1: Minimum and maximum measurable viscosity for each shear rate for each spindle. The shear rate, minimum measurable viscosity, and maximum measurable viscosity are calculated and shown following the equations shown in bold for each spindle.

Spindle	Rotation Speed (RPM)	Shear Rate (s^{-1})	Minimum Viscosity (cP)	Maximum Viscosity (cP)
CP-40	**N**	**7.5N**	**30.7/N**	**307/N**
	15	112.5	2.05	20.47
	30	225	1.02	10.23
	45	337.5	0.68	6.82
	60	450	0.51	5.12
	75	562.5	0.41	4.09
	90	675	0.34	3.41
	105	787.5	0.29	2.92
	120	900	0.26	2.56
	135	1012.5	0.23	2.27
CP-51	**N**	**3.84N**	**485.4/N**	**4854/N**
	15	57.6	32.36	323.60
	30	115.2	16.18	161.80
	45	172.8	10.79	107.87
	60	230.4	8.09	80.90
	75	288	6.47	64.72
	90	345.6	5.39	53.93
	105	403.2	4.62	46.23
	120	460.8	4.05	40.45
	135	518.4	3.60	35.96

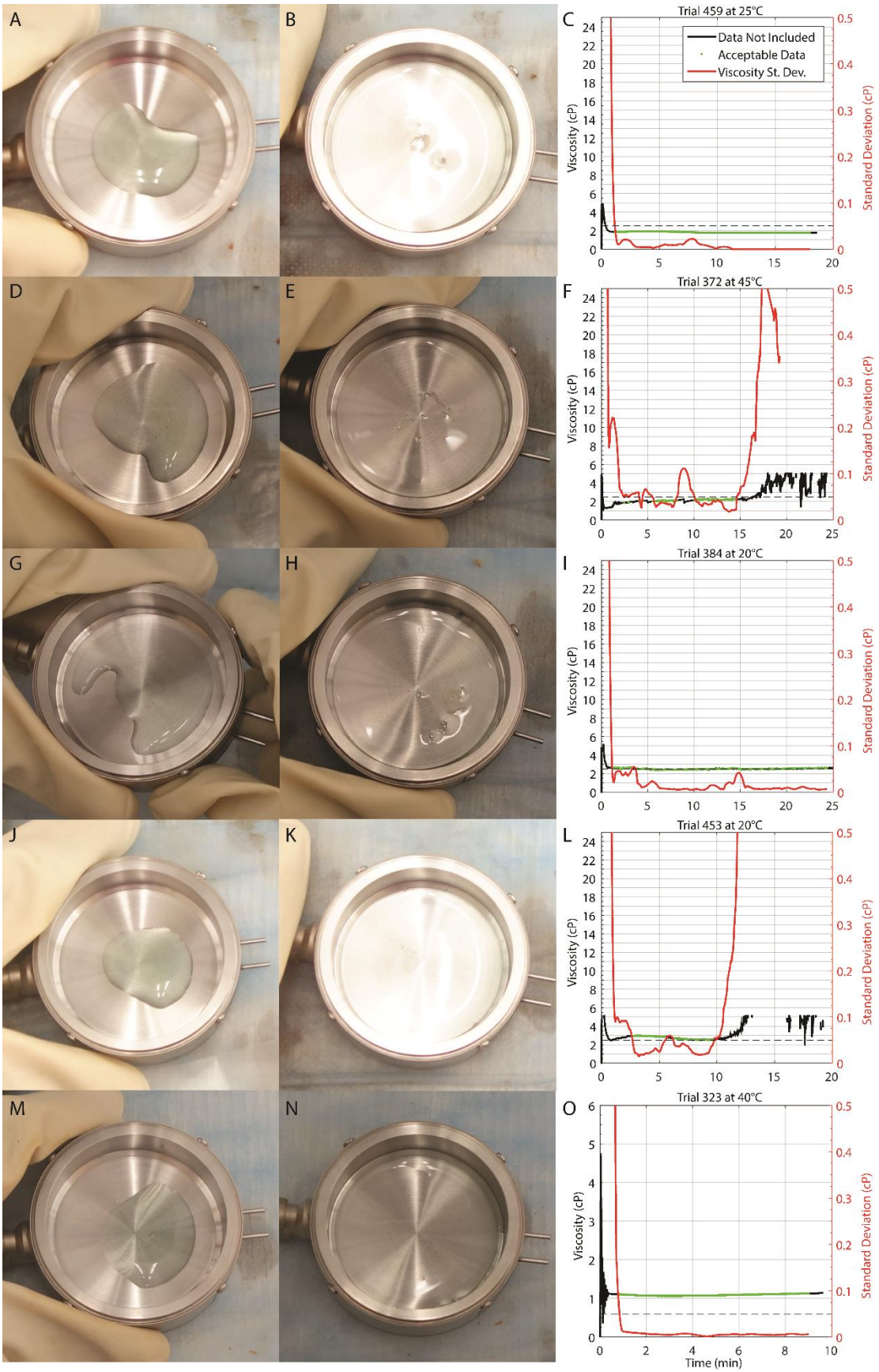
A
B
C
Trial 459 at 25°C
Data Not Included
Acceptable Data
Viscosity St. Dev.
Viscosity (cP)
Standard Deviation (cP)
D
E
F
Trial 372 at 45°C
G
H
I
Trial 384 at 20°C
J
K
L
Trial 453 at 20°C
M
N
O
Trial 323 at 40°C
Time (min)

Figure B.2.1 (previous page): Photos of *Manduca sexta* hemolymph before (left column; A, D, G, J, M) and after (middle column; B, E, H, K, N) trials in the viscometer, with corresponding data traces (right column; C, F, I, L, O). Each row represents an individual trial. From these photos, an estimate of the number of clots and their size was made using ImageJ software. For scale, the outer diameter of the cup was 63.5 mm. Generally, viscosity measurements were more steady for plasma trials than whole hemolymph trials. For some samples, a clot was found on the spindle (held by surface tension), which is not shown in the photo. Due to blur or reflection on the surface of the sample, some images could not be analyzed. Of the whole hemolymph trials, 38 of 55 were analyzed for number and size of clots. Of these, 11 (29%) did not have a clot (e.g., H and K), and 27 showed the presence of one to four clots (e.g., B and E). These clots ranged in size from 0.4 to 8.6 mm in diameter. The presence of clots did not always indicate a steady (e.g., C and I) or unsteady (e.g., F and L) viscosity measurement over time. Of the plasma trials, 36 of 50 were analyzed. Of these, 28 (77.8%) did not have a clot (N), and 8 showed the presence of one or two small clots, ranging in size from 0.6 to 2.8 mm in diameter. Typically, when large clots (>3 mm) were found, only one such clot was present. For the traces in the right column, the title indicates the temperature and trial number. The raw viscosity data are indicated in black and green, with green indicating that the standard deviation (plotted in red) was below 0.05. Only green data were included in the calculated average for the trial.

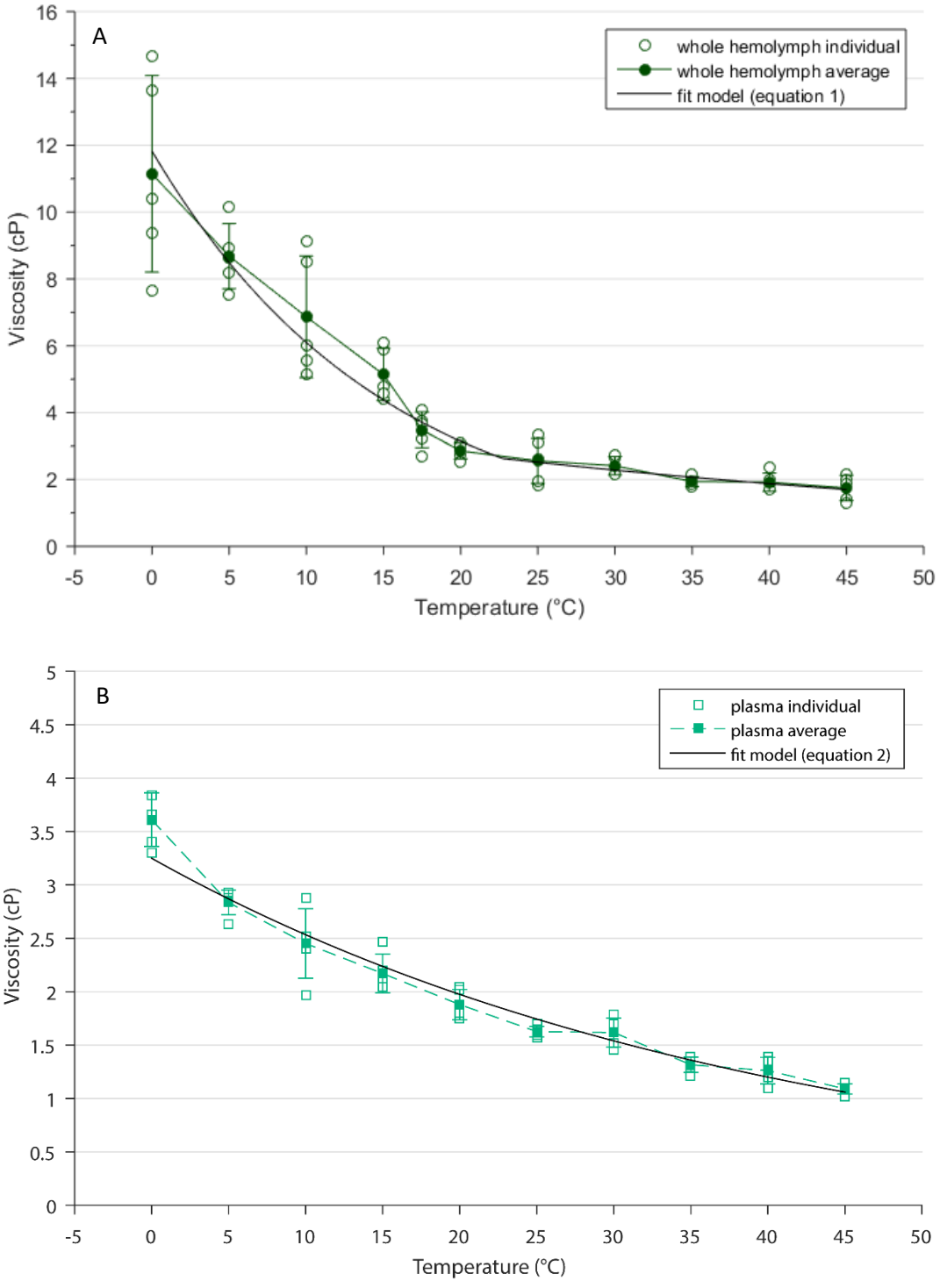

Figure B.2.2: Viscosity versus temperature for whole hemolymph (A) and plasma (B), including the exponential fit line Eqn. 3.1 (A) and Eqn. 3.2 (B).

Whole hemolymph

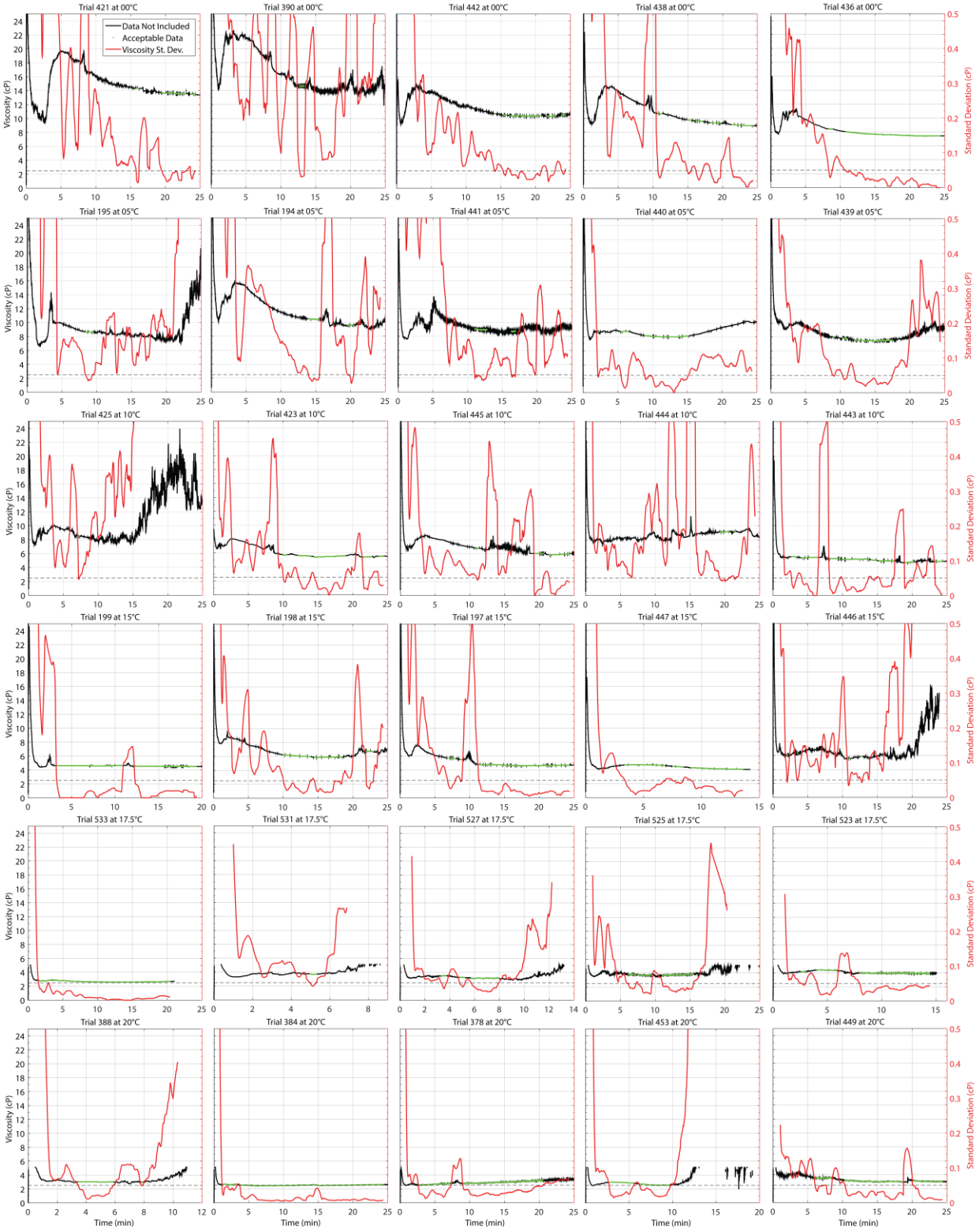

Whole hemolymph

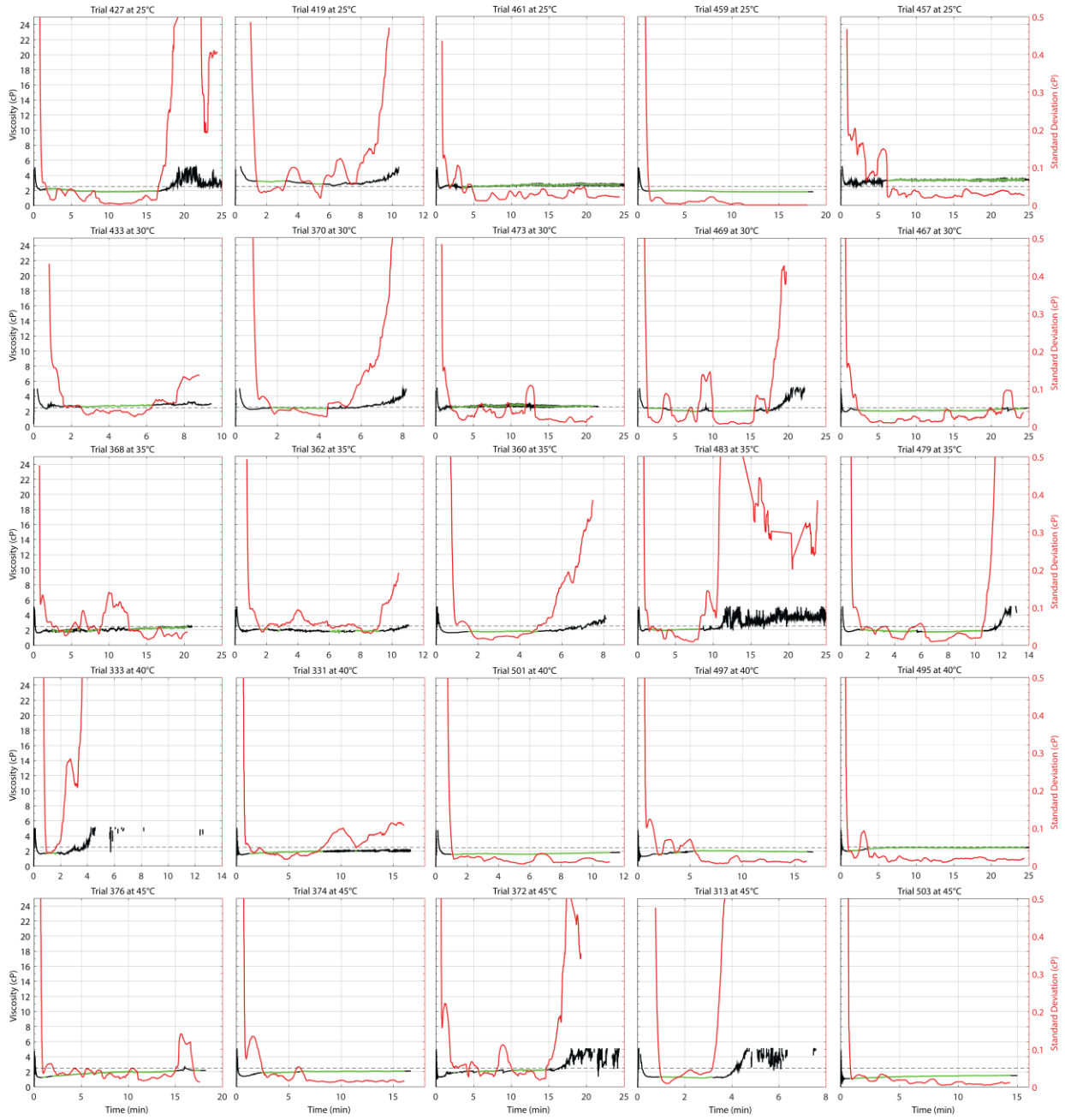

Plasma

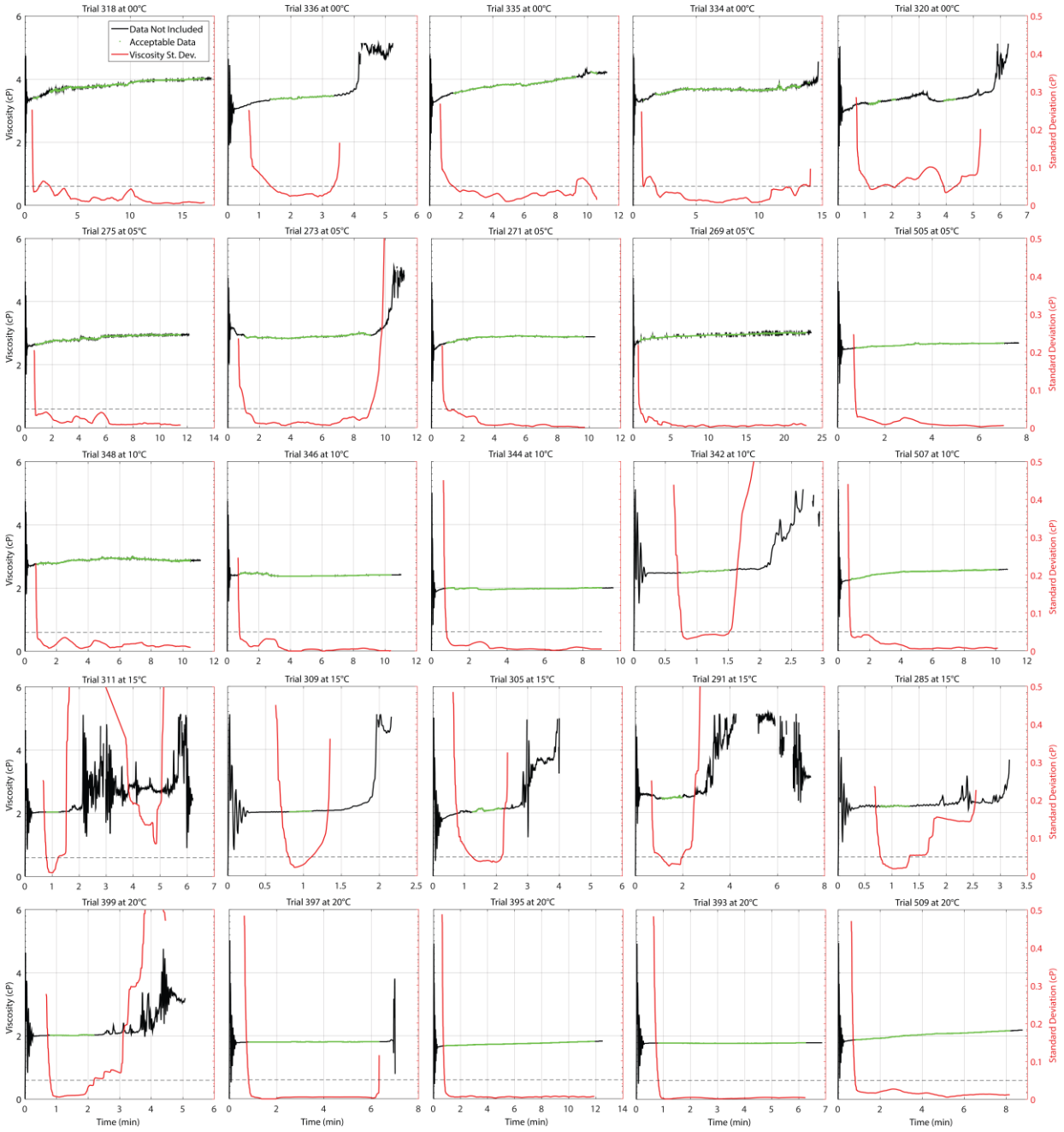
Trial 318 at 00°C
Trial 336 at 00°C
Trial 335 at 00°C
Trial 334 at 00°C
Trial 320 at 00°C
Trial 275 at 05°C
Trial 273 at 05°C
Trial 271 at 05°C
Trial 269 at 05°C
Trial 505 at 05°C
Trial 348 at 10°C
Trial 346 at 10°C
Trial 344 at 10°C
Trial 342 at 10°C
Trial 507 at 10°C
Trial 311 at 15°C
Trial 309 at 15°C
Trial 305 at 15°C
Trial 291 at 15°C
Trial 285 at 15°C
Trial 399 at 20°C
Trial 397 at 20°C
Trial 395 at 20°C
Trial 393 at 20°C
Trial 509 at 20°C
Data Not Included
Acceptable Data
Viscosity St. Dev.
Viscosity (cP)
Standard Deviation (cP)
Time (min)

Plasma

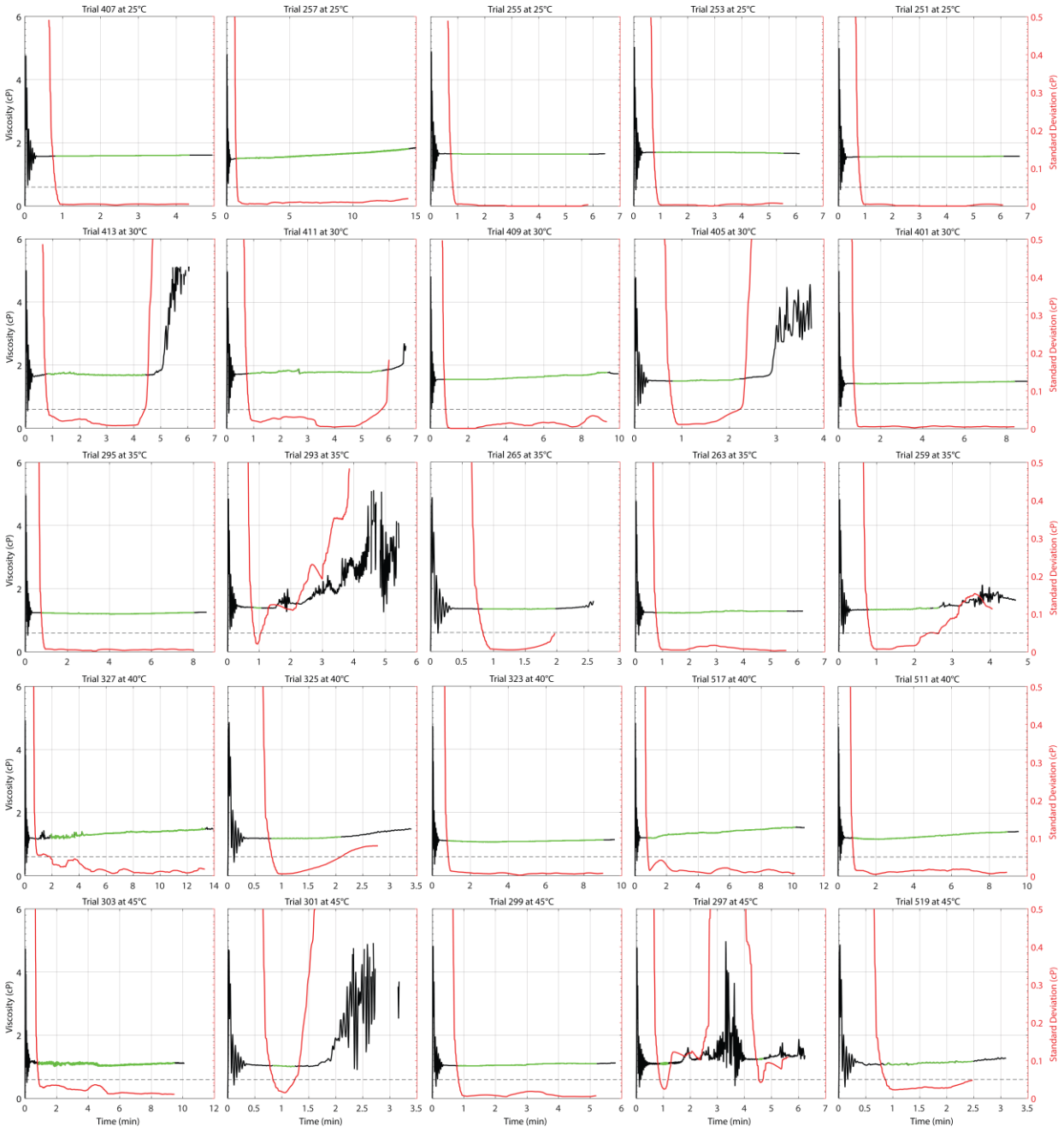

Figure B.2.3 (previous pages): Traces of viscosity over time for each whole hemolymph (n=55) and plasma (n=50) trial. Each row represents a different temperature of the water bath for that trial. The first 11 rows are trials using whole hemolymph while the following 10 are using plasma. The title of each graph indicates the temperature and trial number. The raw viscosity data are indicated in black and green, with green indicating that the standard deviation (plotted in red) was below 0.05. Only green data were included in the calculated average for the trial.

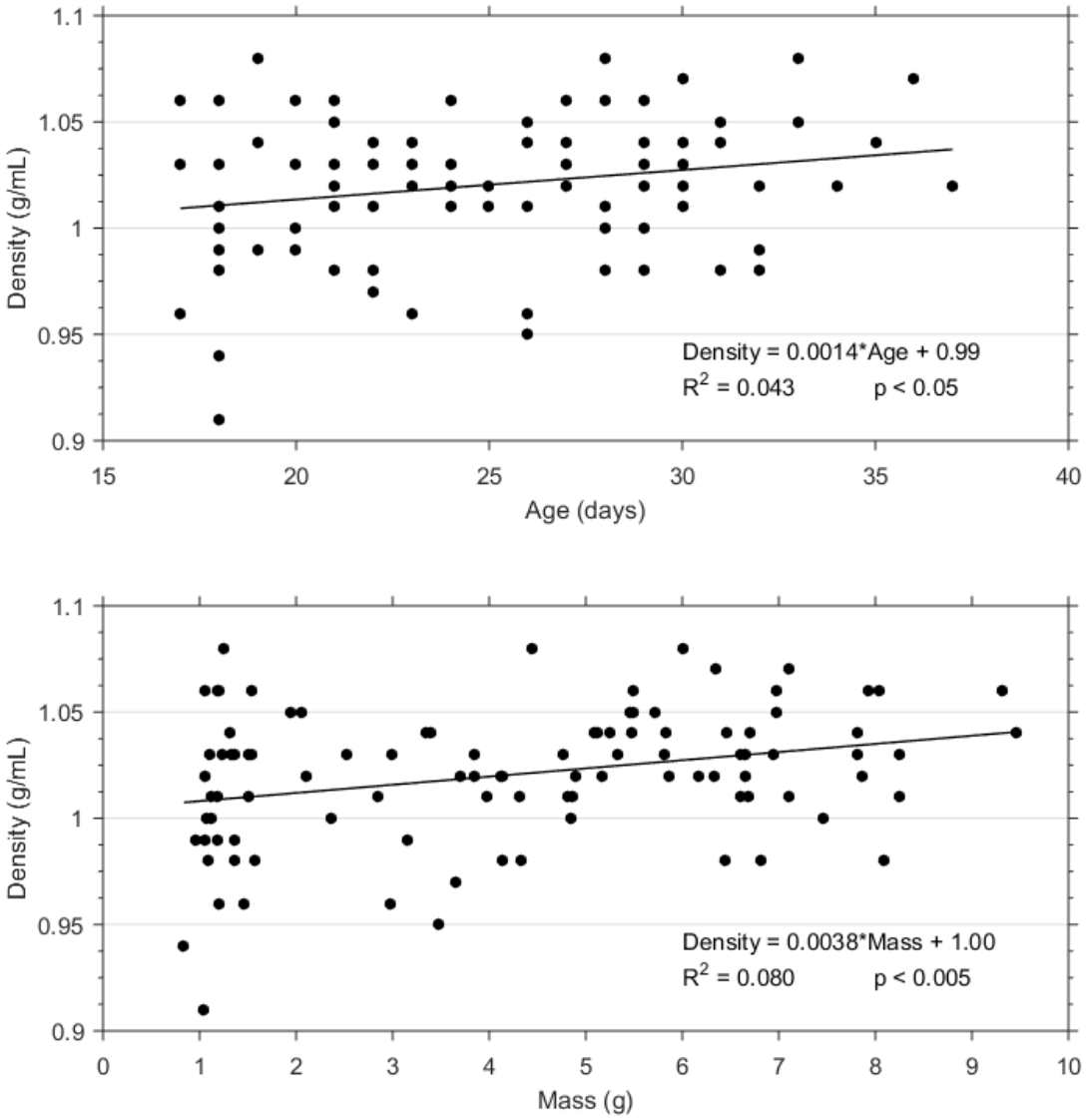

Figure B.2.4: Density of whole hemolymph versus age of larvae (top) and density of whole hemolymph versus mass of larvae (bottom). There is a significant positive correlation between both age and mass with density of the whole hemolymph.

B.3 Hornworm care

This document describes the care of *Manduca sexta* larvae only (not through pupation or adult stages). The hornworm's lifespan, before pupation, ranges from approximately 15 to 25 days at room temperature (~22°C). They grow more slowly at lower temperatures and more quickly at higher temperatures. It is important to note that the hornworms are both competitive for resources and tend to pupate synchronously when reared together. This is why separate rearing of larvae in individual containers can significantly increase both survival rate and larvae size before pre-pupation begins.

Authors: Melissa Kenny (mck66@vt.edu) and Christie Crandall (ccran@vt.edu)

Preparation:

ORDERING LARVAE: The larvae can be obtained from several different sources, listed below.

- Carolina Biological (https://www.carolina.com) – Can supply eggs or very small 1st or 2nd instar larvae or pupae. Carolina is relatively expensive but is a reputable company with good customer service that is easy to reach. They also sell the tobacco meal in large containers.
- Backwater Reptiles (http://www.backwaterreptiles.com) – Can supply either eggs or 1-1.5 in larvae for a somewhat reasonable price. Backwater Reptiles does not have any method of customer service besides email (no phone number) so it can sometimes take time to receive answers to any questions or concerns. They do not sell the tobacco meal separately.
- Great Lakes Hornworms (http://www.greatlakeshornworm.com) – Can supply several different size hornworms or eggs. Great Lakes has truly amazing customer service and will fill special requests for size as well. They have always put more worms than advertised in each container. Their prices are very good and tobacco meal is cheap for a large container. They ship almost immediately to arrive in two days (so will only ship on Mondays, Tuesdays, or Wednesdays each week).
- University of Washington – The Riddiford Lab at University of Washington has a hornworm colony and will send worms at whatever size is needed with enough notice. You must email Binh Nguyen (anhbinh@uw.edu) at least 1.5 weeks in advance to receive them. The worms are shipped overnight and arrive in individual containers. The cost is $2.36 per worm which can get expensive fast.

MATERIALS: Before receiving hornworms, make sure you have the following materials ready:

- Individual containers – 8 oz clear deli containers with lids work well with air holes poked through the sides, similar to these: https://www.amazon.com/gp/product/B0743K62KZ/
- Space to keep the worms while they grow
- Tweezers
- Gloves
- Hornworm food – tobacco meal, which can be purchased with the animals
- Cleaning tools (e.g., popsicle sticks, paper towels, trashcan, etc.)

Maintenance:

CLEANING: Cleaning of the containers should occur when needed. For large larvae (>5 g) this might be daily, but small larvae may only be once a week. Use judgement to determine when feces need to be removed. Any mold or fungus growth should be cleaned out immediately when found.

When cleaning the worms, for each container first remove the worm and any viable food then scrape out any feces, mold, etc. into the trash can. The container can now either be wiped out with a paper towel, or washed with soap in the sink and dried.

FEEDING: All larvae should be checked daily to see if they need feeding. Occasionally, a day can be skipped if they are given some additional food to tide them over. If a large quantity of food is given, it can easily grow mold in as little as 2-3 days. Food should be given as a single solid piece so it does not dry out too quickly.

Food can be distributed using a spoon, popsicle stick, or any similar tool from the container received and should be refrigerated between feedings. The amount of food is based on the size of the worm, as detailed below:

- 0.25-1 in length – 1 cm^3 of tobacco meal
- 1-2 in length – 2-3 cm^3 of tobacco meal
- 3+ in length – 4 cm^3 of tobacco meal or more if necessary, because lack of food can trigger early pre-pupation

The larvae do not require any additional water or food; the tobacco meal is moist enough to keep them hydrated.

Size-Specific Care:

EGGS: Eggs will be green until hatched and transparent after the larvae has emerged, which can take approximately 4-5 days. Many eggs can be placed in one tub together. Place a small amount of food in the container with the eggs so the newly-hatched larvae migrate to it and can more easily be removed. This also keeps the larvae from trying to escape in search of food. Wait until their horns develop and turn black before moving the young larvae to new containers.

BABIES: Once the newly-hatched larvae have black horns, remove the larvae from the egg container into individual containers. This can be done most easily by pinching their horns with tweezers. House the newly hatched larvae (first instar) about 8-10 per individual container to begin because there will be a huge number of them and survival rate is not very high at this age. Once they grow to ~0.5-0.75 inch in length (about second instar), separate to 2-4 per container. At 1 inch in length (approaching third instar), begin rearing them individually in the containers.

When they are housed together, try to keep the size of all the larvae within a container consistent.

MIDDLE-AGE: Once the worms reach 1 inch in length, they will grow fast. Some will grow faster than others and some will require more food than others. Once the larvae reach fourth instar, they will shed their head capsule and it will be noticeable in their container.

FIFTH INSTAR: This brings the most changes in the larvae, as it will more than double in size and consume a considerable amount of food. Without available food, they may pupate early. At this stage, they can reach up to 13 g.

PREPUPATION: Larvae will enter their 'wandering' stage late in their fifth instar. At this stage, their dorsal vessel becomes significantly more apparent along the dorsal vessel, their cuticle will become less flexible, and they will begin moving a lot around their container. They are looking for a location to burrow to pupate, which is most noticeable by the smearing of food and feces all over the walls of the containers. They will begin to shrink and become more yellow as they pupate, before turning brown and hardening completely.

Troubleshooting:

HUMID TUBS: If there seems to be a lot of humidity in their tubs, poke more holes. This may also be caused by too much food.

DEATH: Many worms will die. If they are brown and in liquid, they have probably died. It is usually easy to identify dead worms. If you are unsure, take care of them as normal and check them again another day.

CUTICLE SHED: When they shed their head capsule and cuticle before fifth instar, it is not always shed cleanly and completely. It will sometimes constrict them somewhere along their soft exoskeleton and result in the hornworm looking cinched in one place or even sickly. A razor or tweezers can be used very carefully to help remove the remaining cuticle in these cases and most larvae will recover completely.

B.4 Viscometer standard operating procedure

This document includes use of the viscometer within the environmental chamber in the Socha Lab. This viscometer is connected to a circulating water bath for temperature control. This set-up has been used mostly for measuring the viscosity of insect hemolymph and thus, this SOP focuses on these types of experiments.

Authors: Melissa Kenny (mck66@vt.edu) and Christie Crandall (ccran@vt.edu)

List of equipment used:

- Viscometer: DV-II+ Pro, Brookfield Engineering
- Water bath: RE 206, Lauda
- Glovebox: CleaTech Critical Laboratory Supplies
- Oxygen sensor: Expedition X O2 Analyzer, OxyCheq
- Humidifier: Ultrasonic Cool Mist, Pure Enrichment
- Hygrometer: Traceable, Fisher Scientific

1. Turn on the water bath and set to the desired temperature

Use the up and down arrows on the front of the control panel to adjust the temperature on the digital display. Press the 'set' button when you've reached the desired temperature. Know that a lower temperature (10 C) may take up to an hour to achieve.

2. Prepare the glovebox for experiments

Make sure you have all of the equipment you need within the glovebox for your experiments before proceeding to the next step. This items may include empty beaker(s), parafilm pieces, sharp razor, pipette tips, distilled water, Kimwipes, pipette, etc.

3. Set up the Oxycheq

1. Calibration: Switch on the Oxycheq and hold the probe over an open window so it is reading the oxygen in the fresh air outside the building. Using the round knob labelled 'Cal', adjust the value on the digital display to read '20.9'.

2. Placement: Place the oxycheq control box inside the glovebox where it isn't in the way but the digital display can be easily read. Place the probe close to where the sample will be extracted.
    i. Note: Usually the best placement is for the control box to be in the left/front corner of the glovebox with the probe resting against the front between the two gloves so it is near the workspace.

4. Flood the box with nitrogen gas

IMPORTANT: Before using the gas cylinders in the lab, you must be trained by Dr. Socha in their use (not another lab member). Misuse of the gas cylinders can cause serious injury!

1. Prep the glovebox: Make sure all of the doors to the glovebox are securely closed and any wires are secured with sticky tack to ensure the box is as air tight as possible. Although there is generally enough leakage from the box to keep pressure from building, make sure the port on the back left side is open (pictured).

2. Begin nitrogen gas: Turn the gas cylinder to 15-18 psi to begin then move to the next step while the oxygen concentration lowers.
    i. Once the oxygen concentration (via the Oxycheq) drops to ~5%, the gas cylinder can be adjusted to ~10 psi and lowered further to 5 psi when the oxygen is <2%.
    ii. Note: Keep an eye on the oxygen concentration from now on. The gas cylinder may need to be adjusted higher or lower to maintain an oxygen concentration of <2%. Every time the door is opened, the gas cylinder will likely need to be turned up.

5. Turn on the humidifier

1. Once the nitrogen is flowing, turn on/off the humidifier by touching the power button on the front in order to maintain humidity between 60-80% (read via the digital hygrometer within the box). The humidifier has four settings based on the number of times you touch the on button:
    i. 1st touch: Humidifier on low, light off
    ii. 2nd touch: Humidifier on low, light on
    iii. 3rd touch: Humidifier on high, light on
    iv. 4th touch: Humidifier on high, light off
    v. 5th touch: Humidifier off

Note: The light is not necessary, but is a feature of the machine; whether it is on or off does not matter for experiments.

2. Be careful leaving the humidifier on either of the high settings for too long as it will raise the humidity to 95+% very quickly and fog up the box which could harm the electrical equipment within! Additionally, if the gas cylinder is set to <8 psi, the humidity may rise too high even on the low settings on the humidifier so be careful to keep an eye on the hygrometer.

6. Prepare your sample

1. Label an empty 50 mL centrifuge tube, place it on the scale, and zero the scale. Place a *Manduca sexta* larvae within the tube and record the body mass. Take a photo of the larvae, then place the larvae within the tube into the glovebox. Try to make sure the glovebox door is open for only a small amount of time, otherwise the oxygen level will raise rapidly.

2. To anesthetize the animal, open the tube containing the animal within the glovebox. This is more effective if the oxygen concentration is already <2%. It will take about 5-10 min at low oxygen to fully sedate a *Manduca sexta* larvae.

7. Prepare the viscometer

Turn on the viscometer using the switch on the back left of the machine. When prompted on the digital display, choose "standalone mode" by pressing the down arrow button. Press any key on the front to continue when prompted.

8. Attach the spindle

If you're unsure what spindle to use, use the table on the next page to determine at what combination of spindle and rotation speed the measurable viscosity range will be able to measure the viscosity of the fluid to be tested.

1. **Make sure the spindle is clean!** The spindle can be cleaned using distilled water and Kimwipes. Do NOT use isopropyl alcohol, as it vaporizes, filling the box, and can affect both the larvae and the hemolymph sample.

2. Once clean, take the wrench and place it around the attachment site on the viscometer along the flat spaces where it fits. While holding the wrench still and in place, position the spindle below the exposed screw at the bottom of the viscometer (you may need to 'straddle' the bar on the right side with your hand). Screw the spindle onto the viscometer. I recommend you use your two hands as follows (pictured):
    i. Left hand: hold the wrench still and place a single finger below the spindle to steady it and keep it against the screw
    ii. Right hand: 'straddling' the bar on the right and slowly turning the spindle clockwise until the threads catch the screw.

3. Attaching the spindle can be one of the most difficult tasks in setting up the viscometer and takes practice. Be careful to touch the spindle as little as possible, to keep it clean. After attaching the spindle, use Kimwipes and distilled water to wipe it down again.

4. Press any key on the viscometer to indicate the spindle is attached.

9. Set up viscometer for specific trial

1. <u>Set the spindle:</u> Press the button labelled 'Set Spindle' on the viscometer, then use the up and down arrow buttons to scroll to either 40 (the larger spindle) or 51 (the smaller spindle).

2. <u>Set the rotation speed:</u> Press the button labelled 'Set Speed" on the viscometer, then use the up and down arrow buttons to scroll to the speed to use.

10. Set up the computer

Note: If the Mac boots into windows, restart and as it is booting hold the "Option" button down until it prompts which drive to boot from, choose the one NOT named "windows".

1. Computer username: labuser
   Computer password: SochaLab4

2. Open the program 'CoolTerm' and open a new file. In the top menu, choose 'Connection' then 'Capture to Textfile' then 'Start' then enter the name and location of the file you are about to collect data within.

11. Calibrate the cup

1. Clean the cup: Begin by thoroughly cleaning the cup using distilled water and Kimwipes.

2. Attach the cup: Place the cup around the spindle with the two side prongs around the lever on the right. Pull the lever under the cup to secure it in place, being careful not to get the gloves caught between the cup and the lever.

3. Set the gap size: The gap size is critical to obtaining an accurate measurements. To calibrate the size of the gap between the cup and the spindle bottom, turn on the switch right above the spindle on the viscometer.
   i. If the yellow light turns on immediately, turn it clockwise until the moment it turns off.
   ii. If the yellow light is off, turn it counter clockwise until the moment it turns on.
   iii. If the yellow light does not appear to turn on after turning the dial a full turn in either direction, first try lightly tapping the dial with your hand on the side. Sometimes the light will then turn on or flicker on. If this still doesn't work, use distilled water and a Kimwipe to thoroughly clean the top of the walls of the cup and the bottom of the outside of the dial. Isopropyl alcohol may be needed to get it properly clean, but if used, the glovebox must be allowed to air out as the isopropyl alcohol fumes will affect most samples.

   Once you are at the point where the yellow light is about to turn on or off, turn the dial clockwise to the closest notch and then turn it one more notch. The gap is now set and the switch for the light can be turned off.

4. Leave the cup attached until right before you're ready to add the fluid to be measured, in order to keep it as clean as possible. Be careful when detaching and re-attaching the cup that the dial used to set the gap size is not moved!

12. Check oxygen concentration

At this point, check the OxyCheq to make sure it is <2% before continuing. If the oxygen concentration is not low enough yet, increase flow from the gas cylinder (but never exceed 20 psi) and wait before continuing.

13. Extracting the hemolymph sample

Make sure larvae are anesthetized via exposure to <2% oxygen for at least five minutes before moving on with the below extraction steps. Additionally, make sure the water bath temperature has been set to the desired temperature for at least five minutes to ensure consistent temperature samples.

1. Prep your work area: Before working with the larvae, make sure you have a piece of parafilm, your pipette is set to 0.7 mL and has a pipette tip attached, and that the cup has been detached from the viscometer.

2. Hemolymph extraction to parafilm:
   i. Remove the larvae from the centrifuge tube and hold it bent over your index finger, holding its posterior and anterior ends with your middle finger and thumb so that its ventral side is exposed with the prolegs showing (pictured).

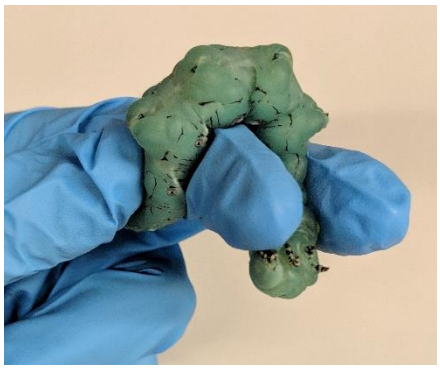

   ii. Use the razor to create a very shallow incision on the larvae between the 2nd and 3rd set of prolegs on the ventral side while holding the larvae over the piece of parafilm. Be *very* careful not to hit the gut or fatty contents on the animal (which are brown or white) as this will contaminate the sample!
   iii. Allow the hemolymph to drip onto the parafilm. In order to obtain enough hemolymph, massage or lightly squeeze the larvae with your other hand very lightly. Sometimes the hemolymph will squirt out at the beginning, be careful to aim at the parafilm.
   iv. Place the larvae back in its centrifuge tube.

3. Move hemolymph to cup and reattach: Use the pipetter (set to 0.70 mL) to suck up the hemolymph deposit, being careful and slow so as to avoid sucking in any air which creates bubbles. Release the hemolymph into the center of the cup, which should be held level. If any bubbles form, carefully use the pipette to remove them. Attach the cup back to the viscometer, being very careful to keep it level!

14. Begin data collection

On the computer, hit "Connect" on the CoolTerm window, which should begin showing lines of data within the window. On the viscometer, press "Motor on/off" to begin spindle rotation and viscosity measurements. Note: It may take a few seconds for data to show on the CoolTerm window but if it does not show after ~10 seconds, check the connection between the viscometer and the computer.

Tip: While the data is being collected, consider recording observations and any other pertinent information as well as cleaning up the glovebox, including removing the used larvae, parafilm, and pipette tip.

15. End data collection

After enough data has been collected (usually ~25 min is good, but this must be evaluated with each trial), press “Motor on/off” on the viscometer then “Disconnect” on the computer. Before exiting the CoolTerm file or opening a new one, make sure the current data is saved in the folder you originally chose and the data has been written to it. You can also analyze the data by copying the current CoolTerm file and uploading the copied file into Excel. This allows you to graph the data and see if the viscosity measurement levels out.

16. Clean up and reset

Remove both the cup and spindle and clean each one using distilled water and Kimwipes. Turn off the viscometer (it will need to re-zero the spindle when you reattach it). To start another trial, begin again at step #6, otherwise make sure to clean out the glovebox and turn off the water bath, the flow from the gas cylinder, the humidifier, the OxyCheq, and the viscometer for the day.

Appendix C

Chapter 4 supporting information

C.1 Code repository

https://github.com/TheSochaLab/Effects-of-environmental-temperature-on-viscosity-of-Manduca-sexta-hemolymph

C.2 Supplemental materials

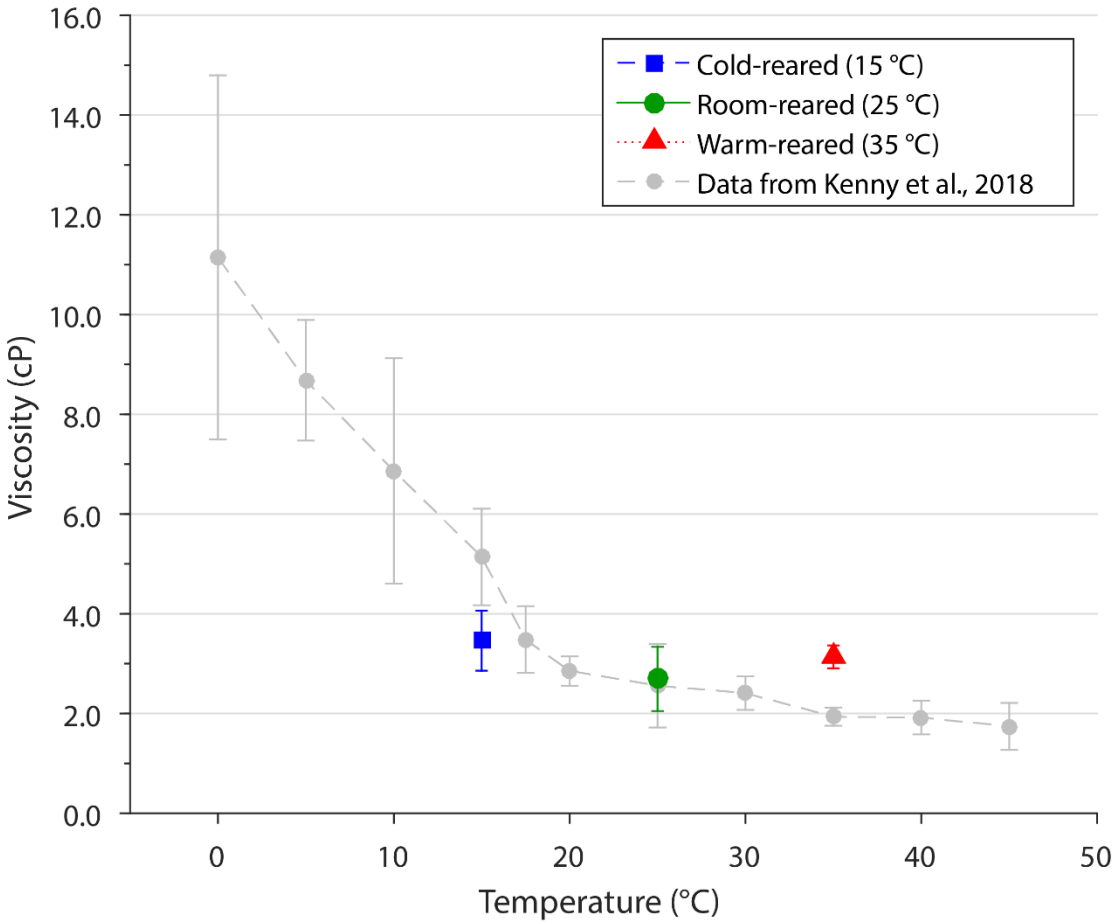

Figure C.2.1: Hemolymph viscosity from cold-, room-, and warm-reared *Manduca sexta* larvae measured at the corresponding rearing temperature. Previous hemolymph viscosity values from Kenny et al. [4] are shown for comparison. Filled points represent the average value for each temperature and rearing condition, with error bars representing 95% confidence intervals for the mean.


Trial 670 at 5°C, reared at 15°C
Trial 671 at 5°C, reared at 15°C
Trial 672 at 5°C, reared at 15°C
Trial 673 at 5°C, reared at 15°C
Trial 700 at 5°C, reared at 15°C
Trial 701 at 5°C, reared at 15°C
Trial 702 at 5°C, reared at 15°C
Trial 703 at 5°C, reared at 15°C
Trial 724 at 5°C, reared at 15°C
Trial 725 at 5°C, reared at 15°C
Trial 630 at 15°C, reared at 15°C
Trial 631 at 15°C, reared at 15°C
Trial 662 at 15°C, reared at 15°C
Trial 663 at 15°C, reared at 15°C
Trial 664 at 15°C, reared at 15°C
Trial 671 at 15°C, reared at 15°C
Trial 673 at 15°C, reared at 15°C
Trial 674 at 15°C, reared at 15°C
Trial 675 at 15°C, reared at 15°C
Trial 688 at 15°C, reared at 15°C
Trial 625 at 25°C, reared at 15°C
Trial 626 at 25°C, reared at 15°C
Trial 652 at 25°C, reared at 15°C
Trial 653 at 25°C, reared at 15°C
Trial 654 at 25°C, reared at 15°C
Trial 677 at 25°C, reared at 15°C
Trial 678 at 25°C, reared at 15°C
Trial 679 at 25°C, reared at 15°C
Trial 689 at 25°C, reared at 15°C
Trial 690 at 25°C, reared at 15°C
Data not included
Acceptable data
Viscosity st. dev.
Viscosity (cP)
Standard Deviation (mPas)
Time (min)

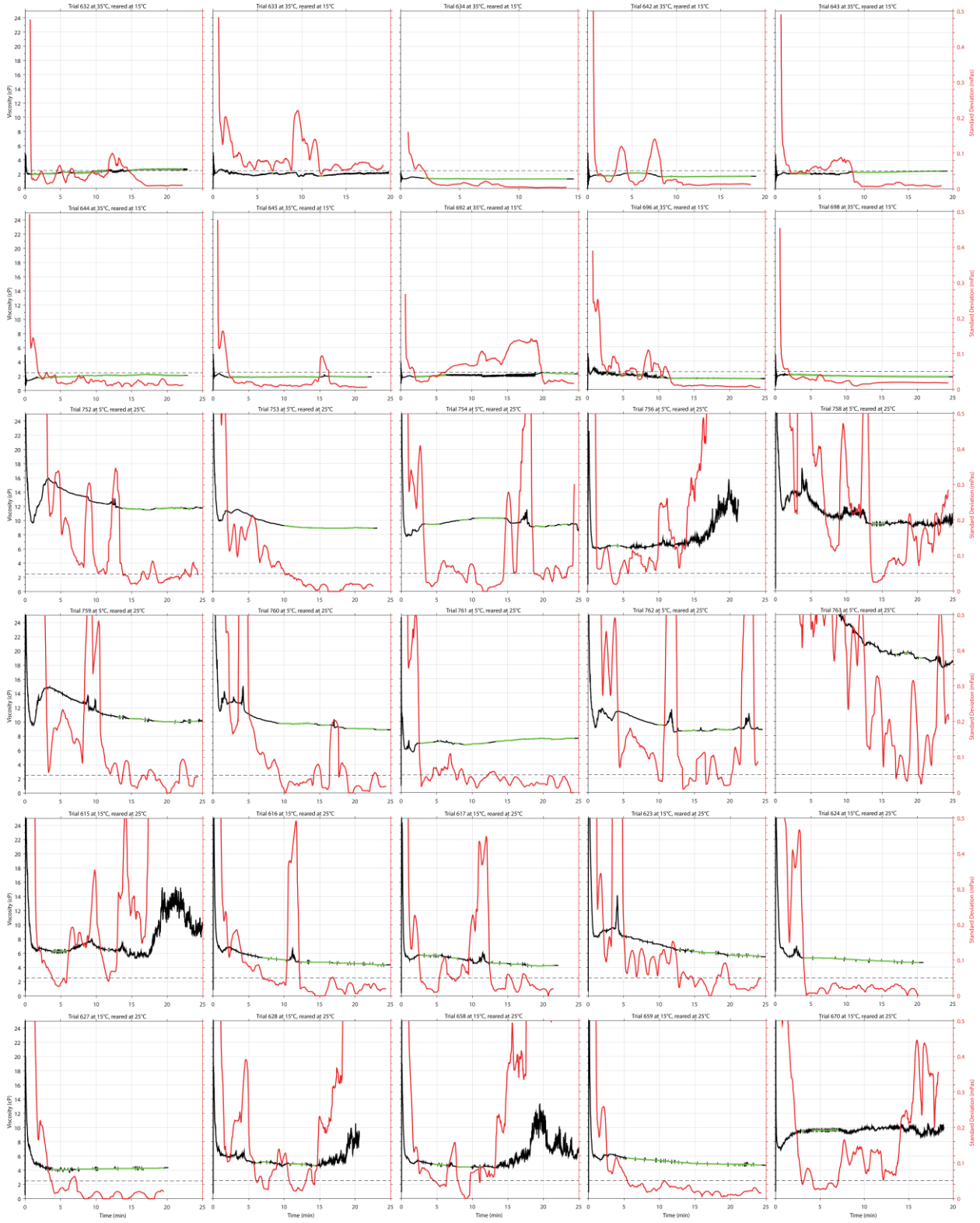
Trial 632 at 35°C, reared at 15°C
Trial 633 at 35°C, reared at 15°C
Trial 634 at 35°C, reared at 15°C
Trial 642 at 35°C, reared at 15°C
Trial 643 at 35°C, reared at 15°C
Trial 644 at 35°C, reared at 15°C
Trial 645 at 35°C, reared at 15°C
Trial 692 at 35°C, reared at 15°C
Trial 696 at 35°C, reared at 15°C
Trial 698 at 35°C, reared at 15°C
Trial 752 at 5°C, reared at 25°C
Trial 753 at 5°C, reared at 25°C
Trial 754 at 5°C, reared at 25°C
Trial 756 at 5°C, reared at 25°C
Trial 758 at 5°C, reared at 25°C
Trial 759 at 5°C, reared at 25°C
Trial 760 at 5°C, reared at 25°C
Trial 761 at 5°C, reared at 25°C
Trial 762 at 5°C, reared at 25°C
Trial 765 at 5°C, reared at 25°C
Trial 615 at 15°C, reared at 25°C
Trial 616 at 15°C, reared at 25°C
Trial 617 at 15°C, reared at 25°C
Trial 623 at 15°C, reared at 25°C
Trial 624 at 15°C, reared at 25°C
Trial 627 at 15°C, reared at 25°C
Trial 628 at 15°C, reared at 25°C
Trial 658 at 15°C, reared at 25°C
Trial 659 at 15°C, reared at 25°C
Trial 670 at 15°C, reared at 25°C
Viscosity (cP)
Standard Deviation (mPas)
Time (min)

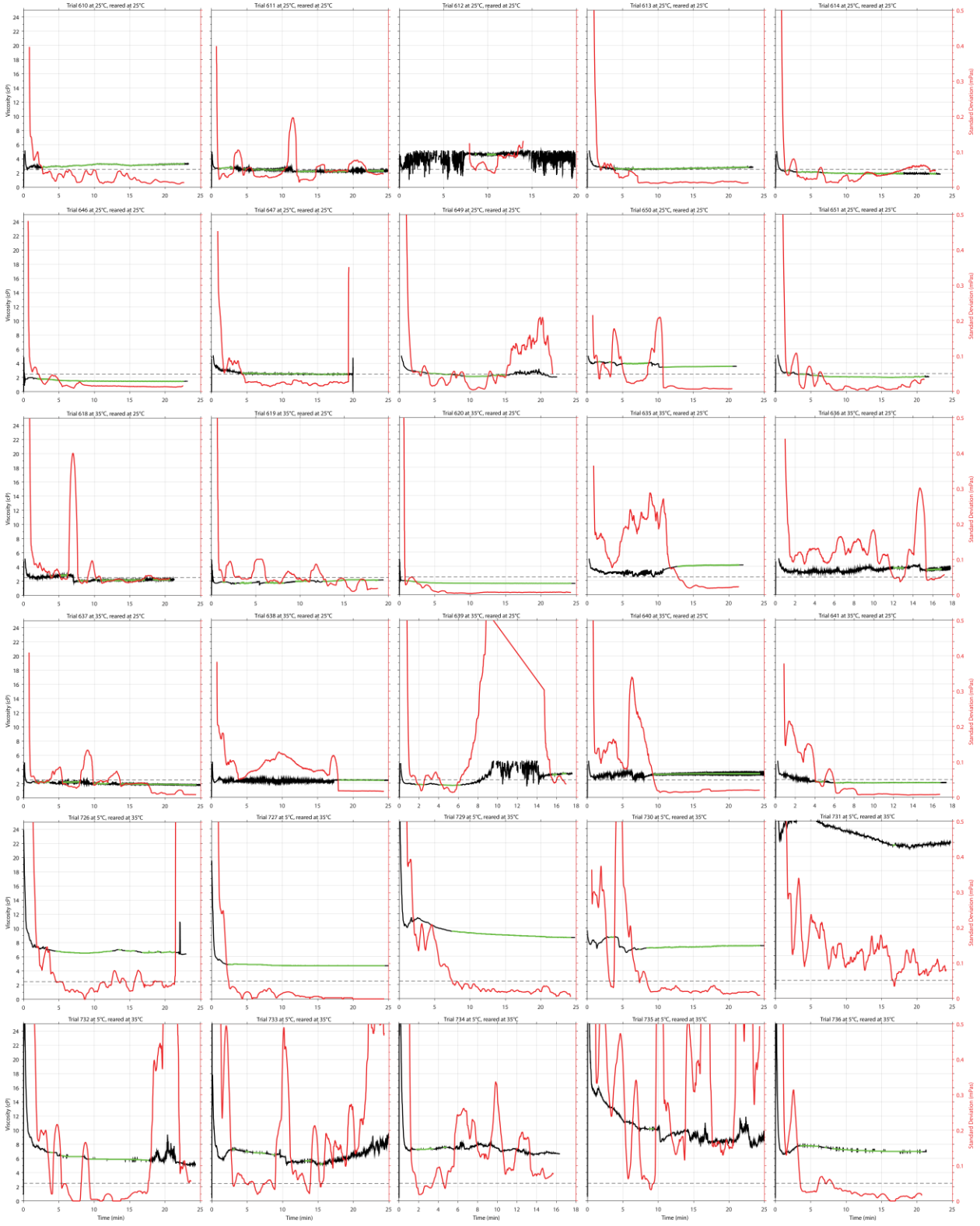
Trial 610 at 25°C, reared at 25°C
Trial 611 at 25°C, reared at 25°C
Trial 612 at 25°C, reared at 25°C
Trial 613 at 25°C, reared at 25°C
Trial 614 at 25°C, reared at 25°C
Trial 646 at 25°C, reared at 25°C
Trial 647 at 25°C, reared at 25°C
Trial 649 at 25°C, reared at 25°C
Trial 650 at 25°C, reared at 25°C
Trial 651 at 25°C, reared at 25°C
Trial 618 at 35°C, reared at 25°C
Trial 619 at 35°C, reared at 25°C
Trial 620 at 35°C, reared at 25°C
Trial 635 at 35°C, reared at 25°C
Trial 636 at 35°C, reared at 25°C
Trial 637 at 35°C, reared at 25°C
Trial 638 at 35°C, reared at 25°C
Trial 639 at 35°C, reared at 25°C
Trial 640 at 35°C, reared at 25°C
Trial 641 at 35°C, reared at 25°C
Trial 726 at 5°C, reared at 35°C
Trial 727 at 5°C, reared at 35°C
Trial 729 at 5°C, reared at 35°C
Trial 730 at 5°C, reared at 35°C
Trial 731 at 5°C, reared at 35°C
Trial 732 at 5°C, reared at 35°C
Trial 733 at 5°C, reared at 35°C
Trial 734 at 5°C, reared at 35°C
Trial 735 at 5°C, reared at 35°C
Trial 736 at 5°C, reared at 35°C
Viscosity (cP)
Standard Deviation (mPas)
Time (min)


Trial 681 at 15°C, reared at 35°C
Trial 682 at 15°C, reared at 35°C
Trial 683 at 15°C, reared at 35°C
Trial 684 at 15°C, reared at 35°C
Trial 685 at 15°C, reared at 35°C
Trial 737 at 15°C, reared at 35°C
Trial 738 at 15°C, reared at 35°C
Trial 741 at 15°C, reared at 35°C
Trial 742 at 15°C, reared at 35°C
Trial 743 at 15°C, reared at 35°C
Trial 687 at 25°C, reared at 35°C
Trial 706 at 25°C, reared at 35°C
Trial 707 at 25°C, reared at 35°C
Trial 708 at 25°C, reared at 35°C
Trial 714 at 25°C, reared at 35°C
Trial 715 at 25°C, reared at 35°C
Trial 716 at 25°C, reared at 35°C
Trial 717 at 25°C, reared at 35°C
Trial 749 at 25°C, reared at 35°C
Trial 751 at 25°C, reared at 35°C
Trial 694 at 35°C, reared at 35°C
Trial 677 at 35°C, reared at 35°C
Trial 709 at 35°C, reared at 35°C
Trial 710 at 35°C, reared at 35°C
Trial 712 at 35°C, reared at 35°C
Trial 713 at 35°C, reared at 35°C
Trial 718 at 35°C, reared at 35°C
Trial 719 at 35°C, reared at 35°C
Trial 720 at 35°C, reared at 35°C
Trial 722 at 35°C, reared at 35°C
Viscosity (cP)
Standard Deviation (mPas)
Time (min)

Figure C.2.2 (previous pages): Traces of viscosity over time for each hemolymph trial for cold-, room-, and warm-reared *Manduca sexta* larvae (n=120). The title of each graph indicates the trial number, the temperature of the water bath, and the rearing temperature. The raw viscosity data are indicated in black and green, with green indicating that the standard deviation (plotted in red) was below 0.05. Only green data were included in the calculated average for the trial. This calculation and plotting method was originally developed by Kenny et al. [4].

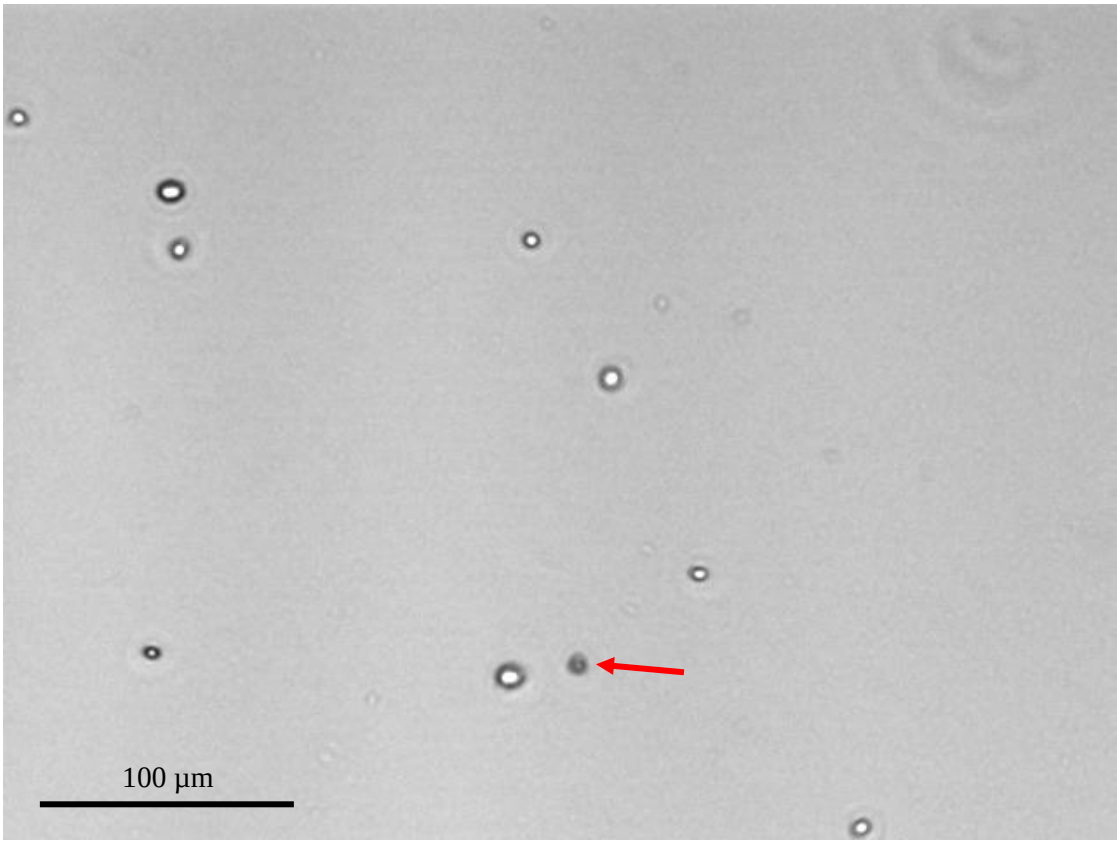

Figure C.2.3: Representative photo of hemocytes in the hemolymph of *Manduca sexta* larvae. A 1 mL sample of 9:1 dilution of hemolymph with an anticoagulant (98 mM NaOH, 186 mM NaCl, 1.7 mM EDTA, 41 mM citric acid, pH 6.8 [5]) within a capillary tube is photographed using a cell counter (Vi-Cell), and photos are analyzed for number of viable cells, number of nonviable cells, cell circularity, and cell diameter. This representative photo shows 9 viable cells and 1 nonviable (red arrow), indicated by the uptake of trypan blue due to cell membrane damage.

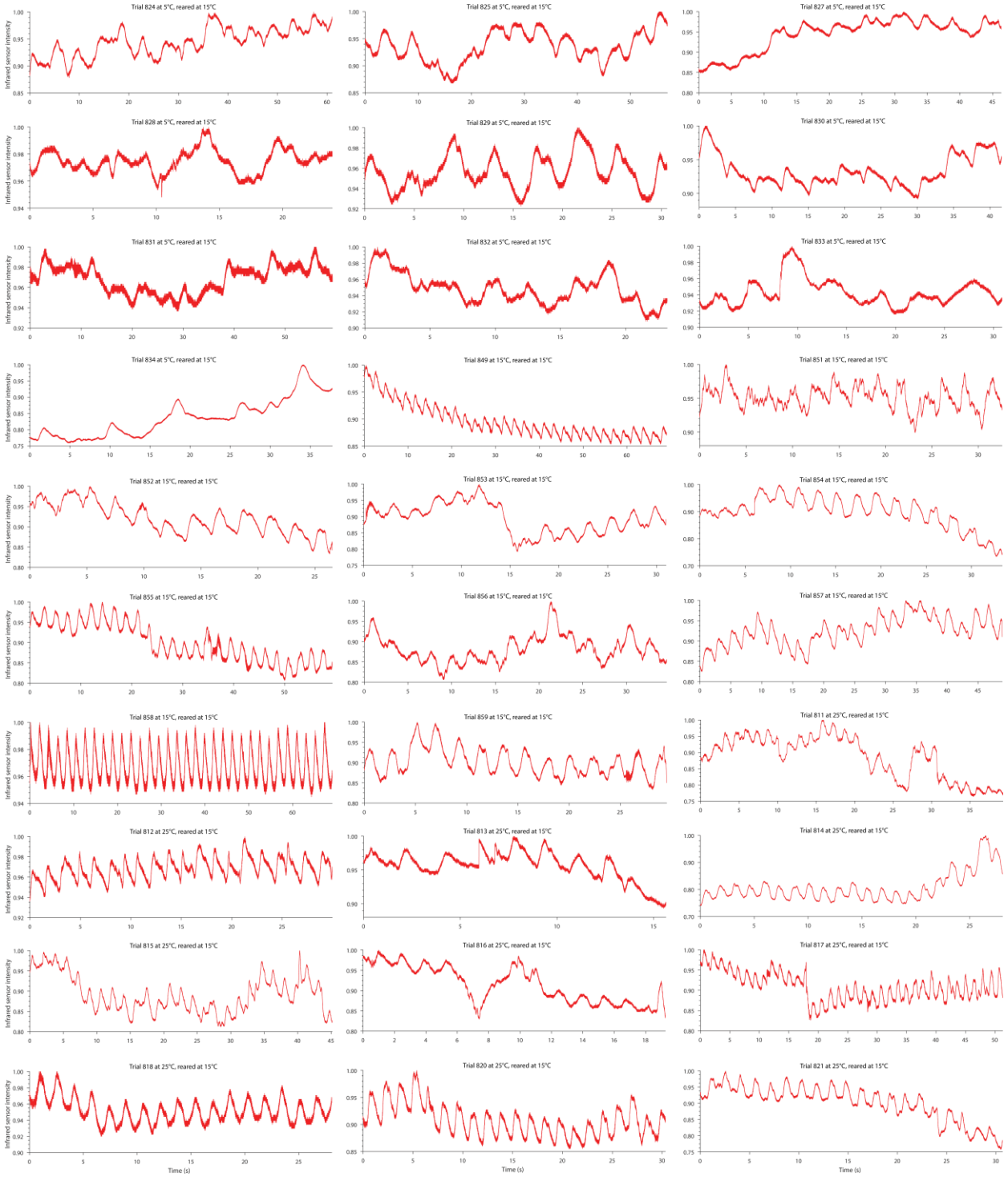
Trial 824 at 5°C, reared at 15°C
Trial 825 at 5°C, reared at 15°C
Trial 827 at 5°C, reared at 15°C
Trial 828 at 5°C, reared at 15°C
Trial 829 at 5°C, reared at 15°C
Trial 830 at 5°C, reared at 15°C
Trial 831 at 5°C, reared at 15°C
Trial 832 at 5°C, reared at 15°C
Trial 833 at 5°C, reared at 15°C
Trial 834 at 5°C, reared at 15°C
Trial 849 at 15°C, reared at 15°C
Trial 851 at 15°C, reared at 15°C
Trial 852 at 15°C, reared at 15°C
Trial 853 at 15°C, reared at 15°C
Trial 854 at 15°C, reared at 15°C
Trial 855 at 15°C, reared at 15°C
Trial 856 at 15°C, reared at 15°C
Trial 857 at 15°C, reared at 15°C
Trial 858 at 15°C, reared at 15°C
Trial 859 at 15°C, reared at 15°C
Trial 811 at 25°C, reared at 15°C
Trial 812 at 25°C, reared at 15°C
Trial 813 at 25°C, reared at 15°C
Trial 814 at 25°C, reared at 15°C
Trial 815 at 25°C, reared at 15°C
Trial 816 at 25°C, reared at 15°C
Trial 817 at 25°C, reared at 15°C
Trial 818 at 25°C, reared at 15°C
Trial 820 at 25°C, reared at 15°C
Trial 821 at 25°C, reared at 15°C
Infrared sensor intensity
Time (s)

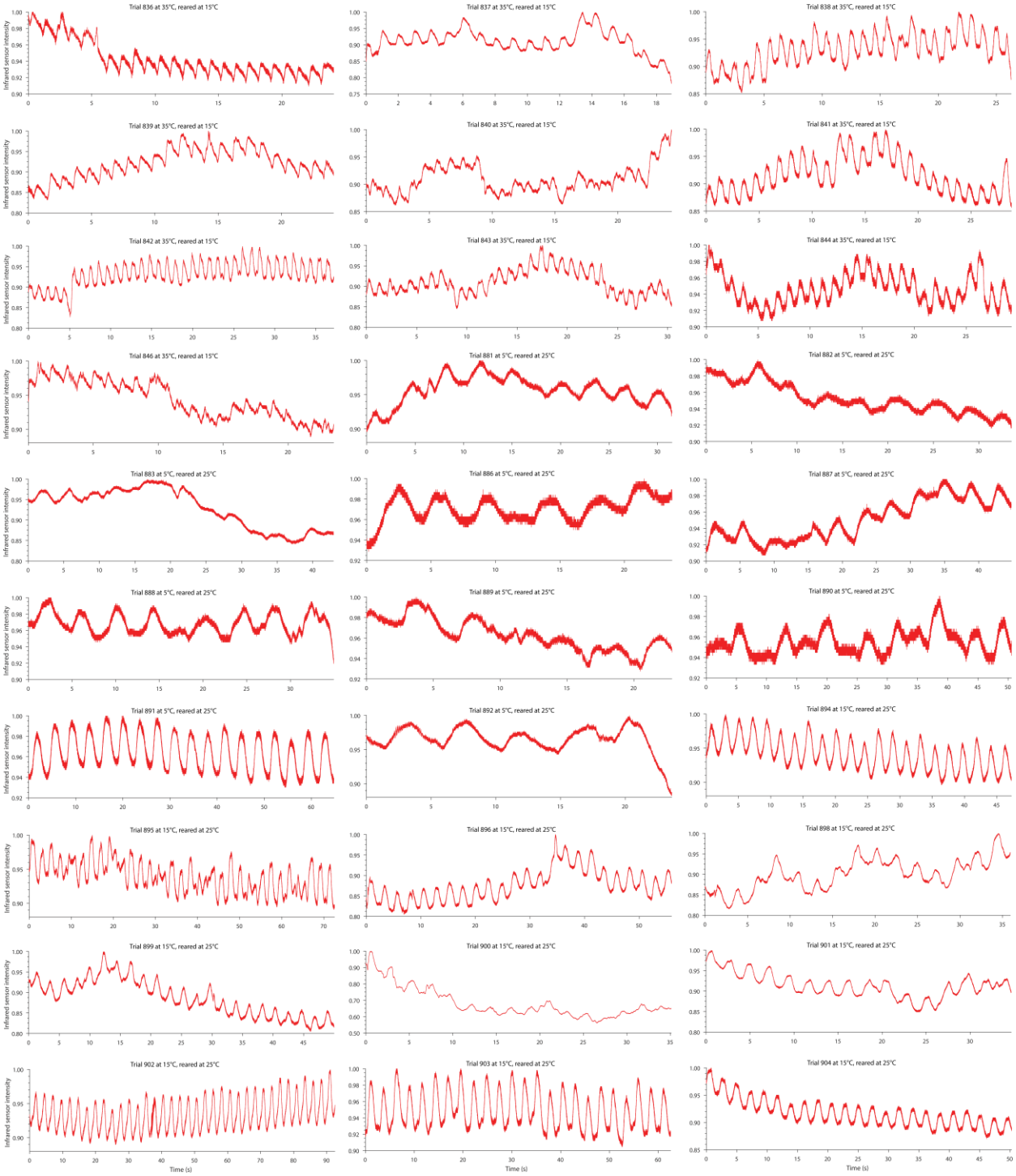
Trial 836 at 35°C, reared at 15°C
Trial 837 at 35°C, reared at 15°C
Trial 838 at 35°C, reared at 15°C
Trial 839 at 35°C, reared at 15°C
Trial 840 at 35°C, reared at 15°C
Trial 841 at 35°C, reared at 15°C
Trial 842 at 35°C, reared at 15°C
Trial 843 at 35°C, reared at 15°C
Trial 844 at 35°C, reared at 15°C
Trial 846 at 35°C, reared at 15°C
Trial 881 at 5°C, reared at 25°C
Trial 882 at 5°C, reared at 25°C
Trial 883 at 5°C, reared at 25°C
Trial 886 at 5°C, reared at 25°C
Trial 887 at 5°C, reared at 25°C
Trial 888 at 5°C, reared at 25°C
Trial 889 at 5°C, reared at 25°C
Trial 890 at 5°C, reared at 25°C
Trial 891 at 5°C, reared at 25°C
Trial 892 at 5°C, reared at 25°C
Trial 894 at 15°C, reared at 25°C
Trial 895 at 15°C, reared at 25°C
Trial 896 at 15°C, reared at 25°C
Trial 898 at 15°C, reared at 25°C
Trial 899 at 15°C, reared at 25°C
Trial 900 at 15°C, reared at 25°C
Trial 901 at 15°C, reared at 25°C
Trial 902 at 15°C, reared at 25°C
Trial 903 at 15°C, reared at 25°C
Trial 904 at 15°C, reared at 25°C
Infrared sensor intensity
Time (s)

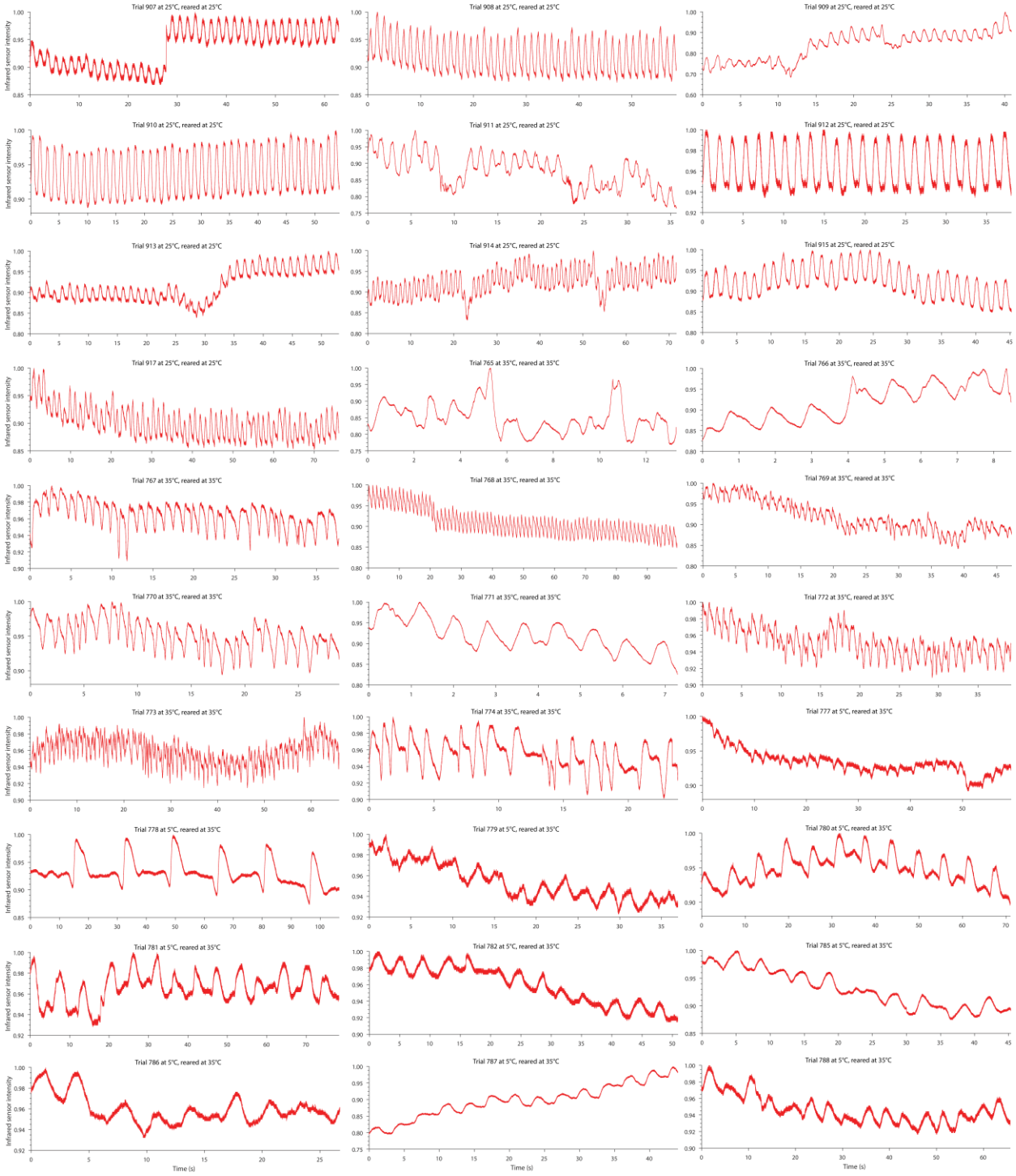
Trial 907 at 25°C, reared at 25°C
Trial 908 at 25°C, reared at 25°C
Trial 909 at 25°C, reared at 25°C
Trial 910 at 25°C, reared at 25°C
Trial 911 at 25°C, reared at 25°C
Trial 912 at 25°C, reared at 25°C
Trial 913 at 25°C, reared at 25°C
Trial 914 at 25°C, reared at 25°C
Trial 915 at 25°C, reared at 25°C
Trial 917 at 25°C, reared at 25°C
Trial 765 at 35°C, reared at 35°C
Trial 766 at 35°C, reared at 35°C
Trial 767 at 35°C, reared at 35°C
Trial 768 at 35°C, reared at 35°C
Trial 769 at 35°C, reared at 35°C
Trial 770 at 35°C, reared at 35°C
Trial 771 at 35°C, reared at 35°C
Trial 772 at 35°C, reared at 35°C
Trial 773 at 35°C, reared at 35°C
Trial 774 at 35°C, reared at 35°C
Trial 777 at 5°C, reared at 35°C
Trial 778 at 5°C, reared at 35°C
Trial 779 at 5°C, reared at 35°C
Trial 780 at 5°C, reared at 35°C
Trial 781 at 5°C, reared at 35°C
Trial 782 at 5°C, reared at 35°C
Trial 785 at 5°C, reared at 35°C
Trial 786 at 5°C, reared at 35°C
Trial 787 at 5°C, reared at 35°C
Trial 788 at 5°C, reared at 35°C
Infrared sensor intensity
Time (s)

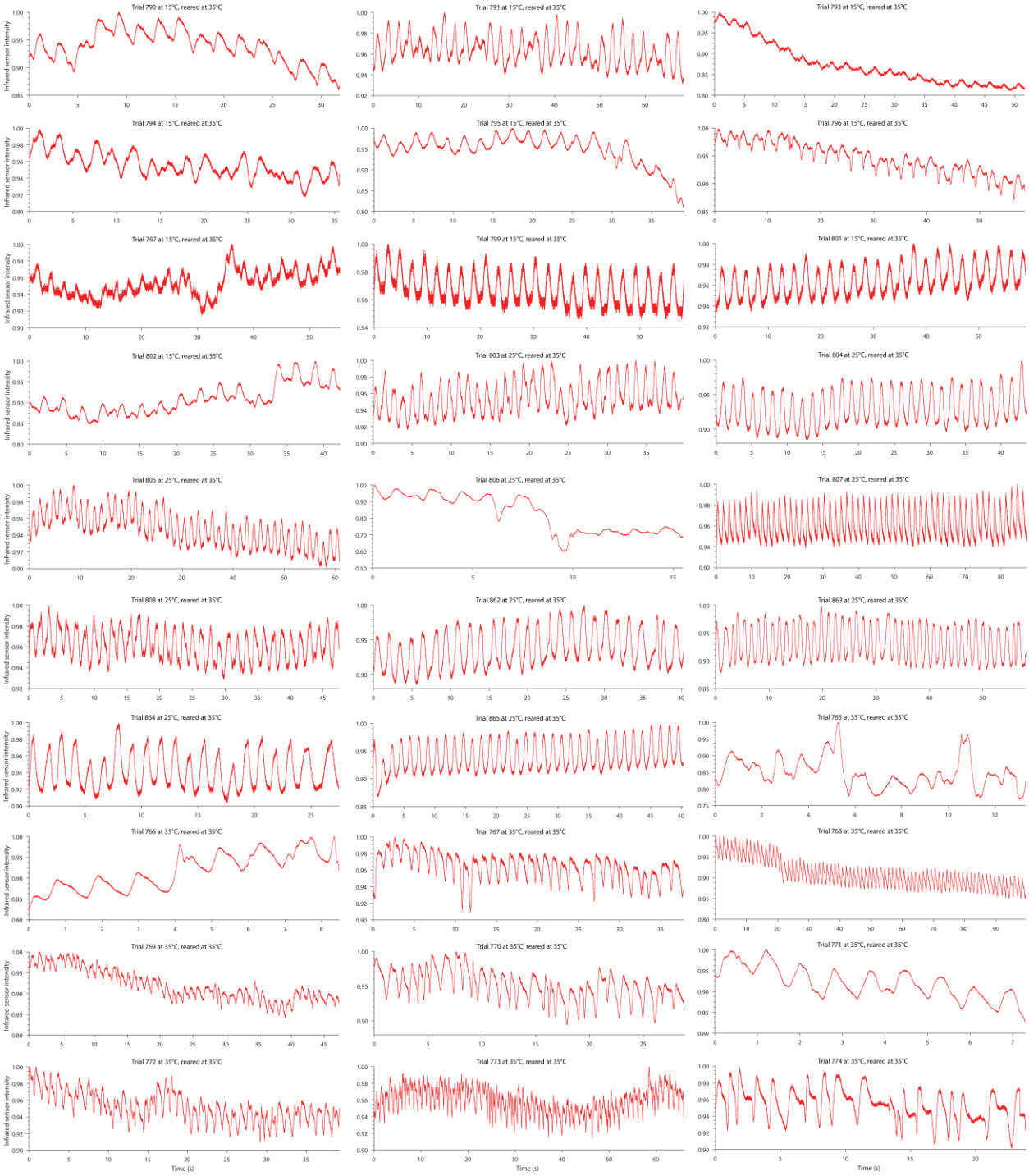

Figure C.2.4 (previous pages): Recordings of heartbeat in *Manduca sexta* larvae. Traces of infrared sensor intensity when aimed at the mid-dorsal surface of *Maduca sexta* larvae over time. Infrared readings show movements in the soft tissue and muscle surrounding the heart of each insect, where pulsations represent heart beats. The title of each graph indicates the trial number, exposure temperature, and rearing temperature.

Appendix D

Chapter 5 supporting information

D.1 Supplemental materials

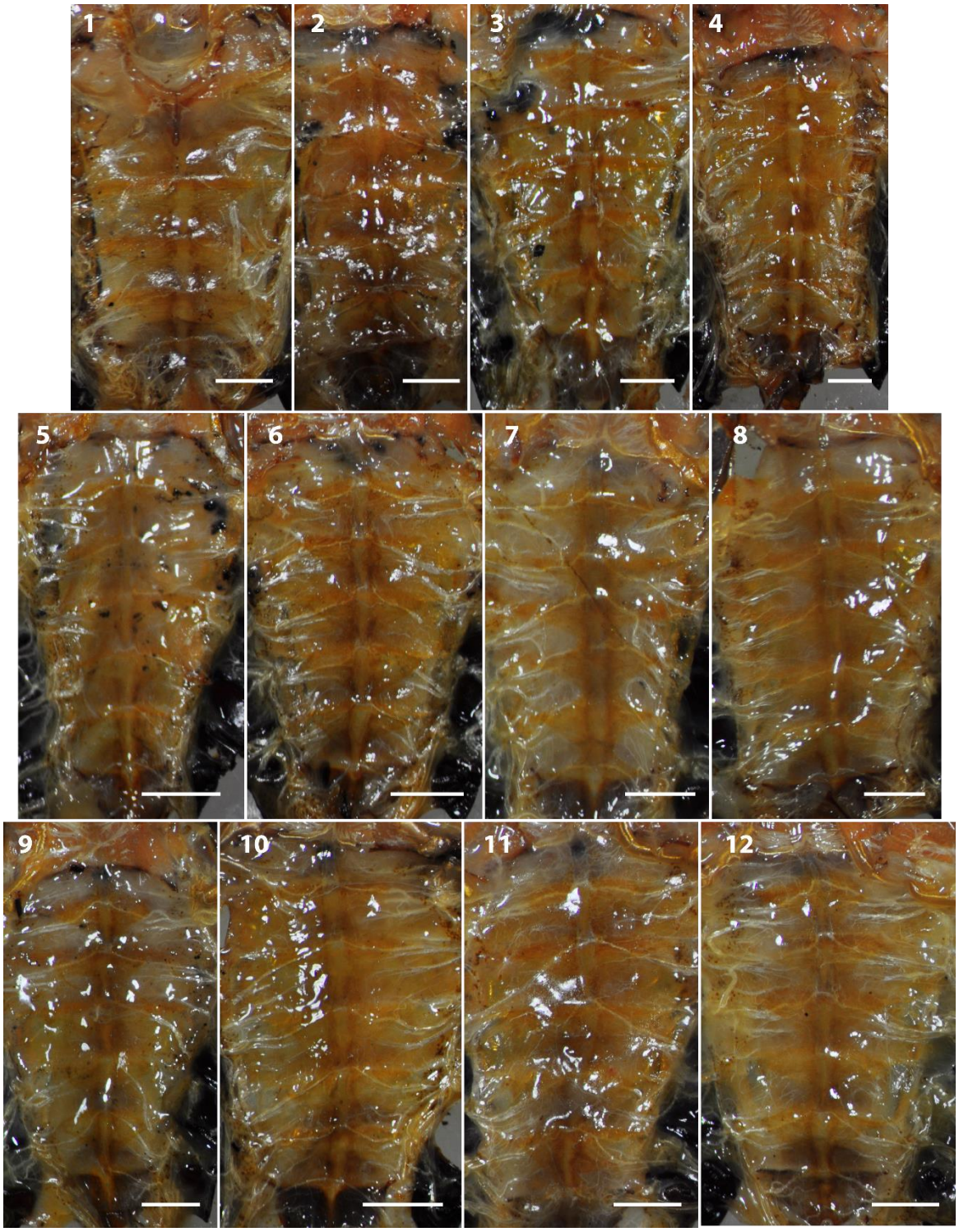

Figure D.1.1: Photos of the dissected dorsal vessel of 12 *Zophobas morio* beetles, showing the inner portion of the dorsal surface where anterior is the top of each photo and posterior is the bottom. The dorsal vessel and diamond-shaped alary muscle pairs can be viewed. Scale bars indicate 2 mm.

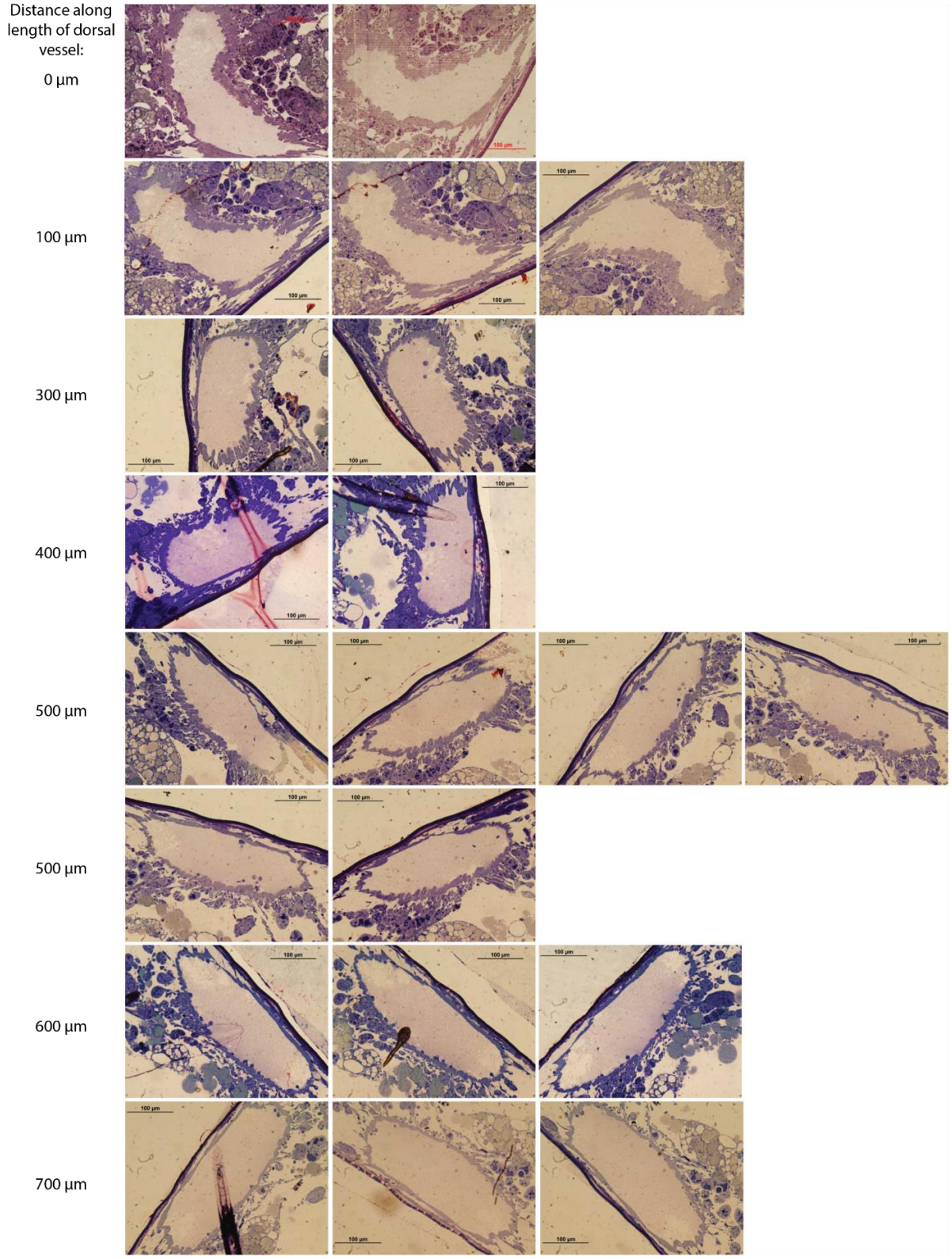
Distance along length of dorsal vessel:
0 µm
100 µm
300 µm
400 µm
500 µm
500 µm
600 µm
700 µm

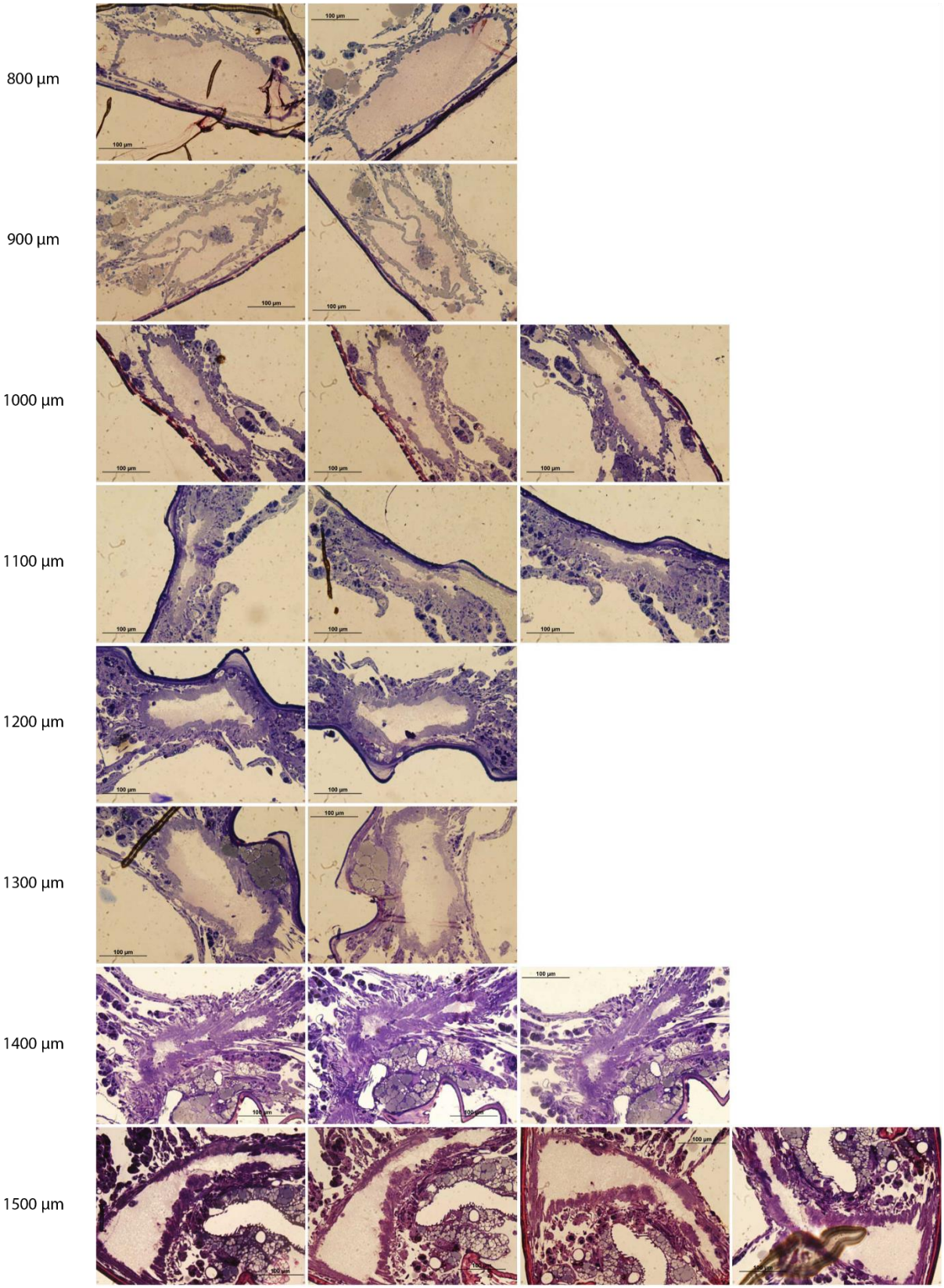
800 µm
900 µm
1000 µm
1100 µm
1200 µm
1300 µm
1400 µm
1500 µm

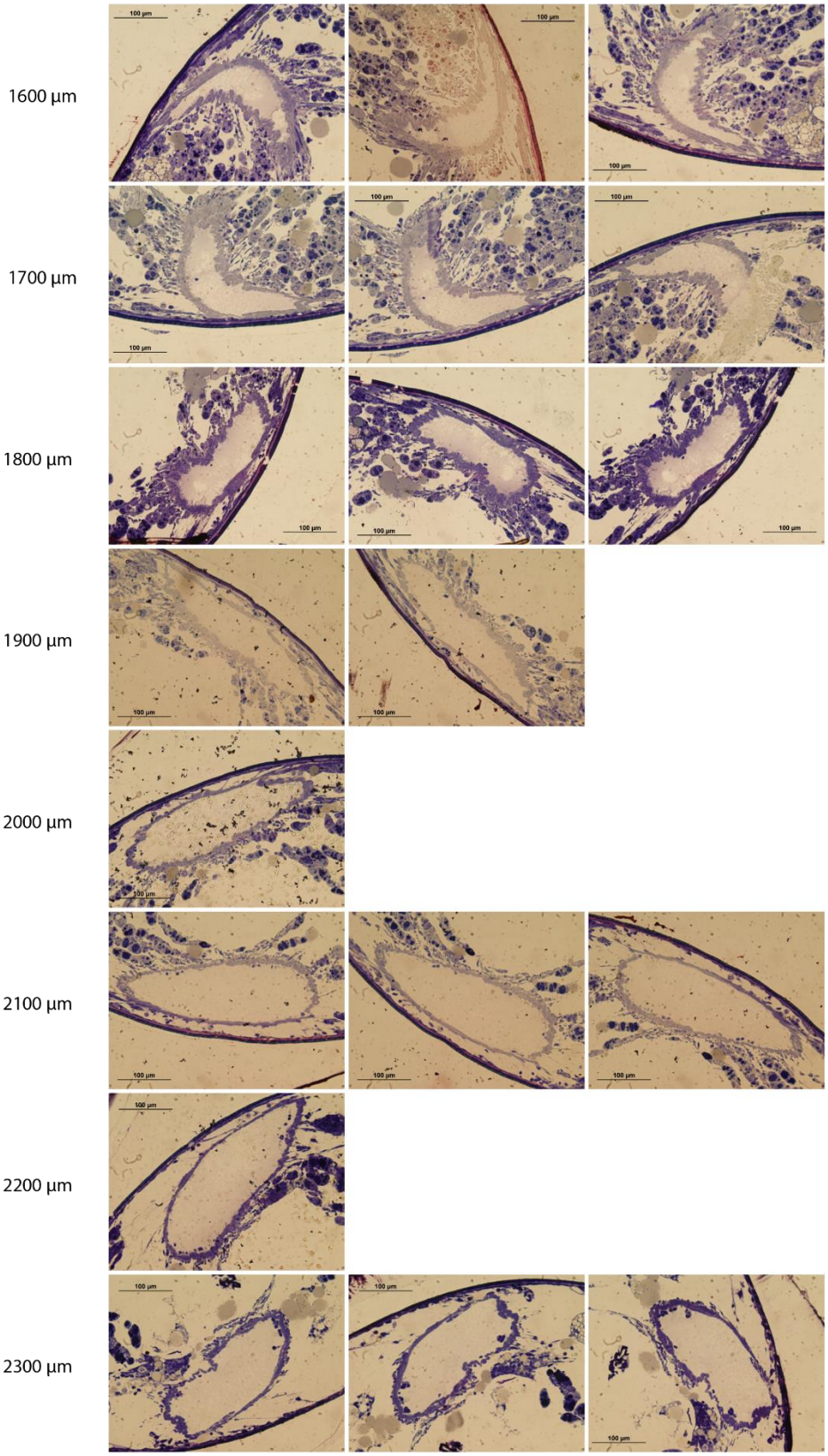
1600 µm
1700 µm
1800 µm
1900 µm
2000 µm
2100 µm
2200 µm
2300 µm

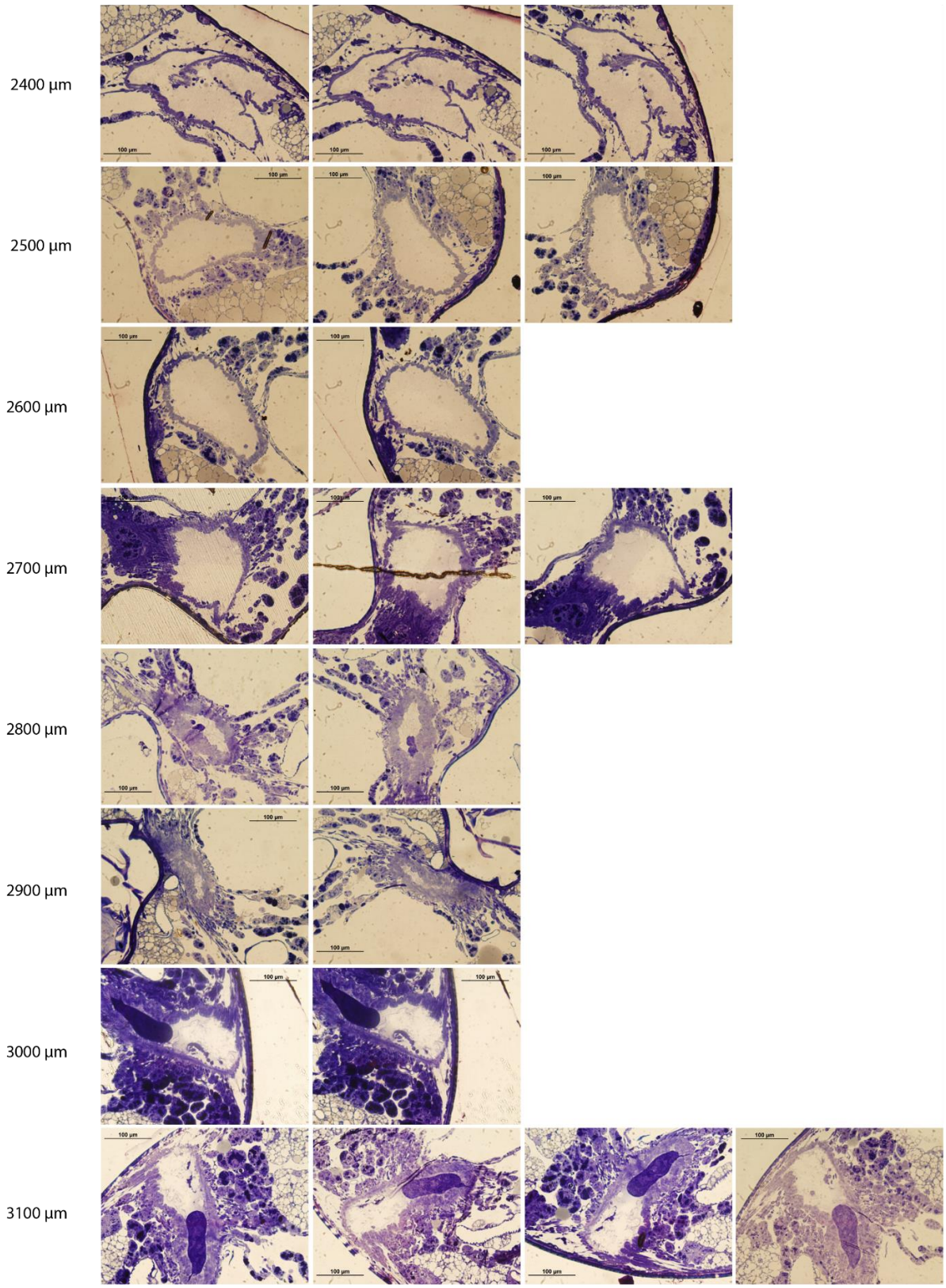
2400 µm
2500 µm
2600 µm
2700 µm
2800 µm
2900 µm
3000 µm
3100 µm

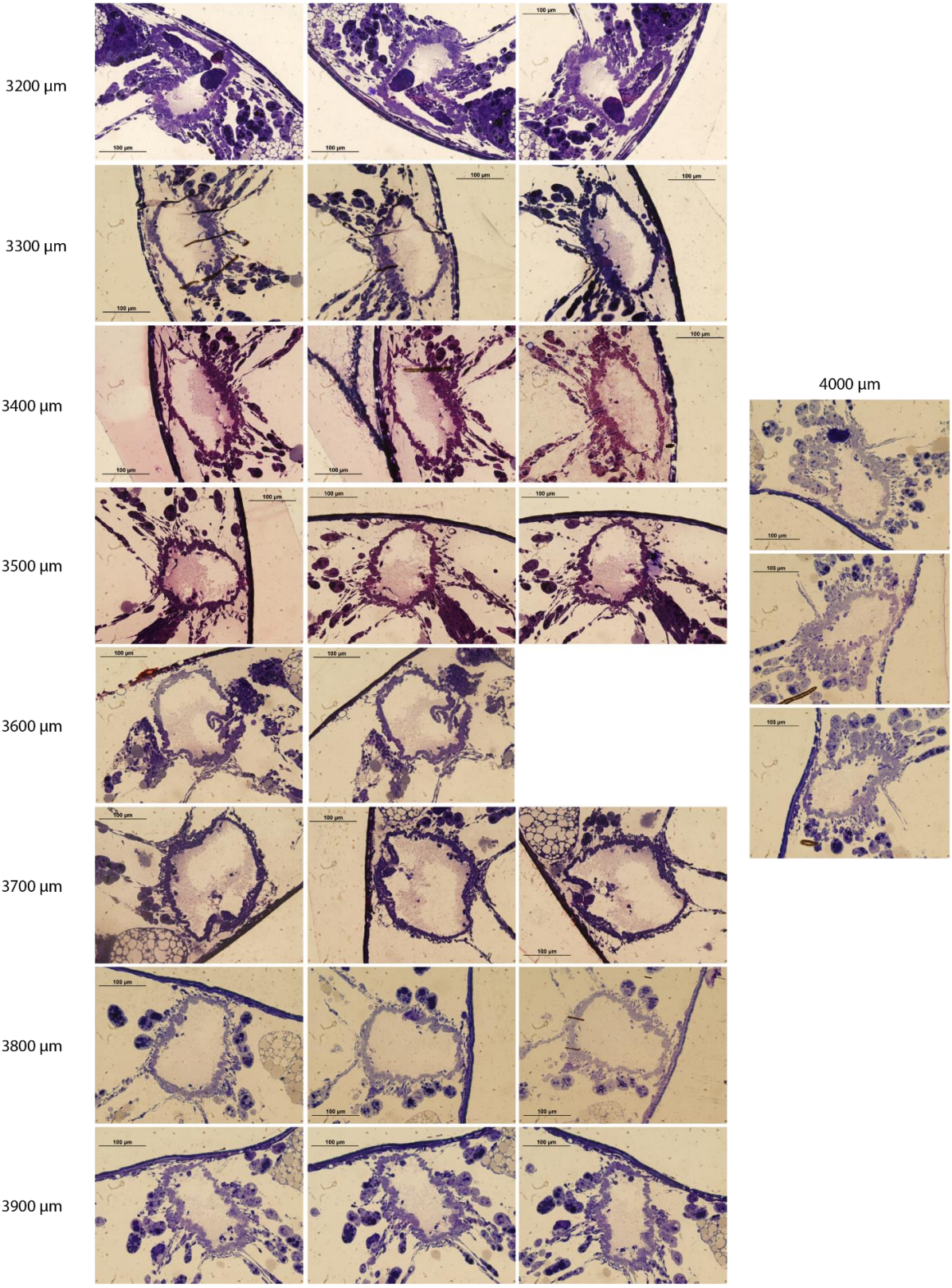
3200 µm
3300 µm
3400 µm
3500 µm
3600 µm
3700 µm
3800 µm
3900 µm
4000 µm

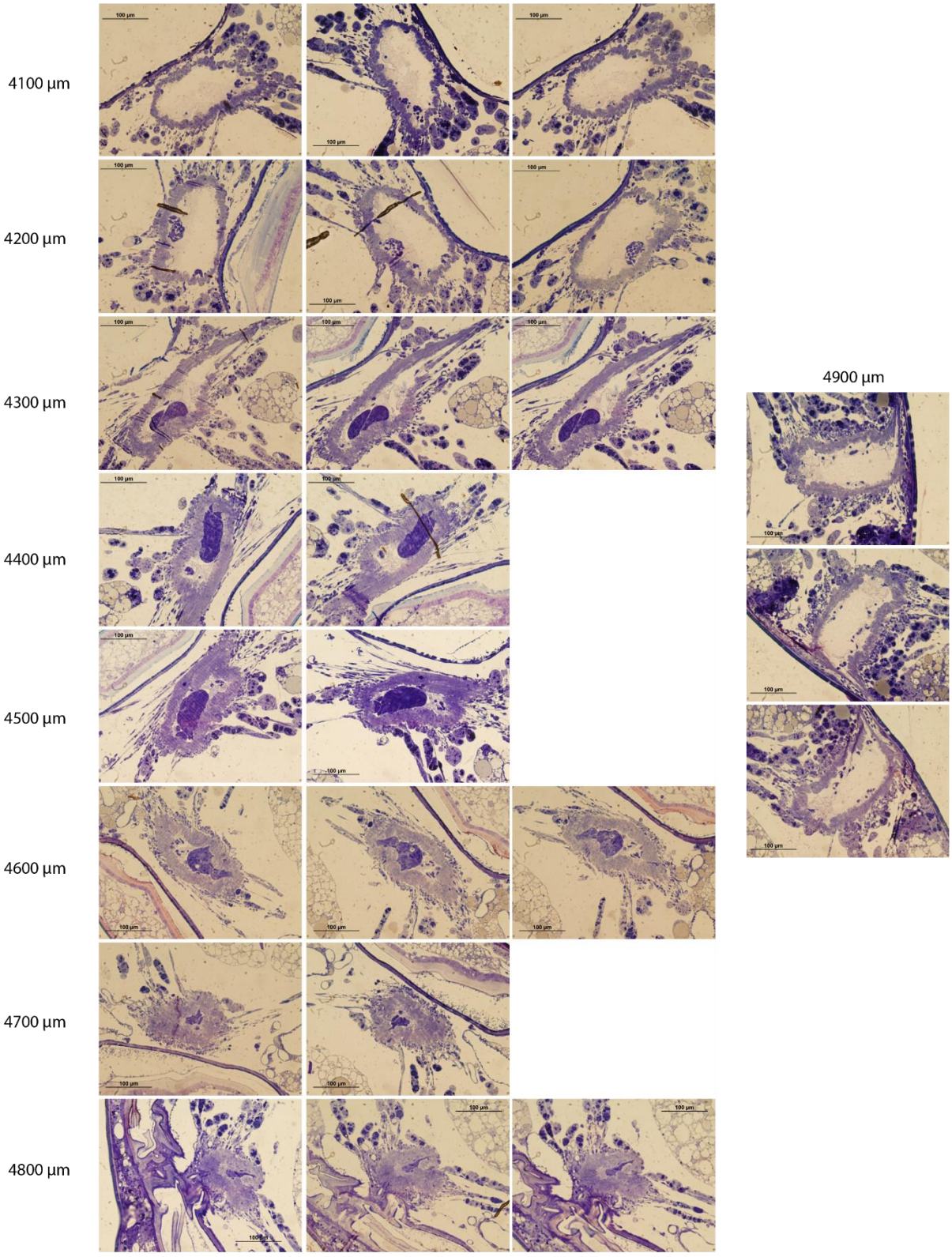
4100 µm
4200 µm
4300 µm
4400 µm
4500 µm
4600 µm
4700 µm
4800 µm
4900 µm

Figure D.1.2 (previous pages): Microtome sections of the dorsal vessel of a single *Zophobas morio* beetle (m = 0.4914 g). Distance along the dorsal vessel for each set of sections is indicated either to the left or above groups of images.

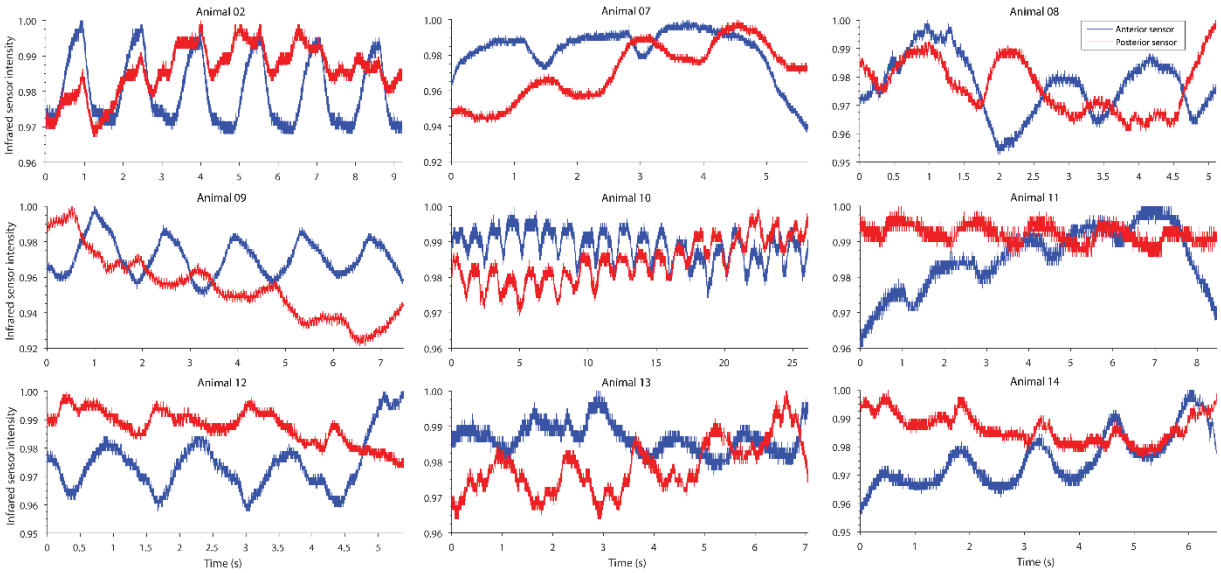

Figure D.1.3: IR traces showing IR intensity for the anterior and posterior sensor over time for nine *Zophobas morio* adults.